Radiative-Convective Equilibrium

Atmospheric Simulations in DALES

L. J. W. Wester

Delft University of Technology

TU Delft Delft University of Technology

Challenge the future

RADIATIVE-CONVECTIVE EQUILIBRIUM

ATMOSPHERIC SIMULATIONS IN DALES

by

Laurens Jan Willem Wester

in partial fulfilment of the requirements for the degree of

Master of Science

in Applied Physics

at the Delft University of Technology,

to be defended publicly on November 26, 2015 at 15:00

Student number:	1543652	
Project duration:	October, 2014 – November, 2015	
Supervisor:	Dr. S. R. de Roode	
Thesis committee:	Prof. dr. A P. Siebesma,	TU Delft/KNMI
	Prof. dr. D. J. E. M. Roekaerts	TU Delft

An electronic version of this thesis is available at http://repository.tudelft.nl/.

TU Delft Delft University of Technology

Abstract

Climate research aims at investigating the atmosphere. Most of this research is performed using low resolution models. Using higher resolution models reduces the need for parametrizations and reduces the uncertainties associated with the low resolution models.

The primary purpose of this study is to investigate the equilibrium using a higher resolution Large Eddy Simulation (LES) model, DALES. In the theoretical situation of radiative-convective equilibrium (RCE) the heat transport of radiation and convection are in equilibrium. Investigating RCE requires domains with altitudes of up to 30 km, this has not been simulated before in the model. The implementation of radiative transfer has been tested by analyzing radiative equilibrium as first researched by Manabe and Strickler (1964). In the experiments of this thesis atmospheres in radiative and in radiative-convective equilibrium are investigated.

These experiments were performed using DALES using the recently implemented RRTMG radiative transfer module. For these simulations ice clouds have been implemented in DALES. To investigate radiative equilibrium a modified version of DALES was used. These simulations were performed on a 30 km high grid with 158 vertical levels. The horizontal size for the radiative equilibrium simulations consisted of a 2×2 domain of $2.5km \times 2.5km$ effectively resulting in a single-column model because of the periodic boundary conditions. Simulations in radiative-convective equilibrium were performed using a horizontal domain of 288×288 grid points on a $72km \times 72km$ domain. Initial RCE simulations on a smaller 24 km domain were used as input to speed up the simulations. The RCE simulations have been performed for surface temperatures of 22°C, 24°C, 26°C and 28°C.

Radiative equilibrium results in a high surface temperature of almost 334K and in very steep lapse rates which indicates that the atmosphere in radiative equilibrium is inherently unstable. Although ozone has large effects on the stratospheric temperature and is responsible for creation of the tropopause inversion, the effect on the surface temperature is negligible. Carbon dioxide and water vapor both act as greenhouse gasses, increasing the surface temperature in radiative equilibrium. Of these two gasses water vapor has the largest effect on the temperature in the atmosphere.

In radiative-convective equilibrium the tropopause height moves upwards due to the convective heat transport. Increasing the surface temperature moves the tropopause further upwards. The lapse rate in the troposphere are relatively close to the saturated adiabatic lapse rate. At the top of the troposphere an almost entirely cloudy layer is formed which moves upwards with increasing surface temperature. Analysis of the CAPE suggests that the lower and middle troposphere are approximately equally stable at these four prescribed surface temperatures, differences in CAPE can be contributed to the top of the troposphere.

A higher relative humidity in the troposphere is reached in the simulations with higher surface temperatures, although the cloud water path remains approximately the same. Although the sensible heat flux from the surface does not change, the latent heat flux increases significantly. Calculation of the cloud radiative effect indicates that the shortwave effect is negative whereas the longwave effect is positive. The net cloud radiative effect however is approximately zero, but as the two effects act at different heights this might still have a destabilizing effect on the atmosphere.

Analysis of the three-dimensional fields showed that vertically developed clouds with small bases developed. Although some areas became dryer than other areas no extensive aggregation was observed. Calculation of the characteristic length scales and analysis of the turbulent spectra indicated that mesoscale fluctuations have formed inside the domain. These mesoscale fluctuations are of a size comparable to the initial domain size of 24 km. Extending the domain to 72 km enabled formation of mesoscale structures.

Previous research showed that DALES is well able to simulate deep convection and the stratocumulus and shallow cumulus regimes. Combined with the findings from this thesis that, with modifications, DALES can be used to perform simulations on domains with altitudes of up to 30 kilometers, this opens up possibilities to investigate phenomena like the Hadley circulation in the future.

Contents

Chapter 1

Introduction

1.1 Background

According to observations from recent decades the global climate is changing and predictions from various climate models indicate that this trend will likely continue (Pachauri et al., 2014). Additionally, model results indicate that the temperatures on earth will steadily rise. Rising temperatures can result in sea-level rise which impacts people living in deltas, islands and coastal areas. Climate change can also cause more extreme weather; locally the amount of precipitation can change, resulting in droughts or floods. Changing temperature and humidity can additionally impact the habitats of wildlife and the agricultural conditions of farmlands.

Climate change predictions are based on simulations with various models using multiple input scenarios. These studies focus on the transient situation of the climate, as the amount of greenhouse gasses is not constant and the response of the climate lags the changes in greenhouse gas concentrations. Climate simulations therefore aim to find the transient state resulting from changes in parameters such as atmospheric composition or ocean temperature. To reduce model uncertainties and input uncertainties simulations with several quasi-independently developed models with multiple input scenarios are used (Taylor, 2005).

The models used in climate change studies are General Circulation Models (GCM) which use very coarse resolutions of several hundreds of kilometers and a limited amount of vertical levels in simulations over several years. Some of these models take into account changes in oceanic temperatures and oceanic motions as well. Because of these coarse resolutions almost all underlying processes, such as clouds, convective motion, precipitation and radiation have to be parameterized. A large part of the uncertainty in the predictions is caused by the resulting model uncertainties.

Model uncertainties can be reduced by using higher resolution models, which reduces the need for parametrizations, as more of the motions are resolved and processes such as clouds can be simulated more accurately. Clouds are generally much smaller than the resolutions of the GCM model and have to be parametrized. Higher resolutions models can be used to simulate clouds and the motion of air within clouds more directly reducing the need for parametrizations. The interaction of clouds with radiation and the resulting cloud-climate feedback loops are important factors in the climate and clouds are therefore a large source of uncertainties in GCMs (van der Dussen, 2015).

Additionally, convection occurs on scales smaller than the GCM model resolutions and hence GCM models require parametrization of convective motion. Higher resolution models can resolve the convective motions directly. The resulting calculations of air motions are more detailed and hence provide a better representation of the dynamics.

Higher resolution models such as for example cloud resolving models, require more computational power and are therefore currently not directly applicable for climate change predictions. These models however can be used to increase the general understanding of certain smaller scale atmospheric processes, which can be used to verify and adapt the parametrizations of GCMs. One type of higher resolution

models are Large Eddy Simulations (LES) models. These models still rely on parametrizations of atmospheric processes but resolve motions at smaller scales. LES models use high vertical resolutions of several tens of meters and horizontal resolutions of hundreds of meters. This high resolution enables resolving convective motions at more length scales hence reducing the need for subgrid parametrizations for convective motions smaller than the grid size. As LES models require many gridpoints and resolve much more processes compared to GCM models, simulations with LES require more computational power and more computation time. It is therefore unrealistic to assume that LES will be used for climate change modeling within the next decades.

Although LES was proposed in the sixties by Smagorinsky (1963) and LES modeling of the atmospheric boundary layer started in the late sixties by Lilly (1967) and Deardorff (1972), the usability of LES in atmospheric simulations was limited by the availability of computational power. LES was therefore first applied to simpler cases such as the 3D turbulent channel flow by Deardorff (1970). Continuous improvements of computers and emergence of supercomputers provided increased availability of computation time and processor speed. These developments recently (2000s) enabled using LES models to perform long simulations on domains of several thousand cubic kilometers as used in the work of Böing et al. (2012). Eventually, but likely not within the next decades, these simulation times and domain sizes may reach scales that enable simulations of large scale domains as are usually used by GCMs.

LES is often used on smaller domains in the lower atmosphere. To perform simulations on large-scale domains, tests with the current LES models are necessary to determine which parts need to be adapted, what input needs to be provided and what settings need to be used. LES for example is often used on domains in the lowest ten kilometers of the atmosphere whereas GCMs often have the top of the domain positioned at thirty kilometers or higher because these simulations are largely determined by radiation. Increasing the height of the domain may require adaptations in the LES parametrizations in for example the radiative transfer routines. This thesis aims at testing and adapting the LES model to enable atmospheric simulations of higher domains.

1.2 Previous Research

To test and adapt the LES model radiative-convective equilibrium (RCE) will be investigated. Radiative-convective equilibrium is the equilibrium state in which the heating and cooling from radiation and convection balance each other out thus reaching a state in which the temperature no longer changes over time. The hydrological cycle; the evaporation and condensation of water, should be in balance as well. Radiative-convective equilibrium requires timescales of several tens of days. Diurnal and season variations however cause fluctuations in the radiation and hence true radiative-convective equilibrium is never reached in the atmosphere. To calculate radiative-convective equilibrium scientists often use average values of their input parameters to simulate the resulting equilibrium state.

Manabe and Strickler (1964) were among the first to investigate the equilibrium state of the atmosphere in radiative-convective equilibrium. Using a 1-dimensional column model they calculated the radiative equilibrium state by numerically integrating the idealized radiative fluxes. To calculate radiative-convective equilibrium Manabe and Strickler used a convective adjustment by prescribing a critical lapse rate of $6.5^{\circ}C/km$ in the convective layer. Aside from this they determined the sensitivity to changes in atmospheric composition as well. In some of their simulations Manabe and Strickler used simple models for clouds at several levels. Their computations for the convective-radiative equilibrium with clouds were in reasonable agreement with observed temperature profiles. Some of their key results are summarized in chapter A.1 in the appendices.

In the past 50 years however much improvement in numerical simulations and parametrizations have been made. Improvements in modeling and computation power enabled performing simulations in multiple dimensions. In two- and three dimensional models the effects of convection can be calculated instead of prescribing a lapse rate. Improvements in parametrizations of clouds, microphyisical schemes and radiative transfer routines enabled doing radiative-convective equilibrium simulations much more accurately. Because of computational limitations scientists often used two-dimensional models. These models include the vertical dimension and one horizontal dimension. Held et al. (1993) used a two-dimensional cloud-resolving model with explicit moisture convection and showed that their results resembled the observed mean temperature profiles in the tropics quite well. In the same period Sui et al. (1994) used a two-dimensional cloud-resolving model to investigate radiative-convective equilibrium. Their results

showed strong influence of cloud-fields on the water cycle and heat budgets. This stresses the importance of clouds. Some results of Sui et al. and Held et al. have been summarized in appendix A.2.

Two-dimensional models can be used to simulate convective processes that are largely two-dimensional but perform considerably worse in cases with three-dimensional convective processes such as random convection. In these cases three-dimensional models should outperform their two-dimensional counterparts.

Tompkins and Craig (1998) used a three-dimensional cloud-resolving model to investigate radiative-convective equilibrium. They determined the sensitivity of the simulations to changes in sea surface temperature using a cloud-resolving model with a horizontal resolution of 2 kilometers. Other researchers such as Islam et al. (1993) and Robe and Emanuel (1996) used similar models to study the humidity and cloud plots. The simulations of Islam et al. (1993) produced a large entirely cloudy layer at the top of the troposphere. The results of Robe and Emanuel (1996) were similar, but the cloud fraction at the top of the domain was significantly smaller. The results of Islam et al. and Robe and Emanuel can be found in appendix A.3.

Increased availability of computational power enables using higher resolution models to simulate radiative-convective equilibrium more accurately. Large Eddy Simulation models can be used at much higher resolutions than the cloud-resolving models of Tompkins and Craig (1998). This reduces the need for parametrizations of the underlying processes, as more of the convective motions can be resolved. Aside, this also enables simulating clouds at a higher resolution, which should result in improved radiative transfer through the cloud field as compared to the parametrized clouds in lower resolution models. This could also enhance the cloud-radiative feedback on the dynamics. Therefore this thesis will investigate radiative-convective equilibrium with a LES model.

1.3 Radiative-Convective Equilibrium

In previous research such as the research by Manabe and Strickler (1964), Sui et al. (1994) and Tompkins and Craig (1998) radiative-convective equilibrium was investigated. As this is radiation-driven problem, these researchers included a large vertical part of the atmosphere in their simulations. The atmosphere is generally classified into five layers; troposphere, stratosphere, mesosphere, thermosphere and exosphere. Almost all of the convective processes occur in the troposphere, but the effects of the higher layers on radiation are substantial. Therefore a part of the stratosphere has been included in the simulations of these researchers. The higher layers such as the mesosphere, thermosphere and exosphere have very low air densities and hence do not exert much influence on the radiation and hence are not included in the work of these scientists. In this thesis the troposphere and part of the stratosphere will be investigated in the simulations.

The troposphere is the lowest layer of the atmosphere and most of the weather phenomena take place within this layer. In this layer the temperature decreases with altitude. The troposphere is capped by the tropopause above which the stratosphere begins. The exact location of the tropopause depends on the latitude and time of year and is situated at about 9 kilometers at the poles and 17 kilometers in the tropics.

The temperature in the stratosphere is dominated by radiative processes. Due to the relatively large amounts of ozone in the stratosphere this layer has a substantial effect on the shortwave radiation reaching the surface. Absorption of solar UV radiation by ozone causes the temperature in the stratosphere to increase with altitude. The stratosphere is therefore very stably stratified with warmer layers on top of colder layers. Therefore very little mixing occurs between layers. Processes in the stratosphere are hence not dominated by vertical motions but by radiative processes. Combined the stratosphere and troposphere contain the lion's share of the atmospheric mass, approximately 99 % (Salby, 1996).

In radiative-convective equilibrium the radiative and convective processes should cancel each other out. Equilibrium is defined as the situation in which all acting influences are balanced out by others. This state therefore does not change over time. Equilibrium in this sense is never truly reached in the atmosphere as solar insolation varies with time due to diurnal and seasonal fluctuations. Therefore this thesis defines equilibrium as the state of the atmosphere in which the average state will no longer change over time. The time-averaged distributions of water and internal energy (temperature) for example should be approximately constant in equilibrium. If the temperature in the atmosphere is constant over time the atmosphere is in thermal equilibrium. This is reached when there is no net heat transport, which requires balancing of the modes of heat transport.

1.3.1 Heat Transport

Generally speaking three modes of heat transport exists; convection, conduction and radiation. Conduction is generally unimportant in atmospheric sciences as the conductivity of air is very low. Radiation is a very important mode of energy transport in the atmosphere as the climate on earth is largely determined by the radiation from the sun and the absorptive properties of the atmosphere. Radiation is transferred at the speed of light ($3.0 \times 10^8 m/s$) and is the only mode of heat transport that can travel through the vacuum of space. Radiation from the sun is one of the main driving forces of the atmospheric motion.

Inside the lower atmosphere convection; the transport of heat through movements of air, is a dominant mode of heat transport. Convection consists of advection, transport caused by bulk motion of fluids, and diffusion, which is transport from a location with a high concentration to a location with a low concentration. Molecular diffusion or conduction becomes the dominant mode of transport above 100 kilometers but is negligible below this height. Below 100 kilometers most of the diffusion is turbulent diffusion; mixing of air by turbulent motions.

When air moves it transports energy in the form of internal energy. The resulting heat flux is called the sensible heat flux. Moist air transports water as well. Water can exist in a gaseous, solid or fluid phase, all of which occur naturally in the atmosphere. Through phase changes water can change from one phase to another, for example by condensation and evaporation. These phase changes either require energy from the environment (endothermic) or release energy to the environment (exothermic). The water vapor can condensate into a liquid phase, releasing latent heat to the environment. Transport of wet air is hence associated a latent heat flux as well.

Radiation is another important mode of heat transfer. If radiation encounters a molecule the radiation can be absorbed, scattered or reflected. Absorption of radiative energy heats op the molecule. The molecule can release this energy by emitting radiation, as every object at a non-zero temperature does. Hotter objects emit more radiation at shorter wavelengths according to Planck's law.

Optical properties of objects can have a strong dependence on the wavelength of the radiation. This is one of the reasons why scientists often distinguish two types of radiation; shortwave radiation from the sun and longwave (thermal) radiation from objects on earth. Clouds for example absorb longwave radiation, while reflecting shortwave radiation. Heating and cooling by radiation can result in temperature differences which can act as a driving force for air motions. In radiative-convective equilibrium the heat transport from convection and radiation should cancel.

1.3.2 Dynamics

Driving forces are required to make air move. In the vertical direction buoyancy is one of the most important mechanisms. Air, like any other object on earth, experiences a downward force of gravity. The space below the air however is not empty and hence the the column of air below it is compressed increasing the pressure. The pressure is largest at the surface and becomes smaller when moving upwards. Pressure differences give rise to a pressure gradient force. In hydrostatic equilibrium the pressure gradient and gravity forces are in equilibrium. Generally the atmosphere remains close to this state of hydrostatic equilibrium.

Upward movement of air can be created by density differences. To illustrate this a simple model of adiabatic air parcels is used. Adiabatic means that there is no heat exchange between the air parcel and the environment. Suppose that a certain parcel of air is hotter than the surrounding air and hence has a lower density. The parcel experiences the same upward pressure gradient force but a lower gravity force. Therefore this parcel rises and enters a layer with a lower pressure where it expands. Expansion work costs energy and as the parcel is adiabatic the only source of energy is the internal energy of the parcel. Hence the temperature in the parcel drops which makes the temperature of the parcel a function of the height. The parcel continues rising until the density is equal to the density of surroundings and the parcel is at the same temperature as the environment. This produces a temperature profile decreasing with height in the atmosphere. It can be calculated, see appendix C.1, that the temperature of dry air decreases by 9.8°C per kilometer, which is called the dry adiabatic lapse rate (Γ_d). Note that lapse rates are by definition positive for temperatures decreasing with height.

1.3.3 Thermodynamics

In atmospheric sciences potential temperatures are used more often than absolute temperatures T. A big advantage of the potential temperature θ is the fact that potential temperature is conserved in adiabatic processes for dry air. Potential temperature and absolute temperature are related through the Exner function Π. In this formula p is the pressure, p_0 is a reference pressure of $10^5 Pa$, R_d is the gas constant for dry air $287.0 Jkg^{-1}K$ and c_p is the heat capacity of dry air $1004 Jkg^{-1}K$,

$$T = \theta \left(\frac{p}{p_0} \right)^{\frac{R_d}{c_p}} = \theta \Pi. \tag{1.1}$$

The potential temperature of dry air is constant with height for parcels following the dry adiabatic curve. Adding moisture to air has two effects. Firstly, the molar mass of water ($18.02 g/mol$) is less than the average molar mass of dry air ($28.97 g/mol$). Water molecules replace heavier molecules in the air, therefore moist air is lighter than dry air. This effect is incorporated in the virtual potential temperature. The virtual potential temperature θ_v can be used instead of the potential temperature θ in almost all equations as long as the air remains unsaturated. For unsaturated air the virtual potential temperature should be constant with height. The virtual potential temperature is often used as a substitute for the density in buoyancy calculations,

$$\theta_v = \theta \left(1 + \left(\frac{R_v}{R_d} - 1 \right) q_t - \frac{R_v}{R_d} q_l \right). \tag{1.2}$$

Secondly, moist air contains latent energy. Similar to the dry parcel, a wet parcel expands as it rises and likewise this expansion work costs energy. The expansion work causes the temperature of the parcel to drop. However, at a lower temperature the amount of water vapor the air can contain decreases. In the adiabatic model, the total amount of water in the parcel remains the same. As long as the air parcel is unsaturated it will follow the dry adiabatic curve. If the air parcel becomes saturated water vapor will condensate and release latent heat. Releasing latent heat increases the temperature of the air parcel. Therefore the temperature of a wet air parcel decreases less than the temperature of its dry counterpart. The temperature of these parcels will decrease following the saturated adiabatic lapse rate (Γ_s), which is located between $4°C/km$ and $7°C/km$ depending on temperature and pressure of the environment. It is not possible to capture this in a single formula as the saturated water content of the air depends on the temperature, which depends on the saturated vapor content. The lapse rate hence has to be calculated iteratively, see appendix C.1. The saturated adiabatic lapse rate is a positive quantity for temperatures decreasing with height.

The virtual potential temperature of a saturated parcel (θ_v^S) on the other hand will increase with height. Similar to the saturated adiabatic lapse rate, the magnitude of the potential temperature increase depends on the potential temperature and pressure as well.

Both the dry lapse rate and the saturated lapse rate are theoretical concepts, in reality the lapse rate of the atmosphere (Γ_e) is not exactly equal to one of these lapse rates. Lapse rates however are important in determining the stability of the atmosphere. In terms of stability three cases exist; absolutely unstable, conditionally unstable and absolutely stable.

Rising air parcels will follow either the saturated adiabatic curve or the dry adiabatic curve. A saturated parcel will follow the saturated curve, while an unsaturated parcel will follow the dry curve. If the environmental lapse rate is smaller than the saturated adiabatic lapse rate, air parcels following the the dry or saturated adiabatic curve will experience a larger temperature decrease during their ascension than the environment. These air parcels will become colder and hence heavier than the environment. The parcels are negatively buoyant and will start descending in this absolutely stable atmosphere.

If the lapse rate of the environment is higher than the dry adiabatic lapse rate, the temperature will decrease very rapidly with altitude. A rising air parcel will follow the dry or the saturated adiabatic curve and in either case the temperature of the parcel will decrease slower than the environment. The parcel will remain warmer and thus lighter than the environment. Because the parcel is lighter it is positively buoyant and it can continue to rise. This type of atmosphere is called absolutely unstable and clouds can form.

If the lapse rate of the environment is between the dry and the saturated lapse rates the atmosphere is conditionally unstable. A dry air parcel will follow the dry curve and its temperature will decrease more than the environment, which makes the parcel negatively buoyant. A saturated air parcel however will follow the saturated adiabatic curve and the temperature will decrease less than the environment, which makes the wet parcel positively buoyant. In this situation saturated air parcels will rise whereas dry air parcels will descend. The environment is conditionally unstable and clouds can form.

These stability criteria are summarized in table 1.1. The stability criteria are described in virtual potential temperatures as well, as these are commonly used to characterize the stability.

Table 1.1: Stability Characterization

Stability	Virtual Potential Temperature	Temperature Lapse Rate
Absolutely Stable	$\frac{d\theta_v^e}{dz} > \frac{d\theta_v^S}{dz}$	$\Gamma_e < \Gamma_s$
Conditionally Unstable	$0 < \frac{d\theta_v^e}{dz} < \frac{d\theta_v^S}{dz}$	$\Gamma_s < \Gamma_e < \Gamma_d$
Absolutely Unstable	$\frac{d\theta_v^e}{dz} < 0$	$\Gamma_e > \Gamma_d$

Buoyancy-driven convection tends to drive the temperature profiles towards stable values. Other influences however can destabilize this situation. In radiative-convective equilibrium the radiative and convective heat transport should balance. The atmospheric composition however is not uniform; some key species for radiation are not uniformly distributed. Ozone for example is mainly found in the stratosphere. Incoming UV light is absorbed by the ozone in the stratosphere which heats the air causing the temperature in the stratosphere to increase with height. Warm light air hence lies on top of denser cold air, which makes the stratosphere very stably stratified (Salby, 1996). Buoyancy-driven convection is hence very small in the stratosphere.

Whereas radiation stabilizes the stratosphere, it destabilizes the troposphere. Solar and thermal radiation are absorbed at the ground surface. The heated surface emits this energy in the form of latent and sensible heat fluxes as well as longwave radiation. These processes warm the troposphere from below, which tends to destabilize the troposphere. At the top of the troposphere only a limited amount of thermal radiation enters from the stratosphere. The troposphere is much denser and warmer and hence emits quite a lot of thermal radiation. At the top of the troposphere the air hence emits more radiation than received, causing a net radiative cooling and destabilization of the top of the troposphere (Salby, 1996).

Another important factor in determining the temperature are clouds. Clouds are composed of water and are hence strong longwave absorbers. Looking from space clouds are approximately white which indicates that they reflect much of the visible light, as clouds are good shortwave reflectors (Taylor, 2005). By reflecting incoming radiation clouds cool the surface of the earth. Clouds can also act as a thermal blanket, absorbing the longwave thermal radiation coming from the surface and re-emitting a large part back towards the surface. The cloud top is cooled and the cloud base is warmed. Whether the shortwave or longwave effect is stronger depends on the circumstances. Optical properties of clouds also depend on factors such as their height, temperature, water content and angle of the incoming solar radiation, which makes analyzing the effects of clouds more complicated. Aside from the radiative properties clouds have profound effects on the motions of the surrounding air as well.

Rain and other types of precipitation can form in clouds which cools the environment as it evaporates. Precipitation hence results in more transport of water and energy, which stabilizes the atmosphere at some places but might destabilize it at other locations.

1.4 Research Objectives and Questions

Previous sections explained that convection and radiation together determine the equilibrium state of the atmosphere. The scope of this thesis is to investigate the state of an atmosphere in radiative-convective equilibrium. This will be investigated using LES models. For this specific research the DALES model, which will be further explained in subsequent chapters, will be used. The employed radiative transfer code (RRTMG) has been tested and verified in GCM models (Mlawer et al., 1997). The implementation of this radiative transfer code in the LES model however has only been used in a limited amount of cases such as in the research of van der Dussen (2015). Since the problem is radiation-driven high domains (30 kilometers) need to be used. To test whether the implementation of this radiative transfer code is applicable to these domain heights, simulations without convection will be performed as well. The resulting equilibrium state in absence of convection is a radiative equilibrium. The simulations from Manabe and Strickler (1964) will be used for comparison. Additionally the effects of of the atmospheric composition on radiative equilibrium will be tested as well.

Investigating radiative-convective equilibrium is the main goal of this thesis. The radiative-convective equilibrium state depends on the imposed forcing and boundary conditions. Radiative-convective equilibrium will be determined at several values of the surface temperature. The resulting energy balance and atmospheric profiles will be investigated and compared to other research. This leads to the following research objective and questions:

Research Objective: Simulate and investigate radiative-convective equilibrium with DALES.

- How does the atmosphere look in radiative equilibrium?
- What is the effect of atmospheric composition on the radiative forcing?
- What is the effect of convection on the atmospheric equilibrium?
- How do the atmosphere and energy balance respond to a change in sea surface temperature?

1.5 Outline

In this thesis the radiative-convective equilibrium is investigated using the Dutch Atmospheric Large Eddy Simulation (DALES) model. In the following chapter the DALES model as used for these simulations will be explained. In the two subsequent chapters the setup for simulations in radiative equilibrium and radiative-convective equilibrium will be described. After these chapters the results of these radiative and radiative-convective simulations will be analyzed in separate chapters. This thesis will conclude with a chapter dedicated to the conclusions and an outlook.

Chapter 2

Model Description

2.1 DALES

In the case of atmospheric physics the Navier-Stokes equations need to be solved, for which no exact solutions exists for situations encountered in the atmosphere according to current knowledge. These equations are therefore often solved numerically. The domain of simulation is divided into volume elements called a grid. By discretizing the equations and iterating the resulting equations a numerical solution to the problem can be found. Methods like Direct Numerical Simulation (DNS) can solve this problem almost exactly. DNS is often applied to problems with laminar flows and turbulent flows with low Reynolds numbers.

In the atmosphere flows are often turbulent consisting of irregular swirls of motions called eddies. The problem with these turbulent flows in the atmosphere is that the length scales of the relevant motions are spread out over an enormous range. Turbulent eddies responsible for the viscous dissipation of energy have scales of millimeters, whereas the largest eddies are in the order of a kilometer depending on the size of the atmospheric boundary layer. The smallest motions resolved by any numerical method depend on the size of the grid; motions that are smaller than the size of the grid will not be resolved. To simulate the small dissipating eddies one has to use a grid size close to a millimeter, but to simulate atmospheric processes one has to use this grid on domains of several kilometers. To solve this problem almost exactly DNS can be applied, which would require more than 10^{23} grid boxes for the simulations of this thesis. Although advances in computational power and memory enable performing larger and larger simulations, the current state of technology is by far not sufficient to perform adequate simulations of small eddies on the domains required by atmospheric problems using DNS.

To enable simulations of turbulent flows on these domain sizes Large Eddy Simulations (LES) are often used. Rather than resolving the smaller turbulent eddies, LES solves only the larger eddies in the order of several tens of meters. Smaller motions are filtered out and are not resolved in the simulation. The effect of these smaller motions however is very important for mixing and dissipation, hence these effects have to be incorporated in the model. To account for these effects LES uses subgrid models to parametrize the effects of the eddies without having to resolve them. This enables LES to solve atmospheric problems with much larger grid sizes as compared to DNS, reducing the computational costs substantially.

This thesis uses DALES, which is an acronym for Dutch Atmospheric Large Eddy Simulation. DALES is an atmospheric simulation model developed by the University of Utrecht, Royal Dutch Meteorological Institute (KNMI), Wageningen University and Delft University of Technology (Heus et al., 2010a). The most recent version of DALES is the DALES 4.0 version which is written in Fortran 90[1]. For this specific project a version modified by van der Dussen was used. A large difference between this version and the source DALES 4.0 version is the implementation of a new radiation scheme (van der Dussen, 2015).

[1]The code for DALES 4.0 can be found online on GitHub (https://github.com/dalesteam/dales.git)

DALES contains several options to allow the user to choose which processes and which parametrizations to include and which to exclude. Several schemes for processes such as microphysics, advection and radiation are implemented. Aside from this the user needs to specify the initial conditions, the boundary conditions at the surface and the radiative input at the top of the domain. It is not necessary to specify boundary conditions at the edges of the domain, as DALES utilizes horizontally periodic boundary conditions. Therefore quantities advected out of the domain on one side enter the domain on the other side.

DALES can be used to simulate atmospheric processes on multiple processors at the same time, which allows for much faster computations. To use multiple processors the computation domain is divided horizontally into several subdomains. Each processor performs the computation on the columns of its respective subdomain. For points on the edges of the subdomains it is necessary for the processors to transfer the necessary information to each other.

For the interested reader, more information about DALES can be found in the work of Heus et al. (2010a) and in the manual by Heus et al. (2010b). It should be noted that the current version of DALES is slightly altered as compared to the information in these sources. In the following sections several processes in DALES will be explained.

2.2 Prognostic Variables

DALES calculates several variables through time integration. These prognostic variables include the velocities u, v and w in m/s, the potential temperature θ_l in Kelvin, the total water specific humidity q_t in kg/kg as well as the subfilter-scale turbulence kinetic energy e in m^2/s^2. These simulations use microphysics and hence the rain water specific humidity q_r in kg/kg and the rain droplet number concentration N_r in m^{-3} are calculated as well (Heus et al., 2010a). Several of these variables and derived variables will be explained in the following sections.

2.2.1 Humidities

One of the important variables for the composition of the atmosphere is the total water specific humidity q_t. This variable is the mass of both cloud water and vapor water per mass of dry air. Air almost always contains water, but clouds need not be present. Only if the air is supersaturated liquid water can be present. The thermodynamic modules of DALES calculate the saturated water specific humidity as a function of temperature and pressure. If the total water specific humidity is larger than the saturated water specific humidity liquid water is present. The presence of a nonzero liquid water specific humidity q_l signals the presence of clouds. Aside from the total water specific humidity a the liquid water specific humidity q_l is calculated as well. This can be used to calculate the water vapor component q_v. In absence of precipitation total water specific humidity q_t is a conserved variable,

$$q_v = q_t + q_l. \tag{2.1}$$

Note that this equation does not contain ice or rainwater. In calculations with ice DALES calculates the ice content indirectly by calculation of the ice-liquid partitioning. Rainwater is not included in the value of either q_t or q_l but is stored as a separate scalar field q_r.

2.2.2 Temperatures

The temperature prognostic variable in DALES is the liquid potential temperature θ_l. The liquid potential temperature is used as a prognostic variable in DALES, as it is conserved in reversible adiabatic motion with phase changes. Liquid potential temperature is not conserved in situations with precipitation and radiation.

In atmospheric sciences potential temperatures are used more often than the absolute temperature T. Conversion from potential temperatures to absolute temperatures is commonly done using the Exner function Π. To convert the liquid potential temperature to the absolute temperature formula 2.2 can be used,

$$T \cong \left(\theta_l + \frac{L}{c_p \Pi} q_l\right) \left(\frac{p}{p_0}\right)^{\frac{R_d}{c_p}} \cong \left(\theta_l + \frac{L}{c_p \Pi} q_l\right) \Pi. \tag{2.2}$$

With respect to the stability of an atmospheric layer the virtual potential temperature θ_v is often used. This variable is related to the liquid potential temperature through the following equation, in this equation R_v is the gas constant for water vapor of $461.5 J kg^{-1} K$,

$$\theta_v = \left(\theta_l + \frac{L}{c_p \Pi} q_l\right) \left(1 + \left(\frac{R_v}{R_d} - 1\right) q_t - \frac{R_v}{R_d} q_l\right). \tag{2.3}$$

2.3 Governing Equations

2.3.1 Mass Conservation

One of the most important equations in fluid dynamics is the continuity equation which represents mass conservation. The continuity equation is described in equation 2.4. In this formula ρ is the density, t is the time, u_j are the components of the velocity and x_j are the Cartesian coordinates over which a sum has to be taken,

$$\frac{\partial \rho}{\partial t} + \frac{\partial \rho u_j}{\partial x_j} = 0. \tag{2.4}$$

In DALES the anelastic approximation has been implemented by Böing (2014). It is assumed that the flow speed is much smaller than the speed of sound and that the vertical length scale of the flow is not shallow compared to the scale height of the atmosphere, which is in the order of kilometers. Hence density can be assumed to be a function of height x_3 only. This leads to the anelastic continuity equation where u_3 represents the velocity in the vertical x_3 direction,

$$\rho = \rho_0 \left(x_3\right), \tag{2.5}$$

$$\rho_0 \left(x_3\right) \frac{\partial u_j}{\partial x_j} + u_3 \frac{\partial \rho_0}{\partial x_3} = 0. \tag{2.6}$$

In DALES the anelastic continuity equation is used to solve the pressure perturbations to achieve closure using a Poisson solver. Moreover, the slab-averaged vertical velocity is set to zero and periodic boundary conditions are used. Mass is therefore automatically conserved.

2.3.2 Momentum Conservation

Another very important set of equations in the field of fluid dynamics is the set of equations representing conservation of momentum. The sum is implicit over j and the subscript i is the Cartesian coordinate $\{1, 2, 3\}$ for which direction the momentum equation is calculated. The left hand side of this equation is change in velocity due to acceleration and convection respectively. The right hand side of this equation contains the exerted forces; pressure, Coriolis and gravity plus possible other forces,

$$\frac{\partial u_i}{\partial t} + u_j \frac{\partial u_i}{\partial x_j} = -\frac{1}{\rho} \frac{\partial p}{\partial x_i} - 2 \epsilon_{ijk} \Omega_j u_k - g \delta_{i3} + F_{ijk}. \tag{2.7}$$

The second term on the right hand side in equation 2.7 is the Coriolis force. This is a fictitious force caused by the rotation of the earth. The Coriolis force changes the direction of the velocities but does not affect the magnitude of the velocities. Dominant winds such as the trade winds and westerlies are caused by the Coriolis force. In formula 2.7, Ω_j is the angular momentum vector of the earth and ϵ_{ijk} is the 3-dimensional Levi-Civita permutation tensor.

The third term in equation 2.7 is the gravitational force, which gives rise to buoyancy fluxes. As DALES uses a Cartesian coordinate system with the x_1 and x_2 coordinate in the horizontal plane, gravity acts solely in the x_3 direction. The symbol g in equation 2.7 is the acceleration of gravity, which is assumed to be a constant $9.81 m/s^2$ and δ_{i3} is the Kronecker delta function.

From equation 2.7 the modified equation 2.8 can be derived. In this equation the drag of precipitation has been added by Böing (2014), which depends on the specific rain water humidity q_r. Viscous effects of air are neglected as is common in atmospheric physics. The subscripts e indicate an environmental variable, e.g. the environmental hydrostatic state. This is the average state, which may differ from the base state indicated with subscripts 0. A derivation of this equation can be found in the appendix C.2,

$$\frac{\partial u_i}{\partial t} = -\frac{1}{\rho_0}\frac{\partial \rho_0 u_i u_j}{\partial x_j} - \frac{\partial}{\partial x_i}\left(\frac{\delta p}{\rho_e}\right) + g\delta_{i3}\left(\frac{\theta_v - \theta_{v,e}}{\theta_{v,e}} - q_r\right) - 2\epsilon_{ijk}\Omega_j u_k. \tag{2.8}$$

The terms on the right hand side are; advection, forces due to pressure fluctuations, buoyancy, rain drag and Coriolis force. Instead of expressing buoyancy in terms of density fluctuations, which are difficult to measure and calculate, buoyancy is expressed in terms of virtual potential temperature.

These simulations have been carried out using DALES. As explained in previous sections (see section 2.1) LES simulations do not simulate motions at all scales. The smallest simulated motions are limited by the resolution of the domain. Motions smaller than this resolution are parameterized instead in the subgrid model. Mathematically this can be represented by applying a low-pass filter to the calculated variables. Therefore instead of solving equation 2.8 a filtered version of this equation is solved. In this equation the variables with a tilde are filtered variables(Böing, 2014),

$$\frac{\partial \widetilde{u_i}}{\partial t} = -\frac{1}{\rho_0}\frac{\partial \rho_0 \widetilde{u_i}\widetilde{u_j}}{\partial x_j} - \frac{\partial}{\partial x_i}\left(\frac{\widetilde{\delta p}}{\rho_e}\right) + g\delta_{i3}\left(\frac{\widetilde{\theta_v} - \theta_{v,e}}{\theta_{v,e}} - \widetilde{q_r}\right) - 2\epsilon_{ijk}\Omega_j\widetilde{u_k} - \frac{1}{\rho_0}\frac{\partial \rho_0 \tau_{ij}}{\partial x_j} - \frac{1}{\rho_0}\frac{\partial \frac{2}{3}\rho_0 e}{\partial x_j}. \tag{2.9}$$

Modeling with LES therefore results in two additional force terms. The τ_{ij} is the anisotropic subfilter scale stress tensor and e is the subfilter scale turbulent kinetic energy. The fifth term on the right hand side represents turbulent diffusion created by the subgrid. The sixth term on the right hand side is the result of making the stress tensor trace free; it is almost always included in the modified pressure (π).

This section is not meant to function as a complete overview of the principle of LES or DALES. More details about the LES filtering in DALES can for example be found in sources such as Heus et al. (2010a) or Böing (2014).

2.4 Boundary Conditions

In DALES the slab-averaged vertical velocity is always zero. At the surface the fluctuations in the vertical velocity are zero as well; the vertical velocity is zero at every gridpoint on the surface. The resolved surface fluxes at the surface are hence zero as well. The moisture and heat surface fluxes are therefore entirely determined by the subgrid scheme. The formulations of these fluxes have been set as to obey Monin-Obukhov similarity theory. Using the prescribed surface temperature and roughness lengths the fluxes are iteratively solved (Heus et al., 2010a).

At the top of the domain the slab-averaged vertical velocity and the fluctuations in the vertical velocities are both set to zero. The horizontal velocities are constant in the vertical direction at the top of the domain. Values of scalars such as potential temperature, water mixing ratio and other scalar fields are extrapolated at the top level,

$$\frac{\partial u}{\partial z} = \frac{\partial v}{\partial z} = 0; w = 0; . \tag{2.10}$$

At the sides of the domain horizontally periodic boundary conditions are applied. Moisture and heat can hence enter and exit the domain only at the top and surface.

2.5 Radiation

Radiative transfer is governed by the Radiative Transfer Equation (RTE) as displayed in formula 2.11. This equation determines the intensity of a certain wavenumber of radiation traveling through the medium. To get the amount of radiative energy impinging on a surface by radiation this equation has to be integrated over all wavenumbers and over all solid angles. On the left hand side this equation contains the change of radiative intensity in time and the change of intensity with space along a line. The change of intensity in time is often ignored. On the right hand side the source and sink terms are located. These terms are emission, absorption, out-scattering and in-scattering (Modest, 2013b). In this formula I_η is the intensity at a certain wavenumber η, c is the speed of light, s is the position, κ_η is the absorption coefficient, $I_{b\eta}$ is the blackbody emission of the medium, $\sigma_{s\eta}$ is the scattering cross-section and Φ_η is the scattering phase function which has to be integrated over all solid angles Ω_i,

$$\frac{1}{c}\frac{\partial I_\eta}{\partial t} + \frac{\partial I_\eta}{\partial s} = \kappa_\eta I_{b\eta} - \kappa_\eta I_\eta - \sigma_{s\eta} + \frac{\sigma_{s\eta}}{4\pi}\int_{4\pi} I_\eta(\hat{\boldsymbol{s_i}})\Phi_\eta(\hat{\boldsymbol{s_i}}, \hat{\boldsymbol{s}})d\Omega_i. \tag{2.11}$$

Earth's atmosphere does not have a uniform composition; concentrations of gasses such as ozone, water vapor and carbon-dioxide change with height. Moreover temperature and density of the atmosphere are a function of height as well. These aspects make solving the radiative transfer equation even more complicated.

Solving the radiative transfer equation (RTE) exactly for the atmosphere is virtually impossible, hence the radiation is simplified. Firstly the radiation is split up into shortwave (SW) and longwave (LW) radiation. Shortwave radiation is emitted by the sun and is not emitted by any object in the atmosphere. Longwave radiation consists of thermal radiation as emitted by the atmosphere and the ground. Since the mean radiating temperature of the sun (approximately 5780K) and the mean radiating temperature of the earth (approximately 255K) differ substantially the amount of overlap in their spectra is limited (Taylor, 2005). The optical properties of clouds and atmospheric gasses are dependent on wavelength. By splitting the radiation into multiple wavelength bands it is easier to calculate the effect of clouds and gasses on the incoming radiation and the two types of radiation can be treated separately.

To further simplify the problem a simplification is used, instead of positioning the sun at an angle with respect to the surface, the sun is positioned right above the domain. The emitted solar radiation hence travels only in the vertical direction. To compensate for the fact that the sun is usually positioned at a non-zero zenith angle the distance traveled by the radiation is divided by the cosine of the zenith angle. This results in the correct pathlength for the radiation, although the shadows of clouds will be created at the wrong position, namely right below the clouds. This approximation greatly simplifies the calculations for the direct beam of shortwave radiation from the sun.

Scattered and refracted shortwave radiation and thermal longwave radiation travel at a myriad of different angles. To calculate the effects of this diffuse radiation one still has to integrate over all solid angles to calculate contributions from every direction. To remove this integral a two-stream approximation (TSA) is used; radiation goes up or down, but does not go sideways. Angular dependent quantities are replaced by hemispherical averaged quantities (i.e. integrated over a 2π solid angle). TSAs are applicable if the variations in quantities such as temperature in the vertical direction are larger than variations in the horizontal direction, which is generally the case in atmospheric physics.

Longwave radiation is split into an upward and a downward component of diffuse longwave radiation. The treatment of shortwave radiation is somewhat more complicated, as shortwave radiation consists of a direct beam from the sun as well as diffuse fluxes from scattering. To account for the effects of multiple scattering by clouds and gasses the shortwave radiation is split into a direct component traveling at a single angle as well as two diffuse fluxes of up- and downward shortwave radiation (Räisänen, 2002). The two-stream approximation is captured in the following equations 2.12, 2.13 and 2.14 in which $F^\uparrow$ and $F^\downarrow$ are the up- and downward diffuse fluxes, S is the direct solar radiation, μ_0 is the cosine of the zenith angle, τ' is the scaled optical depth and the α coefficients are the factors describing the scattering and absorption processes (Räisänen, 2002). The value of the α coefficients depends on the atmospheric composition and the utilized TSA method. In DALES the Practical Improved Flux Method (PIFM) developed by Zdunkowski et al. (1980) is used. These formulas can also be used for longwave radiation, albeit without the S as there is no direct component of longwave radiation and with different α coefficients since optical properties are often spectrally dependent,

$$\frac{dF^{\uparrow}}{d\tau'} = \alpha_1 F^{\uparrow} - \alpha_2 F^{\downarrow} - \alpha_3 \frac{S}{\mu_0}, \tag{2.12}$$

$$\frac{dF^{\downarrow}}{d\tau'} = \alpha_2 F^{\uparrow} - \alpha_1 F^{\downarrow} + \alpha_4 \frac{S}{\mu_0}, \tag{2.13}$$

$$\frac{dS}{d\tau'} = -\frac{S}{\mu_0}. \tag{2.14}$$

Another advantage of using the TSA is in the numerics of DALES. The domain in DALES consists of a 3-dimensional grid. Grids have a constant spacing in the x- and y-direction and variable spacing in the z-direction. By confining the radiation to up- and downward movement radiation in a column does no longer depend on the situations in adjacent columns. The RTE can hence be solved for each column individually. Especially in cases of parallel computing this is more efficient, as the radiative transfer solver does not require information on adjacent columns, which may reside in other processors. A disadvantage of this simplification is the fact that no horizontal radiative fluxes are calculated. Radiation therefore does not reduce variations in temperature within a horizontal slab, but often convection or gravity wave damping is well able to reduce these variations.

Even with these simplifications solving the RTE is still computationally very expensive as the atmosphere is inhomogeneous and an integration has to be carried out over all wavelengths. Hence DALES uses the Rapid Radiative Transfer Model for General Circulation Models, or RRTMG as developed by the U.S. based company AER (Atmospheric and Environmental Research). This is a slightly altered version of the extensively validated RRTM model in the sense that is has been made computationally less expensive to operate, enabling implementation in GCM models. RRTM is a radiative transfer model utilizing the properties of correlated-k distributions (Mlawer et al., 1997).

Absorption spectra consist of many fine lines because molecules absorb only specific wavelengths. The resulting fine line spectra are therefore highly irregular. To solve the RTE these distributions have to be integrated over all wavelengths which results in complicated numerical integration over many spectral lines. The method of k-distributions transforms the integral over wavelengths to an integral over absorption coefficients, which results in a monotonically increasing function in terms of so called g-points. This function is much smoother and numerical integration can be conducted using only a small amount of points. To apply this method to radiative transfer over larger parts of the spectrum the spectrum is split up into spectral bands with some overlap. RRTMG uses 14 bands for the SW radiation ($820 - 50000 cm^{-1}$) and 16 bands for the LW radiation ($10 - 3250 cm^{-1}$).

These g-points can be tabulated for these spectral bands for a certain temperature. To apply this method to inhomogeneous paths the assumption is made that the value of the absorption coefficients at different temperatures and pressures are correlated (Fu and Liou, 1992). Use of correlated k-distributions greatly reduces the required computational power and provides very accurate results. A more extensive explanation of correlated-k distributions goes beyond the scope of this thesis, but more information can be found in papers such as Modest (2013a).

The RRTMG radiative transfer code calculates the effects of the entire atmospheric column on the radiation. In most LES simulations the LES domain will not contain the entire atmospheric column. Therefore RRTMG adds a second domain on top of the LES domain; this "backrad" domain is only used in the radiative calculations. This domain contains, water, ozon and other trace gasses but clouds are absent in this domain. The composition and the height of this domain depends on the user-provided input. At the top of the domain shortwave radiation from the sun enters the domain. Using this method a more representative longwave-shortwave composition of the radiation entering the LES domain is acquired.

Reflection of radiation at the ground surface depends on the albedo, which determines the fraction of the radiation that is reflected. For the non-diffuse components of the radiation the albedo is a function of the zenith angle. Additionally the surface temperature and emissivity determine the amount of upward emitted longwave radiation. The total amount of upward radiation hence consists of a reflected and an emitted component. The non-reflected part of the downward longwave and shortwave radiation is absorbed. In simulations with a constant surface temperature the heating from the absorbed radiation at the surface is neglected.

2.5.1 Solar Zenith Angle

Important parameters of choice in radiation-driven simulations are the parameters defining the radiation of the sun. For simulations in DALES without diurnal variations one has to choose both the effective solar constant as well as the zenith angle of the sun. The effective solar constant defines the intensity of the solar radiation at the top of the atmosphere. Although the exact value of the solar intensity is not constant, as it depends on solar activity and on the earth sun-distance, a commonly accepted value is 1368 W/m^2.

In DALES the sun is positioned right above the simulation domain, but in reality the sun is positioned at an angle with respect to the point directly overhead called the zenith angle. This zenith angle affects the amount of radiation reaching the surface in multiple ways. Firstly, the intensity of the solar constant is the intensity in a plane perpendicular to the direction of propagation of the solar radiation. Solar radiation rarely travels in a direction perpendicular to the ground surface, hence the solar energy is distributed over a surface area depending on the zenith angle.

Closely related to this is the path length of the radiation, radiation emanating from a sun close the horizon has to travel a longer distance in the atmosphere, hence more of the radiation will be absorbed or scattered. Moreover, scattering properties of surfaces and clouds can also depend on the zenith angle of the incoming radiation.

The position of the sun is not constant throughout the year, the sun is positioned closer the horizon in the winter months and is positioned higher in the sky during summer months. This is described by the declination angle δ. The declination angle describes the position of the sun relative to the earth. As the axial tilt ϵ_{earth} of the earth is approximately a constant -23.45°, the declination angle is mainly determined by the day of the year N. Since the declination angle changes slowly with day of the year, it can safely be assumed that this angle is constant throughout the day. This is summarized in formula 2.15,

$$\delta = \arcsin(\sin(\epsilon_{earth}) \sin(4.88 + 0.172N)). \tag{2.15}$$

Near the equator the sun is positioned higher in the sky compared to regions closer to the poles. This causes the equatorial regions to receive more solar insolation than the polar regions throughout the year. This effect is captured in the latitude ϕ dependence of the zenith angle.

The third variable determining the zenith angle is the time of day. At solar noon the sun is positioned at the highest point whereas it is positioned at the horizon during sunset and sunrise. It is often easier to convert the time to an angle; also called the hour angle h. This angle varies from $-\pi$ to π throughout the day. The solar intensity before $-h_0$ and after h_0 is 0, since the sun is below the horizon. The value of h_0 can be calculated using formula 2.16,

$$\cos(h_0) = -\tan(\phi)\tan(\delta). \tag{2.16}$$

The solar zenith angle θ_s can be calculated using formula 2.17. Literature often uses the cosine of the zenith angle, expressed by μ_0,

$$\mu_0 = \cos(\theta_s) = \sin(\phi)\sin(\delta) + \cos(\phi)\cos(\delta)\cos(h). \tag{2.17}$$

In these experiments an equilibrium situation is investigated. The atmosphere however is usually not in equilibrium because of the diurnal cycle. The relative motion of the earth to the sun changes the intensity of the solar radiation at the surface throughout the day. In equilibrium studies it is often beneficial to remove this diurnal variation to reach an equilibrium state faster and to more directly observe the intrinsic variations of the radiative-convective equilibrium (Bretherton et al., 2005; Wing and Emanuel, 2014). This is reached by fixing the zenith angle and the effective solar constant. The use of effective solar constants and fixed zenith angles is often employed in papers such as in Tompkins and Craig (1998), Bretherton et al. (2005) and Wing and Emanuel (2014). These papers refer to the paper of Tompkins and Craig (1998) who noticed that averaging the diurnal cycle over a day would cause undesirably long path lengths, but did not provide a calculation of their zenith angle and solar constant. The derivation of the values of these constants is explained extensively in appendix C.3 and a short derivation will be provided in the remainder of the section.

It is desirable for the simulations to have the same amount of incoming radiation as to get the same amount of incoming energy. Therefore the product of cosine of zenith angle μ_0 and effective solar constant needs to equal the daily averaged intensity as described in formula 2.18. The factor 2π is due to the fact that the hour angle goes from $-\pi$ to π. The ratio ${R_0}^2/{R_E}^2$ represents the actual earth-sun distance divided by the mean earth-sun distance, for this ratio data from NASA have been used (NASA, 2011),

$$S_0^* \overline{\mu_0} = \frac{1}{2\pi} \int_{-h0}^{h0} S_0 \frac{{R_0}^2}{{R_E}^2} \cos(\theta_s) dh. \tag{2.18}$$

This formula constrains the product of zenith angle and solar constant but not their individual values. In older papers such as Manabe and Strickler (1964) both zenith angle and solar constant were divided by two to get a globally averaged solar intensity. This however corresponds to a sun that is always setting, which means that the path length of the radiation is overestimated. Moreover the scattering properties of clouds also depend on the zenith angle.

In reality most of the sunlight enters when the sun is located high in the sky. This effect is especially important in studies with clouds as researched by Cronin (2014). Hence better results can be achieved by weighting the zenith angle with the amount of incoming radiation, using the insolation-weighted zenith angle. Radiative transfer simulations of Cronin (2014) using RRTM showed that more accurate results could be achieved by using the insolation-weighted zenith angle. His simulations showed that using an insolation-weighted zenith angle resulted in albedos closely resembling the absorption of the cloudy atmosphere. This angle can be calculated by integrating the product of the cosine of the zenith angle and the insolation and dividing this by the integral of the insolation as described in formula 2.19 which can be simplified to 2.20,

$$\overline{\mu_0} = \frac{\int_{-h_0}^{h_0} S_0 \frac{{R_0}^2}{{R_E}^2} \cos(\theta_s) \cos(\theta_s) dh}{\int_{-h_0}^{h_0} S_0 \frac{{R_0}^2}{{R_E}^2} \cos(\theta_s) dh}, \tag{2.19}$$

$$\overline{\mu_0} = \frac{\int_{-h_0}^{h_0} \cos(\theta_s)^2 dh}{\int_{-h_0}^{h_0} \cos(\theta_s) dh}. \tag{2.20}$$

Using the resulting insolation-averaged value of the cosine of the zenith angle in formula 2.18 provides a value for the effective solar constant in simulations without diurnal variations. A complete derivation can be found in appendix C.3. In this appendix the working formulas of equations 2.18 and 2.20 can be found in equations C.58 and C.60.

Chapter 3

Setup of Radiative Equilibrium Simulations

To investigate radiative equilibrium, modifications to DALES were made, as DALES has not specifically been written to perform simulations towards radiative equilibrium. These modifications enable removal of motions of air and are used to force radiative equilibrium in the atmosphere. First these modifications will be discussed. Afterwards the domain setup and the input conditions are explained.

3.1 Modifications

3.1.1 Radiative Equilibrium

Apart from investigating radiative-convective equilibrium (RCE) the situation in radiative equilibrium has also been researched. At the top of the domain the incoming solar radiation is prescribed. This radiation enters the domain and through absorption, scattering and emission the amount of radiation and the shortwave-longwave composition of the radiation changes as the radiation travels towards the surface. At the ground surface a percentage of the incoming radiation is reflected and longwave radiation is emitted.

Radiation changes the temperature of the atmosphere if it is absorbed or emitted. In DALES the heating is calculated by determining the up- and downwards shortwave and longwave fluxes. The flux difference across a grid cell determines the radiative heating rate. Shortwave radiation generally causes radiative heating, whereas longwave radiation mostly causes radiative cooling. In thermal equilibrium the temperature in a grid cell does no longer change, hence the longwave cooling and shortwave heating balance. This is equivalent to stating that the net radiative flux does not change with height. In other words, the net radiative flux should be divergence free.

This thermal equilibrium is not necessarily a radiative equilibrium, as radiative equilibrium does not only require a divergence free net radiative flux, but this flux should be zero at every height. The net flux should be zero, as the amount of incoming radiation should equal the amount of outgoing radiation at the top of the atmosphere for the atmosphere to be in equilibrium. If the temperature in DALES is determined by the model the potential temperature of the ground surface is set equal to the potential temperature of the first level. In radiative equilibrium sharp temperature gradients near the surface can exist and this method of determining the surface temperature is no longer correct. To achieve radiative equilibrium the amount of incoming radiation needs to equal the amount of outgoing radiation as displayed in formula 3.1. All radiative fluxes in this equation are positive, although in DALES downward fluxes have negative values,

$$0 = SW^{\downarrow} - SW^{\uparrow} + LW^{\downarrow} - LW^{\uparrow}. \tag{3.1}$$

To specify the boundary condition at the surface, the surface temperature was made a function of the amount of incoming and outgoing shortwave radiation and incoming longwave radiation as seen in formula 3.2. In this formula σ is the Stefan-Boltzmann constant and ϵ is longwave emissivity. Part of the incoming longwave radiation is reflected as captured by the $(1-\epsilon)$ factor. In the radiative equilibrium simulations an emissivity ϵ of 0.898 was used corresponding to the work of Manabe and Strickler (1964). In the radiative-convective simulations however the default value of 0.95 is used,

$$\sigma\epsilon\left(\frac{\theta_{ls}}{\Pi}\right)^4 = SW_s^{\downarrow} - SW_s^{\uparrow} + (1-\epsilon)\,LW_s^{\downarrow}. \tag{3.2}$$

3.1.2 Pressure

The radiative code uses pressure as the vertical coordinate. This pressure is used to determine the path length of the radiation and hence the amount of absorbed and scattered radiation. The pressure however is initialized only once, at the start-up of the radiation code. Usually the pressure in a simulation will not change that substantially during a simulation. In runs with radiative equilibrium the temperature can change substantially and hence the assumption that the pressure will not change substantially during a simulations is not valid.

At the initialization the pressure at every altitude is determined and hence the path of air for the RRTMG code has been determined. This determines the pressure path length of the grid boxes. Suppose that the initial atmosphere is much cooler than the end-situation. During the simulation the air will become warmer and hence the column of air should expand which changes the pressure of the air. The pressure at the ground surface is fixed and therefore the column of air expands upwards and the pressures at every altitude except the ground surface increase. This means that the pressure gradient dP/dZ becomes smaller; e.g. the air becomes thinner.

In the radiative transfer however, the pressure at each grid box has been determined only during the initialization and therefore a too high pressure path length is used, e.g. the radiation code calculates the transfer through cold dense air instead of warm lighter air. Therefore too much radiation is absorbed inside the grid box. If the initial situation would have been warmer, the pressure as a function of the altitude would have been different and hence different pressure path lengths would have been used in the model. This results in an undesired situation; the final temperature in radiative equilibrium depends on the initial situation because of the pressure initialization in the radiative transfer routine.

This problem can be resolved by modifying DALES. The pressure in DALES is calculated continuously and changes with temperature, the problem in this case is the fact that this pressure is not updated in the RRTMG radiative transfer code. Therefore the DALES code is modified. Instead of initializing the pressure only at the initialization phase, the pressure in the radiative code is now initialized once every radiation time-step. This can result in problems with the "backrad" domain if the pressure inside the LES domain decreases while the pressure in the "backrad" domain remains constant. The pressure in the LES domain could in this case become lower than in the "backrad" domain above, which results in errors in the radiative transfer code as the pressure path length could become negative.

This problem has been averted by updating the pressure levels of the "backrad" domain as well should the pressure inside the LES domain become lower than the lowest pressure in the "backrad" domain. Therefore the radiative equilibrium state does no longer depend on the initial temperature profiles, as should be the case in equilibrium studies.

3.2 Domain Setup

In radiative equilibrium the only forcings are the radiative forcings. Therefore all other forcings have been removed from the simulations. This means turning off the advection, subgrid convection, Coriolis forces and other forces such as buoyancy. Moreover the surface fluxes and air velocities are all set to a value of zero.

Since air motion is absent it is not necessary to use a large domain. A single column simulation like in the calculations of Manabe and Strickler (1964) would suffice for these simulations. The minimal possible grid size in DALES however is a 2x2 grid. Because of the periodic boundary conditions all 4 columns are exactly the same. Hence using these 4 columns in DALES is effectively the same as using a single column model.

To simulate this a non-equidistant grid of 158 points has been used. This grid starts at a vertical spacing of 40 meters, which is stretched by 2.5% until the grid has a vertical spacing of 200 meters. The vertical spacing remains at 200 meters until a height of 12 kilometers is reached, after which the grid stretches by 1% until a height of approximately 30 kilometers. This grid has been created specifically for the simulations for radiative-convective equilibrium, more information can hence be found in the following chapter. For consistency the same grid is used in both the radiative equilibrium experiments and the radiative-convective experiments. A plot of the vertical grid spacing versus height can be found in appendix D.1.

Table 3.1: Radiative Equilibrium: Domain

Variable	Value
Horizontal Grid Points	2×2
Horizontal Domain Size	$25km \times 25km$
Vertical Grid Points	158
Vertical Domain Size	30km

3.3 Settings and Input

These simulations were inspired by the classic paper of Manabe and Strickler (1964) and hence many of the input settings are approximately the same as in their paper. These simulations were performed for a latitude of 35° N in April. Manabe and Strickler used a fixed solar zenith angle of 60° and a solar constant of 2.00 Langley per minute, equivalent to 1395 W/m^2. Combined with 12 hours of light per day this results in an effective solar constant of 697 W/m^2. Note that an insolation-weighted angle would yield a considerably smaller angle (43.7°), but to mimic the work of Manabe and Strickler the insolation-weighted angle has not been used.

In the work of Manabe and Strickler (1964) an albedo of 0.102 was used for both shortwave and longwave radiation, this value has been used for the radiative equilibrium simulations of this thesis as well. This results in an emissivity of 0.898 for both shortwave and longwave radiation.

Table 3.2: Radiative Equilibrium: Solar Input

Variable	Symbol	Value
Latitude	ϕ	35°N
Day Number	N	115
Zenith Angle	θ_s	60°
Effective Solar Constant	SW_0^*	$697W/m^2$

As explained in chapter 2.5 simulations with the RRTMG radiative code require specification of an additional domain on top of the LES domain, with a certain temperature and composition. In the current implementation of the RRTMG code in DALES it is not possible to use perform simulations without a "backrad" domain or with a "backrad" domain of 0 layers.

A "backrad" domain with the same latitude and time as Manabe and Strickler (1964) was not available, therefore the "backrad" domain from CGILS S6 has been used, corresponding to a day in mid-July at 17°N[1].

Initially it was not possible to user-specify the ozone profile correctly inside the LES domain; only a constant ozone mixing ratio could be used. Therefore the default ozone profiles of RRTMG have been used, these profiles correspond to a mid-latitude location in summer (Mlawer et al., 1997). This ozone profile can be observed in appendix D.2. The modification to enable user-specification of the ozone profile has been made as well, but has not been used for these simulations, the code for this modification can be found in chapter B.3 of the appendix.

As these simulations are performed on a minimal horizontal grid size without motions and the radiative code is started only once every hour in simulated time, these simulations are computationally very fast. Simulation speeds of 10000 simulated hours per wall-clock hour can be reached using only a single processor. As these simulations are very cheap they have been performed for 300 simulated days to ensure a completely converged simulation in radiative equilibrium.

As the radiative equilibrium simulations do not include evaporation and transport of water, the specification of the initial water distribution profile is important as this distribution directly affects the resulting equilibrium state. The distribution of water in the atmosphere has been derived from the Manabe and Strickler paper and can be observed in 3.1.

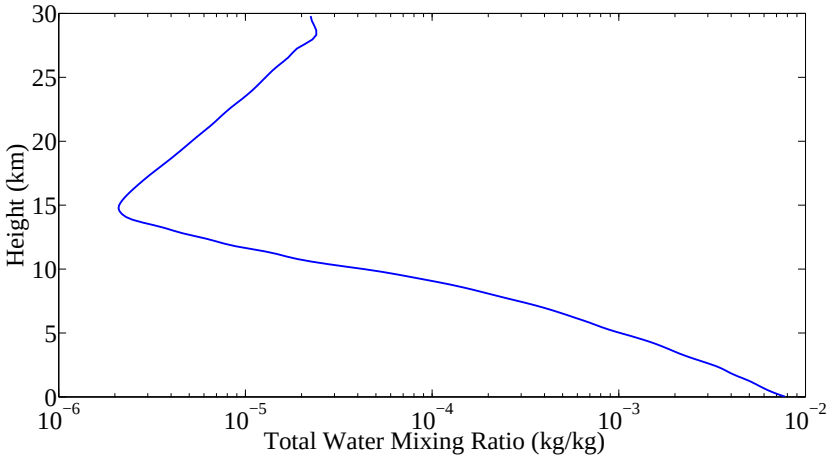

Figure 3.1: Total water mixing ratio as derived from Manabe and Strickler (1964). In the radiative equilibrium simulations the water mixing ratio is not determined by the model and has to be provided. This water mixing ratio profile is used as input in these calculations. As clouds and precipitation are absent in these simulations all water is in a gaseous phase.

[1] The input conditions for CGILS S6 can be found on http://atmgcm.msrc.sunysb.edu/cfmip_figs/Case_specification.html

Chapter 4

Setup of Radiative-Convective Equilibrium Simulations

To simulate radiative-convective equilibrium some small modifications were made to the original DALES code. These modifications include changes to the advection scheme, implementation of ice clouds in the radiation scheme and small adjustments of the gravity wave damping. In the first section these modifications will be discussed. Afterwards the setup of the domain and the used input conditions are explained.

4.1 Modifications

4.1.1 Ice Clouds

For this project domains of up to 30 kilometers high have been simulated. During these simulations clouds emerged at a height of 10 to 12 kilometers. Clouds at these heights are generally cirrus or cirrostratus clouds. The temperatures inside these clouds are well below freezing temperature and hence these clouds are largely composed of ice crystals.

The DALES version used in these simulations has previously been used to perform simulations to investigate stratocumulus clouds (van der Dussen et al., 2013). Stratocumulus clouds are generally located in lower parts of the troposphere, below 2500 meters. Being close to the surface these clouds are much warmer and therefore they can be modeled as being composed entirely of liquid droplets. The composition of clouds can have a profound effect on the optical properties of the clouds such as absorption and scattering. Two important properties are the cloud water content and the effective radius. The cloud liquid water path $CLWP$ is calculated according to formula 4.1 with the effective radius $r_{eff-liq}$ being calculated with formula 4.2. This liquid effective radius is the result of assuming a lognormal distribution of droplet size (van der Dussen et al., 2013). In this formula N_c is the average droplet number concentration, σ_g is the geometric standard deviation 1.34,

$$CLWP = \int_{z_{base}}^{z_{top}} \rho_{air} q_l dh, \tag{4.1}$$

$$r_{eff-liq} = \left(\frac{3\rho_{air} q_l}{4\pi \rho_l N_c} \right) \exp\left[\ln\left(\sigma_g\right)^2 \right]. \tag{4.2}$$

Simulations using this original code resulted in large radiative tendencies in the cirrus clouds resulting in extreme temperatures differences. The radiative tendencies at the top of the cloud cause very strong cooling, whereas the tendencies at the cloud base caused very strong heating. The resulting temperature differences caused even stronger cooling and heating, causing DALES to crash.

Optical properties of ice crystals and water droplets in clouds can differ substantially since cloud liquid droplets are smaller than cloud ice crystals. Moreover, the shape of ice crystals is mostly hexagonal whereas liquid droplets are generally round. Assuming the cirrus clouds to be composed entirely of liquid thus overestimates the optical effects of these clouds.

The RRTMG code has been used extensively and has been validated frequently, therefore it can be safely assumed that the optical properties of RRTMG for ice crystals are functioning properly and that RRTMG is well able to cope with mixed ice-liquid clouds. For simulations with ice and liquid clouds RRTMG requires information on four input parameters; the effective radius of liquid droplets $r_{eff-liq}$, the effective radius of ice crystal $r_{eff-ice}$, the cloud liquid water path $CLWP$ and the cloud ice water path $CIWP$.

DALES does not calculate the ice content directly. Instead an ice-liquid partitioning is calculated using the microphysics scheme of Böing (2014). This is a single-moment scheme based on the work of Grabowski, which uses tabulated values to calculate the ice as a function if the absolute temperature. By multiplying the prognostic liquid water mixing ratio q_l with this partitioning the amount of ice cloud water (q_I) and liquid cloud water (q_L) can be calculated which can be used to calculate the cloud liquid water path and cloud ice water path,

$$CIWP = \int_{z_{base}}^{z_{top}} \rho_{air} q_I dh, \tag{4.3}$$

$$CLWP = \int_{z_{base}}^{z_{top}} \rho_{air} q_L dh. \tag{4.4}$$

The effective radius of the ice crystals is calculated using the diagnostic formula 4.5 from Ou and Liou (1995) based on data from Heymsfield and Platt (1984). In this formula $r_{eff-ice}$ is the effective radius of the ice crystals in micrometers and T is the absolute temperature. This formula is only valid within a certain temperature range, hence models like the ECMWF and RACMO2 have limited the effective radii of the ice crystals between 30 and 60 micrometers (ECMWF, 2013; van Zadelhoff et al., 2007). After calculation of the effective ice radius, the ice radii larger than $60\mu m$ are rounded down to $60\mu m$, whereas ice radii smaller than $30\mu m$ are rounded up to $30\mu m$,

$$r_{eff-ice} = 326.3 + 12.42\,(T - 273.15) + 0.197\,(T - 273.15)^2 + 0.0012\,(T - 273.15)^3\,. \tag{4.5}$$

Validated optical properties of ice crystals were already included in the RRTMG radiative code but were not used in previous DALES simulations. RRTMG uses the optical properties of ice crystals from Ebert and Curry, which have been researched specifically for cirrus clouds in climate models (Ebert and Curry, 1992). The implemented code to enable using these optical properties can be found in appendix B.1.

The effects of the implementation of this code in DALES has been tested using several short simulations. To test this a layer of clouds between 11 and 13 kilometers was simulated. The cloud water path was varied to create clouds with different cloud water contents as calculated using equation 4.6, a modified version of equation 4.1. In this equation the ice water specific humidity is represented by q_I and the liquid water specific humidity is q_L, which is not the same as the prognostic variable q_l, because of the ice-liquid partitioning,

$$CWP = \int_{z_{base}}^{z_{top}} \rho_{air}\,(q_L + q_I)\,dh. \tag{4.6}$$

Three different series of simulations were simulated. In the first series (blue) the clouds were entirely composed of liquid water, in the second series (black) the clouds were composed of equal parts of liquid water and ice and in the third series (red) the clouds were composed entirely of ice. The effect on the reflectivity, measured using the albedo was determined, which also includes reflective effects of the surface and trace gasses in the atmosphere. As can be seen from figure 4.1 the optical effects of ice clouds are substantially smaller than the optical effects of water clouds. The optical properties of mixed ice-liquid clouds are close to the properties of liquid-clouds.

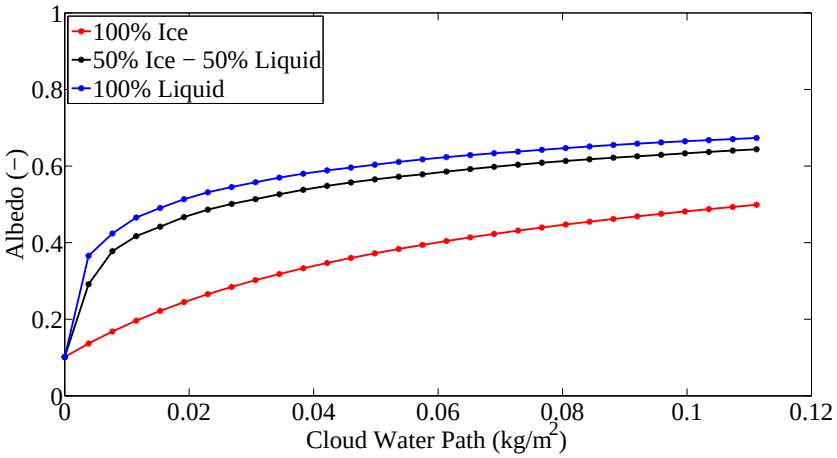

Figure 4.1: Difference in optical effects of ice and liquid clouds. In this simulation clouds of various cloud water paths were simulated for different ice-liquid ratios. The effect on the reflectivity was measured using the total atmospheric albedo.

Addition of the ice clouds thus improves the modeling of the effects of clouds on the radiation. The effective radius of precipitating ice and water is relatively large compared to the ice and water particles in clouds. Because of their large effective size, the optical properties of precipitation can be neglected.

4.1.2 Advection Scheme Modification

The advection in the performed simulation is calculated using a hybrid advection scheme similar to the scheme proposed by Hill and Pullin (2004). This scheme calculates the advection in the x, y and z-direction separately using a fifth order advection scheme, except on locations where discontinuities in the advected quantities arise. Discontinuities are detected by comparing a smoothness parameter λ to a critical value.

At locations with discontinuities a fifth order Weighted Essentially Non-Oscillatory (WENO) scheme is used as developed by Blossey and Durran (2008). This scheme filters out some of the higher frequency components of the solution, thus preserving the discontinuity while filtering out unwanted oscillations. At discontinuities higher order numerical schemes can result in oscillatory behavior. This oscillatory behavior can result in prohibited values of the advected quantities in the numerical simulation, such as negative humidities. More extensive descriptions of the WENO advection schemes can be found in the paper by Blossey and Durran (2008).

To determine whether a location contains discontinuities the smoothness parameter λ is calculated. If this smoothness parameter is larger than a critical value the WENO scheme is utilized, else the ordinary fifth order advection scheme is used. The critical value of λ is set to 20 following van der Dussen (2015). This smoothness parameter is calculated using a set of points near the point of interest. Which points are used depends on the direction of the advection velocity as defined in formula 4.7. Using these points λ at point $i + 1/2$ is calculated using formula 4.8,

$$K = \begin{cases} [i-1, i, i+1], & \text{if } u_{i+1/2} \geq 0, \\ [i, i+1, i+2], & \text{otherwise,} \end{cases} \tag{4.7}$$

$$\lambda_{i+1/2} = \frac{\max_{k \in K} \gamma_k}{\min_{k \in K} \gamma_k + \epsilon}. \tag{4.8}$$

In formula 4.8 the symbol ϵ is a small number depending on the variation η in the advected field. Usually constant values are taken for the value of η of each advected field,

$$\epsilon_{old} = \eta^2 \times 10^{-8}. \tag{4.9}$$

While these values work fine for simulations in the lower atmosphere, for simulations in higher domains the used values of the variation η are too high, therefore ϵ is no longer a small value. Hence the resulting smoothness parameters are too low compared to the critical value and use of the WENO scheme is not triggered as should. As suggested by Peter Blossey (personal communication, March 12, 2015), ϵ should be calculated using formulas 4.10 and 4.11 to make it dependent on the local variation in the advected field,

$$\epsilon_{new} = 10^{-300} + \sum_{k \in K} \gamma_k \times 10^{-14}, \tag{4.10}$$

$$\gamma_i = (\phi_{i+1} - \phi_i)^2 + (\phi_i - \phi_{i-1})^2. \tag{4.11}$$

This should result in better calculations for the smoothness parameters and hence more appropriate use of the WENO scheme. Using this method problems with oscillatory behavior should be reduced. The implemented code can be found in appendix B.2.

Another problem of the oscillatory behavior is the possibility of the advection scheme creating negative total water specific humidities. This is not only nonphysical but can result in trouble with the radiative code. To avert this the total water specific humidity should be more than a small fraction of the input profile.

4.1.3 Gravity Wave Damping

In LES a smooth transition at the top of the LES domain is usually required. Variables at the top should hence be approximately smooth. Moreover, gravity waves can be reflected at the top of the domain and can result in buildup of momentum. To reduce this gravity wave damping is implemented. Gravity wave damping damps out variations in prognostic variables such as velocities, water mixing ratio and potential temperature in the so called sponge layer. This sponge layer takes approximately one quarter of the vertical grid points at the top of the domain and acts as some sort of stability buffer. Because of the damping the results inside the sponge layer are generally less reliable. It is therefore important to position the sponge layer above the part of the domain where the clouds occur.

In these simulations the top of the LES domain is located in the stratosphere. The stratosphere is included for stability purposes and for the effects on radiation. This project is not interested in the dynamics of the stratosphere and it is unsure whether DALES is able to correctly calculate the stratospheric dynamics. Vertical velocities in the stratosphere for example should be small because of the strong stratification.

Gravity wave damping has been used to reduce the variations in fields and to damp the dynamics. Water content and temperature are all damped towards the slab averaged value in an effort to create uniform slabs. Vertical velocities are damped towards a zero velocity, reducing the exchange between the layers in the stratosphere. Horizontal velocities are damped towards their geostrophic values, as damping towards the slab average horizontal velocity values resulted in continuously increasing horizontal velocities.

The most likely explanation for the increasing horizontal velocities is the possibilities of clouds to overshoot the tropopause and enter the stratosphere. Here they evaporate or descend, but the horizontal momentum they carry is not entirely removed in this process and hence horizontal momentum is transported to the stratosphere. Since the amount of friction in the stratosphere is negligible there are virtually no damping forces acting on the velocities. The only force influencing the momentum is the Coriolis force, which merely changes the direction of the velocity field, but does not change the magnitude of the velocity. Therefore the direction of the velocity starts rotating while increasing continuously in time. This produces the risk of creating huge velocities in the stratosphere. By damping the velocity towards the geostrophic velocity this risk is avoided.

The strength of the damping in DALES is a function of height; slabs higher in the sponge layer experience stronger damping. The original amount of damping however was not sufficient to reduce the variations, therefore the damping has increased by a factor of 10 to ensure zero heat and moisture fluxes at the top of the domain.

4.2 Domain Setup

In radiative-convective equilibrium the simulation includes both radiation as well as convection. Moreover, clouds are included in the simulations. As cloud systems can span several kilometers a large domain is needed to enable simulations of multiple cloud systems. Moreover, larger domains enable better development of the turbulent motion. In small domains the largest scales of motions are limited by the domain size.

Radiative-convective equilibrium however is quite a slow process and simulations with radiation, microphysics, turbulence and advection are computationally quite expensive. Therefore a different approach has been used. First simulations on a small domain of 24 by 24 kilometers have been performed. Although this domain size is too small to allow good development of cloud structures and large scale dynamics, this domain is computationally relatively cheap. It is hence possible to perform long simulations of several tens of days on this domain. Experiments on this domain are simulated until they are in approximate equilibrium. Even though the modified WENO scheme is used oscillatory behavior is still observed at the top of the troposphere.

The results are therefore smoothed in Matlab using the *smooth* function to remove oscillations and other irregularities[1]. These smoothed profiles are used as input profiles for simulations on a larger domain. Using this approach the initial conditions of the large scale domain simulations are already close to equilibrium, reducing spin-up time and hence saving computation time. The large scale dynamics that can evolve on a larger domain could still change this equilibrium state however. The large domain measures 72 by 72 kilometers horizontally and is hence 9 times larger. Several cloud systems can in principle develop on this domain size. Both domains use the same horizontal spacing of 250 meters. This grid is used for the final 10-day simulations.

Both simulations use the same vertical grid. This is a non-equidistant grid of 158 points. At the bottom the vertical spacing is 40 meters similar to the well-known BOMEX case. This spacing should suffice to create turbulence near the surface. A vertical grid spacing of 40 meters on a domain of 30 kilometers would require 750 grid levels, which is computationally very expensive. The grid is hence stretched by 2.5% until the grid has a vertical spacing of 200 meters. A vertical spacing of 200 meters should suffice to simulate appropriate cloud dynamics. Therefore the vertical spacing remains 200 meters until a height of 12 kilometers is reached, above which no clouds are formed. Hence the grid above 12 kilometers can have a higher vertical spacing, therefore the grid stretches by 1% until a height of approximately 30 kilometers. Higher stretch factors have been used but resulted in non-zero fluxes at the top of the domain. A plot of the vertical grid spacing versus height can be found in appendix D.1.

Table 4.1: Radiative-Convective Equilibrium: Domain

Variable	Value	
	Small Domain	Large Domain
Horizontal Grid Points	96×96	288×288
Horizontal Domain Size	$24km \times 24km$	$72km \times 72km$
Vertical Grid Points	158	158
Vertical Domain Size	30km	30km

4.3 Settings and Input

Simulations of radiative-convective equilibrium have been executed using radiation input files from CGILS S6. The CGILS simulations used data from the GEWEX cloud system study (GCSS)(Blossey et al., 2013). The S6 input as used in these simulations are from mid-July at 17°N, 149°W, which is situated in the middle of the Pacific Ocean, near Hawaii. Using this latitude and day number the insolation-averaged zenith angle and effective solar constant were calculated using equations 2.18 and 2.20. The results can be found in table 4.2.

[1]The smooth function is a moving-average filter in Matlab, more information can be found on http://nl.mathworks.com/help/curvefit/smooth.html

As diurnal variations are removed and the solar input is set manually, the time of day and longitude are not relevant. The resulting solar constant and zenith angle are not equal to the ones used in CGILS S6 ($448.1 W/m^2$ and 51.0°)[2] as CGILS uses daytime averaged values of these variables, although it is suggested in the paper by Blossey et al. (2013) that using an insolation-weighted zenith angle would be more accurate. The default albedo of 0.05 and emissivity of 0.95 are used in these simulations.

Table 4.2: Radiative-Convective Equilibrium: Solar Input

Variable	Symbol	Value
Latitude	ϕ	17°N
Day Number	N	196
Zenith Angle	θ_s	38.7°
Effective Solar Constant	SW_0^*	$571 W/m^2$

The radiative transfer is calculated using the RRTMG radiative code as described in chapter 2.5. The radiative code is started every 10 minutes in simulated time to save computation costs. Further increasing this timescale could result in ghost clouds. Ghost clouds occur when the position of the clouds is changing, as the radiative code is updated less frequently than the dynamics of the LES model. If the clouds are moving the radiative tendencies of the clouds are no longer acting on the location where the cloud is, but rather at the location where the cloud was located. Running the radiative transfer code more frequently reduces this problem.

The simulations are performed above a surface with a uniform constant sea surface temperature (SST). The resulting heat and moisture fluxes at the surface are calculated by the model. Sea surface temperatures range from 22°C to 28°C with steps of 2°C. These values are commonly observed at this latitude and time of year (NOAA, 2015). These temperatures are converted to liquid potential surface temperatures in Kelvin using equation 2.2.

As these simulations are performed on domains of 30 kilometers height it can no longer be assumed that the density does not vary in the vertical direction. Therefore a height dependent density profile has been used. This height dependent density is used in the anelastic approximation for the vertical advection. The density profile is calculated by the model using the standard atmospheric lapse rate without a surface temperature offset.

The advection scheme is a fifth-order hybrid scheme. This scheme calculates the advection using a fifth-order stencil. At discontinuities the Weighted Essentially Non Oscillatory (WENO) scheme is used. More information can be found in chapter 4.1.2.

These simulations are performed with microphysics as to have a mechanism to remove moisture from the atmosphere. Simulations without microphysics would eventually run into problems as the air would become too humid. As clouds can occur at both high and low altitudes and therefore at high and low temperatures, a microphysics scheme is needed that incorporates ice. The *simpleice* microphysics scheme from Böing (2014) includes ice microphysics and is applicable in situations of deep-convection. This single-moment ice microphysics scheme is based on the work of Grabowski with several modifications. The ice-liquid partitioning in clouds of this microphysics is also used in the radiative code for the ice-liquid partitioning. The settings and their corresponding flags and values in the namoptions files are described in table 4.3.

Table 4.3: Radiative-Convective Equilibrium: Settings

Module	Namoptions	Value	Description
Radiation	iradiation	4	RRTMG radiative transfer code
Surface	isurf	2	Fixed surface temperature; fluxes are calculated
Density	ibas_prf	3	Density profile with standard atmospheric lapse rate
Advection	iadv	55	Hybrid advection scheme; fifth order and WENO
Microphysics	imicro	5	Single-moment ice microphysics; ice and water precipitation

For the other settings of the simulations the reader is referred to the appendix D.3 where the complete namoptions file used in these simulations can be found.

[2]The input conditions of CGILS can be found on http://atmgcm.msrc.sunysb.edu/cfmip_figs/Case_specification.html

4.3.1 Input Profiles

Using the settings as described in the previous section requires specification of four input files. The radiation is prescribed in the *backrad.inp* NC-file. Similar to the radiative equilibrium simulations the CGILS S6 backrad file has been used combined with the default RRTMG ozone profiles.

These simulations do not make use of subsidence or large scale temperature and humidity tendencies. Near the equator the vertical velocity is generally positive whereas it is negative at the horse latitudes (30°N and 30°S). As these simulations are idealized situations no observations can be used to determine the appropriate vertical subsidence velocities. To simplify the problem subsidence velocities have therefore been set to zero. Similar arguments apply to large scale temperature and humidity tendencies. The *lscale.inp* file therefore only contains the geostrophic velocities u_g (West-East) and v_g (South-North). These velocities are both set to constant values of $0.01m/s$ and $5.0m/s$ respectively. Velocities in the stratosphere are generally much higher and usually some wind shear is present in the troposphere as well. These profiles are not entirely realistic, but as the focus of this thesis is not on the velocities these simplified pressure forcing profiles can be used to reduce the complexity of the problem.

The initial profiles are described in the *prof.inp* file which contains the liquid potential temperature θ_l, the total water specific humidity q_t, horizontal velocities u and v and the turbulent kinetic energy e as a function of the height. The winds u and v are set equal to their geostrophic counterparts. Aside from this the microphysics requires specification of a *scalar.inp* file which contains the initial rainwater specific humidity q_r and rain droplet number concentration N_r. Although the simpleice microphysics scheme does not use the droplet number concentration N_r, the bulk microphysics scheme does use this variable. The variables q_r and N_r are determined by the model in a few time steps and hence the input of these variables is less important.

As these experiments are equilibrium experiments the simulations should converge towards the same end-result regardless of the initial conditions, therefore specification of the input profiles should not matter. To reduce spin-up time results from smaller domains are used as input profiles. These input profiles are the results of many iterations with the same settings as the simulations on the larger domains. Specification of total water specific humidity q_t and liquid potential temperature θ_l is quite important, as convergence of these variables in DALES can take a lot of time. These profiles can be found in figure 4.2. These small domain simulations have been performed until the relevant variables converged. These simulations took between 23 and 35 simulated days. Relevant variables consist of atmospheric water content, cloud water, potential temperature and surface fluxes. This resulted in the input profiles of figure 4.2.

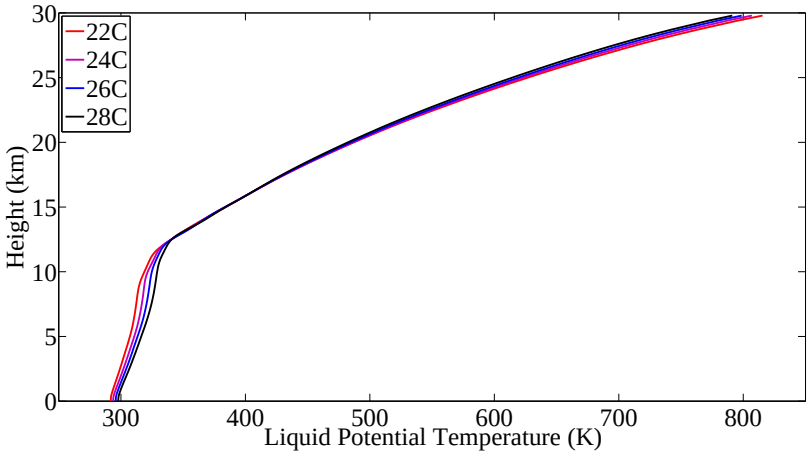

(a)

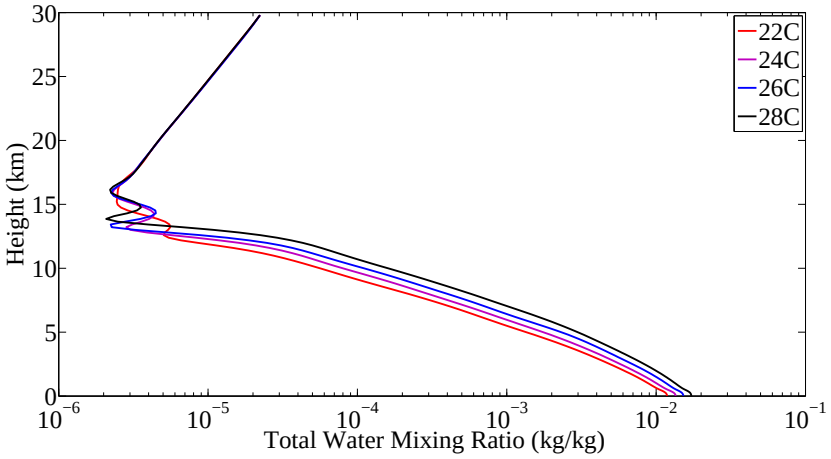

(b)

Figure 4.2: Input profiles for various SSTs. Simulations on a 24 by 24 kilometer domain with uniform sea surface temperatures ranging from 22°C to 28°C have been performed. These graphs are the steady state results of these simulations. The liquid potential temperature and total water specific humidity profiles have been smoothed in Matlab to reduce oscillations and other irregularities. These profiles serve as input for the simulations on larger domains.

Chapter 5

Radiative Equilibrium Results

To test the implementation of the RRTMG transfer this thesis investigates the situation in radiative equilibrium. This work is largely inspired by the work of Manabe and Strickler (1964). Three sets of experiments have been carried out. In the first sets the net radiative flux has been determined as a function of the prescribed surface temperature to determine the surface temperature in radiative equilibrium.

In the second sets of experiments, radiative equilibrium is calculated in atmospheres without certain gaseous components such as ozone or water, similar to the work of Manabe and Strickler.

Additionally, the third sets of experiments is used to determine the sensitivity of the equilibrium to changes in the atmospheric composition, the column amounts of three gaseous components are changed and the resulting temperature profiles are investigated.

5.1 Radiative Equilibrium

In chapter 3 it was mentioned that in absence of motions of air, DALES converges towards situations in which there is no net radiative heating, a situation called thermal equilibrium. In this situation the net radiative flux is constant with altitude, but the net radiative flux can be nonzero. Radiative equilibrium however is a special case of thermal equilibrium in which the solar radiation entering at the top of the domain is equal to the sum of the thermal radiation and reflected solar radiation leaving the domain. In other words, the net radiative flux is zero at every altitude.

DALES will automatically converge towards a situation with a divergence free radiative flux. To force DALES to reach radiative equilibrium the surface temperature has been made a function of the amount of incoming radiation. By changing the surface temperature the longwave emission of the ground surface is adjusted as to always force a zero radiative flux at the surface. Hence the simulation will converge towards a situation with zero net radiative flux at every altitude. In this section the experiment used to test this modification is described.

Using the settings of chapter 3.3, which includes water vapor and the RRTMG ozone profile, 16 simulations of 300 days have been carried out. These simulations are without motions of air. In these 16 simulations the surface potential temperature has been fixed at a temperature between 275K and 350K. After 300 simulated days the net radiative flux difference between top of the atmosphere and ground surface was less than $0.06 W/m^2$ and hence the net radiative flux was essentially divergence free.

The net radiative flux at the top of the atmosphere has been determined and has been plotted as a function of surface potential temperature in figure 5.1 by the blue asterisks. These simulations have been compared to a simulation in which the surface temperature was a function of the incoming radiation, as to reach radiative equilibrium, indicated by a red diamond.

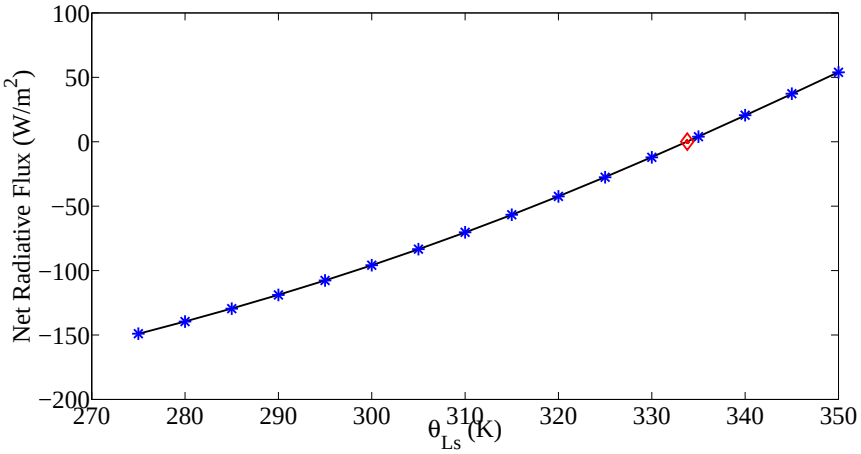

Figure 5.1: Net radiative flux as a function of the surface potential temperature. A fourth-order polynomial fit (black line) has been fitted to the results of the simulations (blue asterisks). This fit has been used to determine the surface potential temperature at zero net flux. The resulting value is $333.75K \pm 0.06K$. This result is in agreement with the calculated value of the surface potential temperature of the modified DALES version ($333.80K$) indicated by the red diamond.

A fourth-order polynomial fit has been used to determine the net flux as a function of the surface potential temperature. This fit function indicates that the surface potential temperature should be $333.75K \pm 0.06K$ at a zero net radiative flux. This temperature is in good agreement with the surface potential temperature of $333.80K$ of the radiative equilibrium DALES version. This indicates that the modification to reach radiative equilibrium functions properly.

The absolute temperature of the surface is $335.22K$, which is higher than the highest observed temperature values on earth and therefore unrealistic. The surface temperature however is close to the calculated value of Manabe and Strickler of $332.3K$.

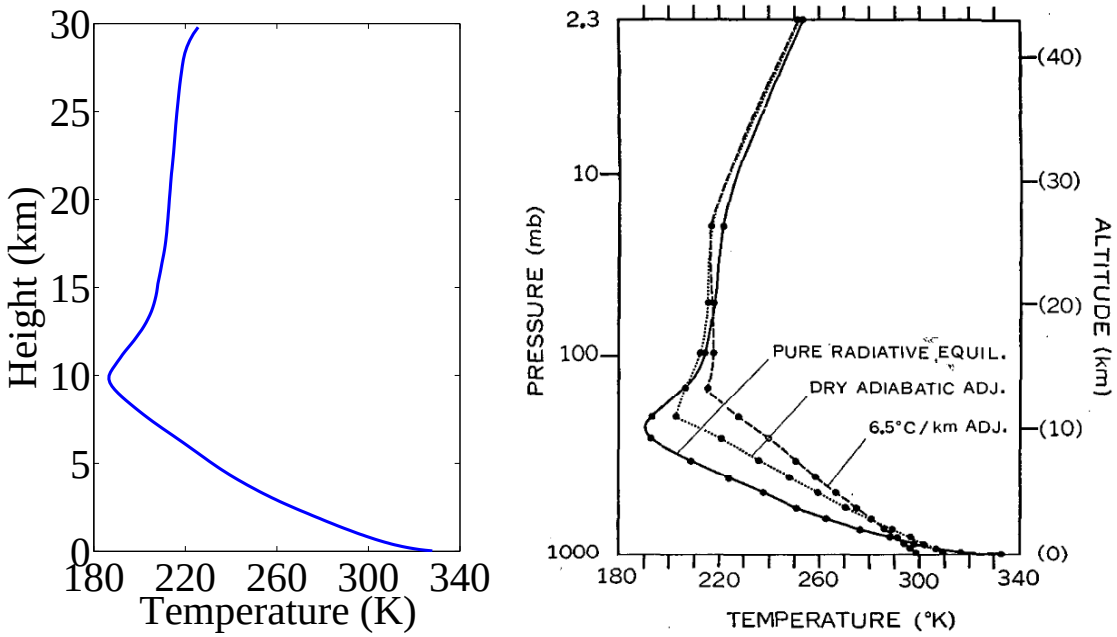

(a) DALES Results

(b) Manabe and Strickler (1964) Results

Figure 5.2: Temperature profile in (pure) radiative equilibrium. Using the water vapor mixing ratio from Manabe and Strickler (see chapter 3.3), the RRTMG ozone profile and insolation input similar to the work of Manabe and Strickler the temperature in radiative equilibrium has been determined in subfigure a. Forcing radiative equilibrium results in an absolute surface temperature of $335.22K$. At approximately 10 kilometers the tropopause inversion is formed, similar to to the calculations of Manabe and Strickler (1964) in subfigure b. Image source: figure 4, Manabe and Strickler (1964).

The absolute temperature of the surface ($335.2K$) in radiative equilibrium is much higher than values observed at earth. The temperature in the middle and upper tropopause is much colder than commonly observed. The resulting tropospheric lapse rate is $14.5K/km$ which is considerably higher than the dry ($9.8K/km$) and saturated adiabatic lapse rate ($4K/km$ - $7K/km$). This steep lapse rate indicates that the simulation has an absolutely unstable troposphere. Radiation therefore destabilizes the troposphere, a process that normally results in buoyancy-driven convection. The behavior of the virtual potential temperature in figure 5.3 confirms that the situation is unstable.

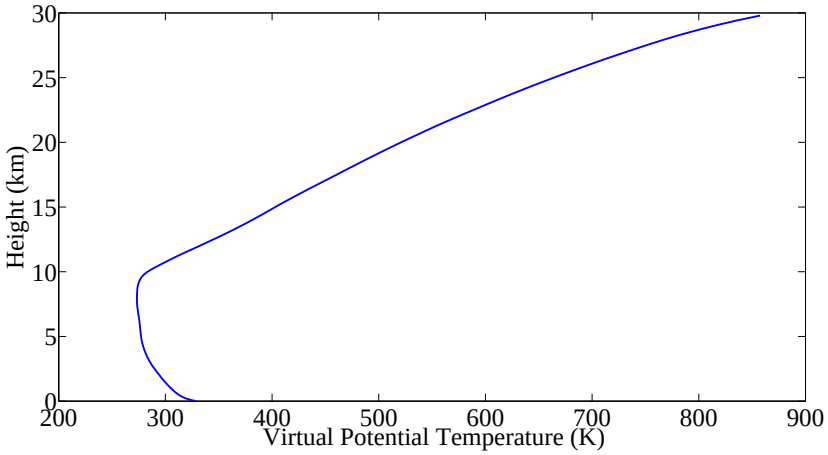

Figure 5.3: The virtual potential temperature profile in radiative equilibrium as a function of the height. The lapse rate below 8 kilometers is negative indicating absolutely unstable situations. Air parcels at the surface have a virtual potential temperature equal to the atmosphere at 12 kilometers, these parcels can hence rise up to 12 kilometers directly. In case of overshoots these air parcels can reach even higher altitudes.

The virtual potential temperature decreases with height below 8 kilometers and the virtual potential temperature of the surface is approximately equal to the virtual potential temperature at 12 kilometers. Air can hence easily rise up to 12 kilometers. In case of overshoots air parcels can rise up even higher. These results confirm the notion that radiation destabilizes the atmosphere.

5.2 Effect of Atmospheric Composition

Manabe and Strickler investigated the effects of the atmospheric composition on the temperature in radiative equilibrium. The atmosphere in their calculations consisted of three absorbing gasses; water (H_2O), carbon dioxide (CO_2) and ozone (O_3). In their calculations they removed some of these key species resulting in the temperature profiles as displayed in figure 5.4.

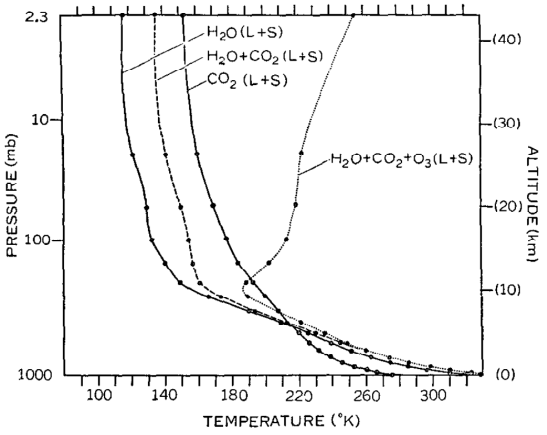

Figure 5.4: Manabe and Strickler (1964): Effect of atmospheric composition. In these simulations the effects of adding and removing three gasses of the atmosphere in radiative equilibrium have been investigated. These three gasses (CO_2, O_3 and H_2O) are good absorbers of longwave or shortwave radiation. Image source: figure 6a, Manabe and Strickler (1964).

Their results show that in absence of ozone no temperature inversion in the tropopause is formed. A

similar approach has been used in this thesis. It should be noted that the atmosphere in the simulations of this thesis also contains additional trace gasses and optically less active gasses as these are by default included in the RRTMG code. In figure 5.5 the results of simulations in radiative equilibrium with CO_2 only (black), H_2O and CO_2 (blue) and all three gasses (red) have been plotted. The dashed simulations use the CGILS backrad file, whereas the solid line simulations use backrad files which closely resemble the results from Manabe and Strickler (1964).

Initial simulations (dashed lines) used the CGILS backrad file, however at higher altitudes these results deviate substantially at from the results of Manabe and Strickler in figure 5.4. Therefore three backrad files have been created for the solid line simulations using the results of Manabe. In these three backrad files the temperature, water vapor and ozone profiles from the curves in figure 5.4 have been used. The results in DALES are very similar to the results of Manabe and Strickler.

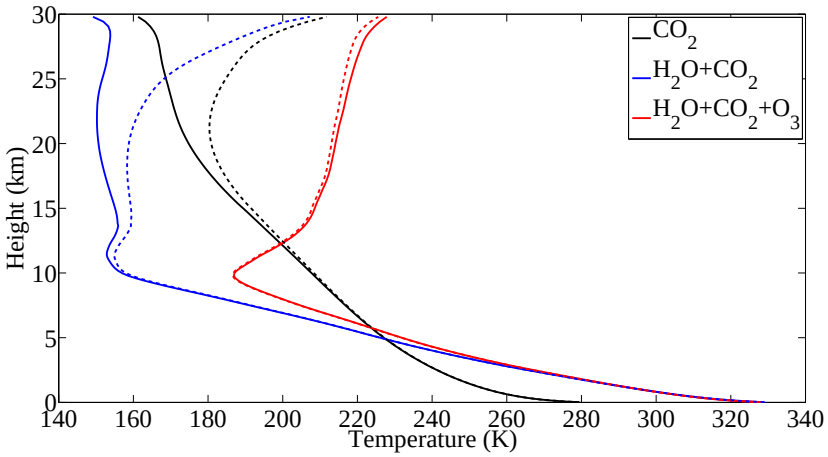

Figure 5.5: Effect of atmospheric composition on temperature profiles in radiative equilibrium. Three different atmopheric compositions have been used; CO_2 only (black), H_2O and CO_2 (blue) and all three gasses (red).

These simulations revealed an important pitfall of using the RRTMG radiative transfer code. As observed in figure 5.5 the results of the simulations, especially at higher altitudes, are strongly depending on the used backrad file. Using the CGILS backrad file produced the dashed lines, which deviate substantially for the CO_2 only (black) and H_2O and CO_2 (blue) cases. Using the results from Manabe and Strickler to produce backrad files with temperature profiles corresponding to their experiments produced temperature profiles that closely resembled the results from their classic paper. Users of DALES should therefore be aware of the influence of the choice of backrad files.

Note that the solid lines show small deviations in the temperature profile at the top of the LES domain; the lapse rate at the top 1 km of the atmosphere deviates from the behavior in the underlying layer. This is most likely an effect of the radiative transfer code and the backrad domain. As one is usually not interested in the results at the top of the LES domain, this behavior has not been further investigated.

These results (blue lines) show that water vapor increases the temperature in the lower troposphere substantially, which is in agreement with the fact that water is a greenhouse gas. As water is a good longwave absorber, it absorbs a large part of the longwave radiation emanating from the surface. Part of this radiation is re-emitted to the surface again, which causes positive feedback, increasing the surface temperature. Compared to the atmosphere without water (black) the temperature in the higher layers of the atmosphere is colder. Because the lower troposphere is much warmer, more longwave radiation is emitted upward. To ensure the zero net radiative flux as required in radiative equilibrium, the higher layers of the atmosphere should emit less longwave radiation, which requires them to be colder.

Addition of ozone (red) creates a tropopause inversion and a rising temperature in the stratosphere. This is in agreement with the results from Manabe and Strickler. Ozone is a strong absorber of ultraviolet radiation, part of the shortwave radiation. Absorption of shortwave radiation increases the temperature of the air. As the ozone mixing ratio increases with height (see figure D.2), the shortwave heating of

ozone increases as well. Therefore the temperature in the stratosphere is increasing with altitude.

5.3 Effects of Gas Concentrations

The previous section showed that water, carbon dioxide and ozone play key roles in determining the temperature profile of the atmosphere in radiative equilibrium. In the simulations of the previous sections fixed profiles of gas concentrations from either Manabe and Strickler (1964) or RRTMG were used. Research however has shown that these concentrations show seasonal and latitudinal variations (Salby, 1996; Taylor, 2005). Research has also shown that the concentration of carbon dioxide, a greenhouse gas is increasing over time. Ozone concentrations have also declined in the past decades, creating the well-known ozone hole. Based upon his previous study Manabe researched the effect of changing the gas concentrations on the radiative-convective equilibrium (Manabe and Wetherald, 1967). In this paper Manabe and Wetherald changed the concentrations and profiles of three important atmospheric gasses; water, carbon dioxide and ozone. In this thesis a similar approach is used for radiative equilibrium simulations. In these simulations one gas concentration is varied, while the other gas concentrations are kept at the same values as in the previous section. All of the experiments of this section use the same CGILS S6 backrad file to be internally consistent.

First the amount of carbon dioxide was varied. The carbon dioxide concentration in RRTMG is constant with height. Carbon dioxide has a constant volume mixing ratio of 355 ppmv, which results in a total of $5.5 kg/m^2$ of carbon dioxide in the atmosphere. In 12 simulations the volume mixing ratio has been varied between 0 ppmv and 781 ppmv. The water vapor and ozone profiles were kept at the same values. The insolation input was the same as in the previous simulations, a 60° zenith angle and a $697 W/m^2$ solar constant.

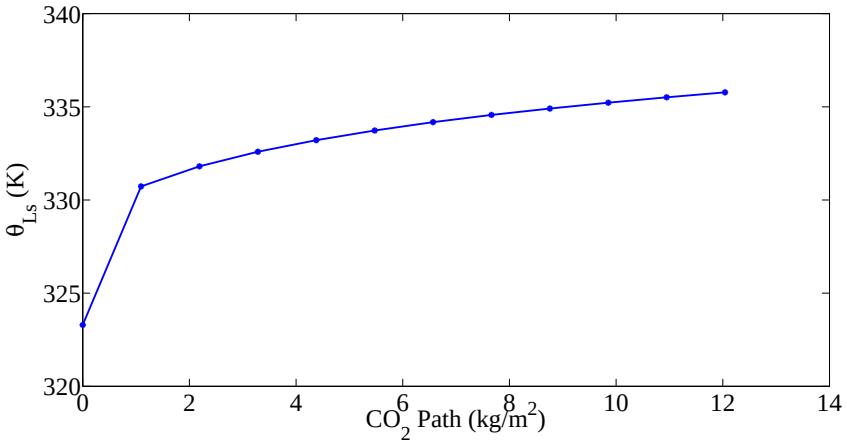

Figure 5.6: Effect of carbon dioxide concentrations on the surface potential temperature. A constant volume mixing ratio with height is used to determine the effect of changing the carbon dioxide concentration. Increasing the amount of carbon dioxide increases the temperature. The standard (RRTMG) carbon dioxide column amount is $5.47 kg/m^2$. Doubling this amount of carbon dioxide increases the potential temperature by $1.8 K$.

These results show that carbon dioxide increases the temperature of the surface, which is consistent with the idea that carbon dioxide is a greenhouse gas. The temperature of the rest of the atmosphere has been determined as well, in figure 5.7 the temperature profile for four carbon dioxide concentrations can be found. The effects on the tropospheric temperature is small, but the temperature in the stratosphere decreases substantially. Several researchers have researched the effect of carbon dioxide on the radiative-convective equilibrium (Manabe and Wetherald, 1967; Romps, 2011). Their results showed that the stratospheric temperature in RCE decreased with carbon dioxide concentration. As the stratosphere is dominated by radiative processes the radiative equilibrium simulation will likely show similar behavior.

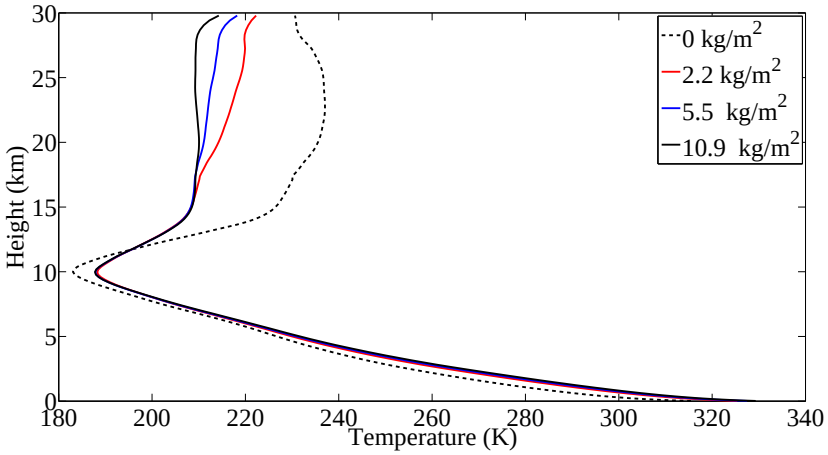

Figure 5.7: Effect of carbon dioxide concentrations on the temperature profile in radiative equilibrium. The standard RRTMG amount of carbon dioxide is $5.5kg/m^2$ (355 ppmv). Addition of carbon dioxide changes the temperature profile substantially. Increasing the amount of carbon dioxide has little effect on the temperature in the lower troposphere. The temperature in the stratosphere decreases with amount of carbon dioxide which is consistent with the RCE results of Manabe and Wetherald (1967) and Romps (2011).

The second gas Manabe and Strickler (1964) investigated was ozone, which is a strong absorbed of shortwave radiation. Ozone is therefore commonly mentioned in the context of the ozone depletion and the ozone hole. Tropospheric ozone however is also known to act as a greenhouse gas limiting the amount of outgoing longwave radiation (Worden et al., 2008). Ozone in the stratosphere however filters out a large percentage of the incoming shortwave radiation, which would hence reduce the temperature of the surface in radiative equilibrium (see equation 3.2). The ozone mixing ratio in the atmosphere is not uniform as can be observed in figure D.2. In these experiments the ozone profiles are equal to the RRTMG ozone profile multiplied by a height-independent factor.

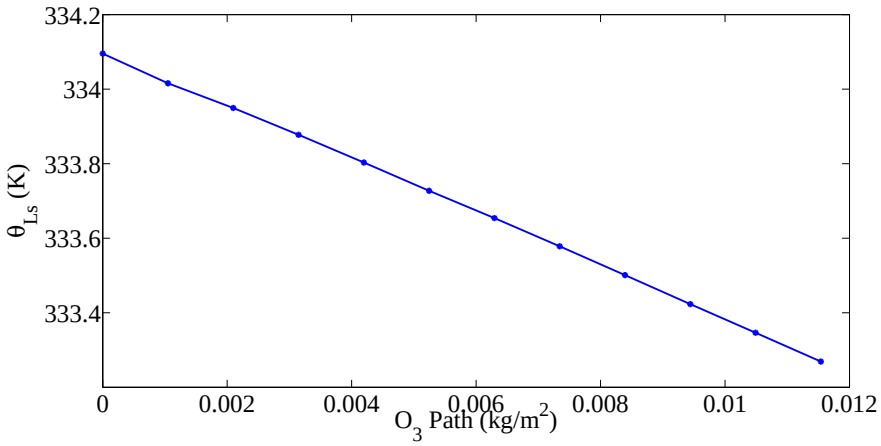

Figure 5.8: Effect of ozone concentrations on the surface potential temperature. The ozone distribution varies with height (see figure D.2). Increasing the amount of ozone results in a very small decrease in temperature. The RRTMG ozone profile contains $5.2g/m^2$ of ozone, equivalent to 245 Dobson units. Doubling this amount decreases the temperature by $0.4K$.

The results of these experiments show that ozone results in a very slight decrease of the surface temperature. This seems to suggest that the shortwave absorbing effects of the stratospheric ozone dominate over the greenhouse gas effects of tropospheric ozone in these simulations. Increasing the ozone concentrations results in more shortwave absorption in the stratosphere, hence cooling the surface as less shortwave radiation reaches the surface. Increasing the ozone concentration reduces the surface temperature slightly, but the temperature in the stratosphere increases substantially when the ozone concentration is increased as can be observed in figure 5.9.

A larger ozone concentration results in more absorption of incoming shortwave radiation which heats the stratosphere as observed in these simulations. The work of Manabe and Wetherald (1967) used ozone distributions corresponding to several different latitudes and these results confirmed that an increase in ozone concentration warmed the troposphere and lower stratosphere. The upper stratosphere cooled down with increasing ozone concentration in their results but this region has not been researched in this thesis.

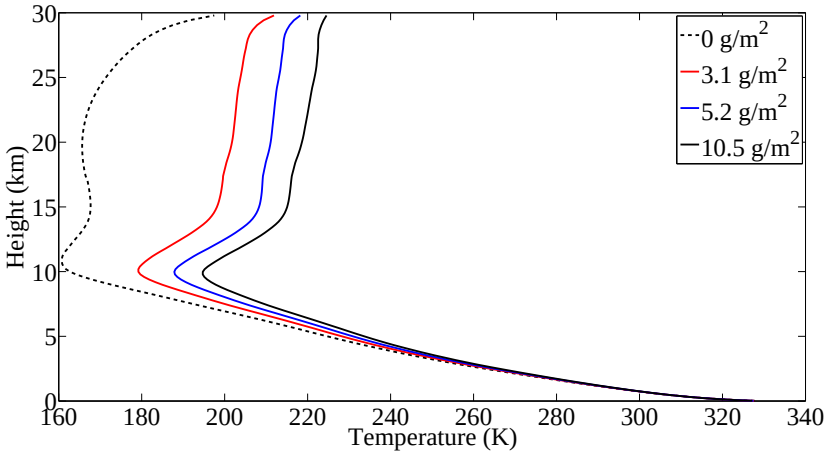

Figure 5.9: Effect of ozone concentrations on the temperature profile in radiative equilibrium. Addition of ozone has a substantial effect on the temperature profile in the stratosphere, due to the absorption of shortwave radiation. The effect of addition of ozone on the lower atmosphere is very small.

The third gas investigated by Manabe and Strickler (1964) was water vapor. Cloud water has a large effect on the climate because of the optical effects of liquid or ice clouds. Water vapor itself however also has profound effects on the radiation as water is a strong absorber in the longwave spectrum (Modest, 2013b). The distribution of water vapor varies with height as can be observed in figure 3.1. The water vapor mixing ratio in the troposphere decreases with height. In the stratosphere the water vapor mixing ratio increases slightly with altitude. In the experiments of figure 5.10 the mixing ratios were increased or decreased at every height with the same factor. These simulations have been performed without liquid water or ice. If the water mixing ratio becomes supersaturated no liquid water is created.

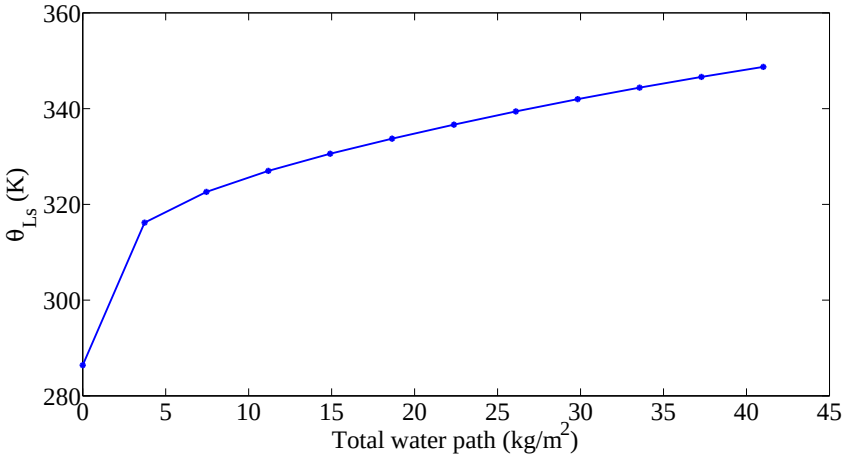

Figure 5.10: Effect of water vapor concentrations on the surface potential temperature. The water vapor distribution in these simulations varies with height (see figure 3.1). Increasing the amount of water vapor results in a large increase in surface temperature. The water vapor profile from the radiative equilibrium experiments contains $18.6kg/m^2$ of water vapor. Clouds have been turned of in these experiments. Doubling the amount of water vapor from $18.6kg/m^2$ as used in the simulations from Manabe to $37.3kg/m^2$, increases the temperature by $12.9K$.

Increasing the amount of water vapor results in an increasing surface temperature. This is consistent with the greenhouse effect of water vapor. Water vapor is a strong longwave absorber, a part of the upward longwave radiation from the surface is absorbed by the water vapor and partially emitted downward, which increases the temperature near the surface. In the stratosphere however addition of water vapor appears to cool down the atmosphere, similar to the simulations of Manabe and Wetherald (1967). A possible explanation for this phenomenon is the fact that as the troposphere becomes warmer it emits more longwave radiation upwards. As the net flux should be zero, the stratosphere has to become cooler, emitting less longwave radiation to compensate for the increased amount of longwave radiation of the troposphere.

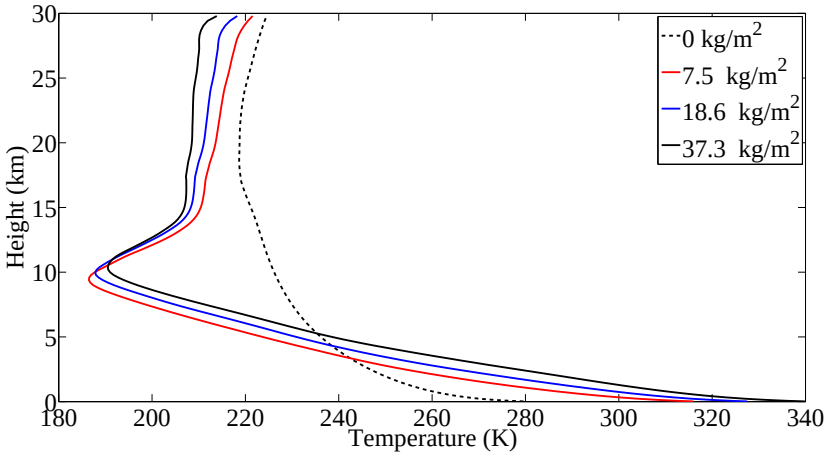

Figure 5.11: Effect of water vapor on the temperature profile in radiative equilibrium. Addition of water vapor to the atmosphere results in a vast increase in the surface temperature. Further increasing the amount of water vapor results in a warmer troposphere and a colder stratosphere. The warming of the troposphere confirms the greenhouse effect of water.

These experiments show that changing the concentration of gasses can have substantial effects on the temperature of the atmosphere in radiative equilibrium. Of the three investigated gasses (CO_2, H_2O and O_3), water vapor has the largest effect on the surface temperature and troposphere temperature. In reality water probably has an even larger effect if clouds are formed because of the optical properties of clouds. In the subsequent chapter clouds, precipitation and convection will be added to the simulation to perform simulations in radiative-convective equilibrium.

Chapter 6

Radiative-Convective Equilibrium Results

In the previous chapter simulations with only radiative heat transfer were discussed. In reality more processes affect the atmosphere. The simulations of this chapter hence have added processes such as clouds, convection and precipitation. In the first set of experiments a simulation in radiative-convective equilibrium is compared with simulations with only radiative heat transfer. Afterwards simulations with different values of surface temperatures have been performed to determine the effect of changing the surface temperature. In the last section the three-dimensional fields of these simulations have been analyzed to more detail to better understand the achieved results.

6.1 Comparison with Radiative Equilibrium

In the previous chapter it was observed that the atmosphere in radiative equilibrium was inherently unstable. This can be observed from the virtual potential temperature profiles in figure 5.3. This instability can cause buoyancy-driven convection which will move the temperature profile towards a more stable situation. Moreover processes such as clouds and precipitation can also affect the temperature profile in the atmosphere. The simulations of this chapter are performed using insolation input different from the previous chapter; an insolation-weighted zenith angle of 38.7° and a solar constant of $571 W/m^2$ are used. The emissivity of ground is 0.95 and the albedo is 0.05.

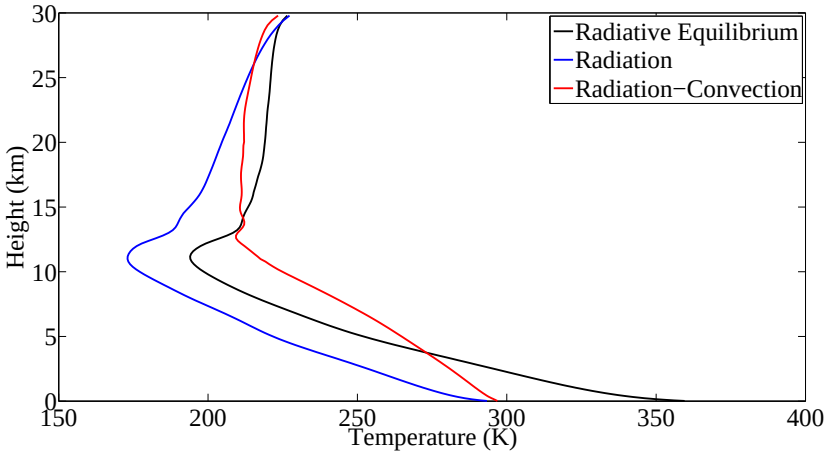

Figure 6.1: Effect of convection on the temperature. Two simulations using the same insolation input are used to determine the effect of convection. One simulation (blue) uses only radiative forcings without clouds, whereas the other simulation (red) is a simulation with convection, clouds, radiation and precipitation. Inclusion of these effects changes the average tropospheric lapse rate from $10.8K/km$ to $6.9K/km$. Both the red and the blue simulation have the same fixed surface temperature of 26°C ($299.15K$). Note that the blue simulation is not in radiative equilibrium as the net flux is nonzero, for comparison a simulation in radiative equilibrium (black) has been plotted as well. The absolute surface temperature in radiative equilibrium is very high, $367.49K$, which is close to the boiling point of water. The temperature in radiative equilibrium is hence considerably higher than in the previous experiments, because the amount of incoming solar energy is higher as well; $446W/m^2$ as compared to $348W/m^2$ in the experiments of the previous chapter.

In figure 6.1 the results of three simulations can be observed all of which use the same insolation input. The red line is a radiative-convective simulation with convection, clouds, radiation and precipitation at a surface temperature of 26 °C. The water vapor mixing ratio profile is determined by DALES in the radiative-convective situation, this profile is used as input in the other two simulations of this figure. The blue simulation uses only radiative heat transfer but is not in radiative equilibrium as the net radiative flux is nonzero. The black line is a simulation in radiative equilibrium.

The average tropospheric lapse rate in radiative-convective equilibrium is $6.9K/km$ and $10.8K/km$ for the simulation with only radiative heat transfer (blue). The tropopause inversion in the simulations without convection is located at 11 kilometers in both cases. The tropopause inversion moves up from 11 kilometers to 12.5 kilometers when convection is included. This behavior is similar to the results of Manabe and Strickler (1964) who observed that the tropopause inversion moved upward from 10 kilometers to 13 kilometers in their research. This can be explained as an effect of convective mixing in the troposphere. As observed in the simulations of radiative equilibrium (see figure 5.3) the atmosphere in radiative equilibrium is unstable. These destabilizing effects from radiation serve as a driving force for buoyancy-driven convection.

An interesting observation in this simulation is the temperature behavior above the troposphere, the temperature profile shows some spatial oscillations in the vertical direction. This behavior is also observed in the liquid potential temperature θ_l, the prognostic temperature variable in DALES and in the water vapor mixing ratio q_t. A possible explanation for this lies in the advection scheme, as advection acts on both of these prognostic variables. Even though a modified version of the WENO scheme is used (see section 4.1.2) the profiles still show oscillatory behavior. In both the liquid potential temperature and water vapor mixing ratio a discontinuity in θ_l and q_t is observed in the tropopause which can cause oscillatory behavior (Blossey and Durran, 2008). Note that these oscillations are not oscillations in time but in space. Apparently the WENO scheme is not capable of completely damping out these oscillations. Additional modifications in the DALES code were necessary as the water vapor mixing ratio in the oscillating part of the atmosphere could become negative in these simulations. These oscillations can persists because they occur in the stratosphere, where there is limited vertical (turbulent) transport because of the strong stratification and hence the spatial oscillations are not smoothed out.

6.2 Effect of Surface Temperature

One of the effects of climate change is a change in the temperature of the sea. A warmer sea results in more evaporation and hence a higher latent heat flux. Aside from this the upward longwave radiative flux should increase as well. To test the effect of a changing surface temperatures four simulations in radiative-convective equilibrium have been performed with sea surface temperatures of 22˚, 24˚, 26˚and 28˚C. These temperatures are commonly measured at the latitude and time of year of these experiments; 17˚N in mid-July (NOAA, 2015). As some fluctuations in the domain might still occur values averaged over the last 2 days of the simulations are used in the graphs and tables of this section unless specified otherwise.

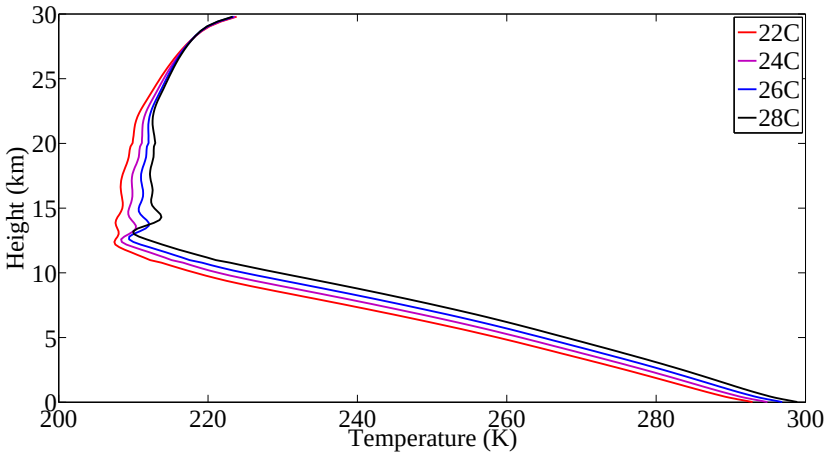

Figure 6.2: Radiative-Convective Equilibrium at several prescribed values for the SST. Sea surface temperatures of 22˚, 24˚, 26˚and 28˚C have been used in these simulations. These simulations include liquid and ice clouds. The altitude of the tropopause inversion increases with surface temperature. Near the top of the domain the temperature is approximately the same for these surface temperatures.

These simulations show that a warmer surface temperature results in a warmer troposphere and lower stratosphere. The temperature profiles closely resembles standards atmospheres such as the U.S. standard atmosphere or the International Standard Atmosphere (NOAA et al., 1976; ISO, 1978). Similar tropospheric and stratospheric lapse rates are observed. Compared to the simulations of Held et al. (1993) the atmosphere in these simulations has a higher lapse rate. Held et al. found that their RCE simulations resulted in lapse rates very close to the saturated adiabatic lapse rate throughout the entire troposphere. The tropospheric inversion in their results occurred at a higher altitude of approximately 18 kilometers for surface temperatures of 25°C and 30°C. The results of Held et al. (1993) are displayed in figure A.3 in appendix A.2. Other simulations such as the work of Robe and Emanuel (1996) display that the lapse rate at tropical latitudes is relatively close to the saturated lapse rate as well.

The simulations of this thesis have not used exactly the same settings of Held et al. (1993). To compare the environmental lapse rate to the saturated lapse rate the ratio of these lapse rates is calculated. The saturated lapse rate can be calculated using equation 6.1 (Rogers and Yau, 1989; AMETSOC, 2015),

$$\Gamma_s = g\frac{1+\frac{L_v q_{sat}}{R_d T}}{c_p+\frac{\epsilon L_v^2 q_{sat}}{R_d T^2}}. \tag{6.1}$$

The ratio is plotted in figure 6.3. Around 6 kilometers the environmental lapse rate is approximately equal to the saturated lapse rate for about 4 kilometers. The exact height of this location increases with surface temperature. The lapse rate in the first kilometer from the surface is approximately 2 to 2.5 times the saturated lapse rate, which results in a lapse rate close to the dry adiabatic lapse rate, as this area is well-mixed and unsaturated. These results clearly show that the lapse rate in the lower troposphere is not equal to the saturated lapse rate, unlike the results of Held et al. (1993). Apart from the lowest

2 kilometers the lapse rates of the RCE simulations of thesis, are relatively close to the saturated lapse rates in the troposphere.

According to research such as Held et al. (1993) the lapse rate for radiative-convective equilibrium at tropical conditions should be close to to the saturated lapse rate, which is observed in figure 6.3 as the ratio of the environmental to saturated lapse rate is close to 1 in the troposphere. Near the surface the air is often unsaturated and the lapse rate should be approximately equal to the dry adiabatic lapse rate, as is observed for the lower 500 meters.

In the stratosphere the lapse rate is not expected to follow the saturated adiabatic lapse rates, as the stratosphere is heavily influenced by radiative processes, which result in an increasing temperature with altitude. This is clearly observed in figure 6.3, which shows that the environmental lapse rate starts deviating substantially from the saturated lapse rate in the stratosphere.

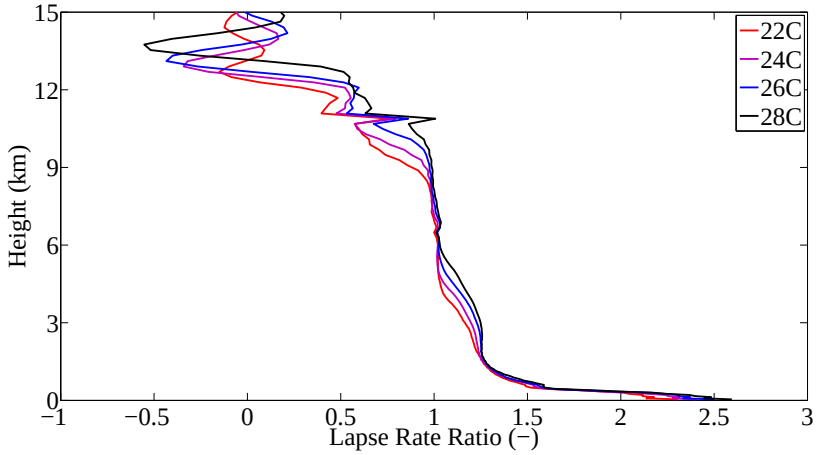

Figure 6.3: Ratio of environmental to saturated temperature lapse rates. When this ratio is close to 1 the environmental lapse rate is close to the saturated temperature lapse rate.

The simulations showed that a higher surface temperature results in increased temperatures of the lower troposphere. According to the Clausius-Clapeyron relation warmer air can contain more water vapor, the absolute humidity of the air in the lower troposphere hence increases. As the air rises upwards more water vapor is available for condensation in the simulations with a warmer surface. The air remains warmer when rising upwards, which results in a lower lapse rate as can be observed in table 6.1.

Under conditionally unstable conditions the environmental lapse rate should be positioned between the saturated lapse rate and the dry lapse rate. The dry lapse rate is approximately $9.8K/km$. In table 6.1 Γ_e is the mean environmental lapse rate and Γ_s is the mean saturated adiabatic lapse rate for the lower five kilometers. The troposphere in these simulations is hence conditionally unstable in all four cases. The convective available potential energy CAPE is calculated as well, the calculations will be explained in subsequent paragraphs. The CAPE is associated with a theoretical vertical velocity w_{CAPE}, which is is compared to the maximum observed vertical velocities w_{max} of these simulations as well.

Table 6.1: Lapse Rates for Lower 5 Kilometers and CAPE

SST $^{\circ}C$	Γ_e K/km	Γ_s K/km	CAPE J/kg	w_{CAPE} m/s	w_{max} m/s
22	6.85	5.61	2234	66.8	18.9
24	6.63	5.32	2721	73.8	19.8
26	6.45	5.03	3361	82.0	20.8
28	6.23	4.75	3906	88.4	21.7

The environmental lapse rate decreases with increasing surface temperature, which suggests a more stable atmosphere if the saturated lapse rate remains the same. The saturated lapse rate however depends on temperature and humidity as well and therefore decreases with surface temperature. The difference between the environmental and saturated lapse rate increases with temperature, which would suggest a more unstable troposphere at higher surface temperatures.

To quantify the instability of the troposphere the convective available potential energy (CAPE) is used. CAPE is defined as the energy an air parcel would have it would have been lifted a certain distance by buoyancy. Atmospheric instability is often measured using the CAPE. To calculate the CAPE an air parcel at the lifted condensation level (LCL) is created and lifted upwards. The LCL is positioned at the cloud base. The wet air parcel will follow the moist adiabat and will intersect the environmental temperature profile twice. The first intersection is at the level of free convection (LFC), the second intersection is the equilibrium level (EL). Between these points the air parcel is positively buoyant and hence accelerating. Integrating the buoyancy force between these points using formula 6.2 provides the CAPE.

$$CAPE = \int_{z_{LFC}}^{z_{EL}} g \left(\frac{\theta_v^{parcel} - \overline{\theta_v}}{\overline{\theta_v}} \right) dz, \tag{6.2}$$

$$w_{CAPE} = \sqrt{2 \times CAPE}. \tag{6.3}$$

Table 6.1 shows that the CAPE increases with surface temperature. The atmosphere is hence more unstable at higher surface temperatures. The simulations however show that in the lower 9 kilometers the CAPE integrals produces roughly the same CAPE, indicating that the lower 9 kilometers are approximately equally stable.

The higher CAPE values can most likely be attributed to the higher altitude at which the stratosphere begins. The warmer surface temperature results in higher tropopause, therefore the air parcels remain positively buoyant up to higher altitudes increasing the CAPE. In figure 6.4 it is observed that the main contribution to the CAPE difference is located at the top of the troposphere.

The increased CAPE is associated with a higher vertical velocity w_{CAPE}. Vertical velocity values as high as w_{CAPE} are not observed, but the maximal vertical velocities w_{max} in DALES are increasing with surface temperature as can be observed in table 6.1. The clouds can hence overshoot the equilibrium level to reach higher altitudes. This results in a higher tropopause.

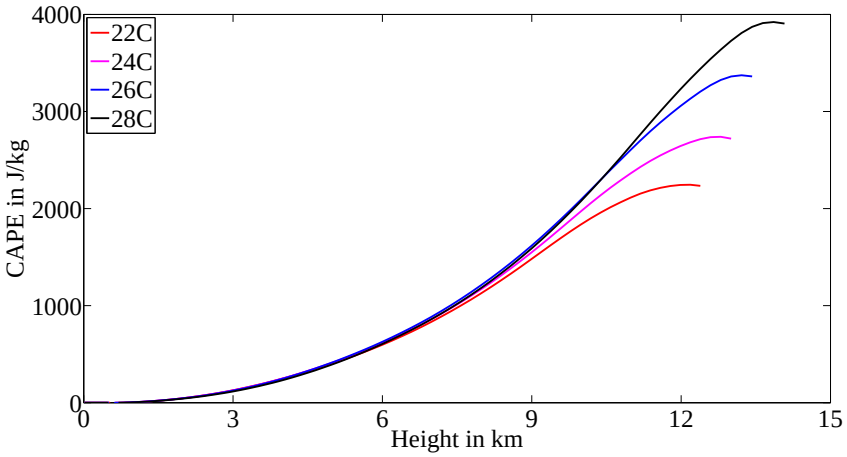

Figure 6.4: CAPE integrals as a function of height. In formula 6.2 the equilibrium level z_{EL} is replaced by a variable height z. The value of the CAPE integrals for four SSTs has been plotted as a function of this height z. The real value of the CAPE is the maximum of these curves, located at $z = z_{EL}$, the rightmost point in this graph. This plot shows that the CAPE contributions for the lower 10 kilometer are approximately the same for these four surface temperatures. A higher surface temperature results in a higher tropopause and hence a higher equilibrium level z_{EL}. The CAPE integral is performed to a higher altitude, increasing the CAPE. The main contribution to the CAPE is the increased size of the unstabile area at the top of the troposphere.

Previous results showed that the temperature profiles in radiative-convective equilibrium changed with a changing surface temperature. According to the Clausius-Clapeyron relation warmer air can contain more water vapor. Therefore the total water mixing ratio q_t has been plotted for these four simulations in figure 6.5. Note that these profiles show the same oscillatory behavior at the top of the troposphere. The sharp peak around 12 kilometers is due to the oscillatory behavior which pushes the humidity towards zero.

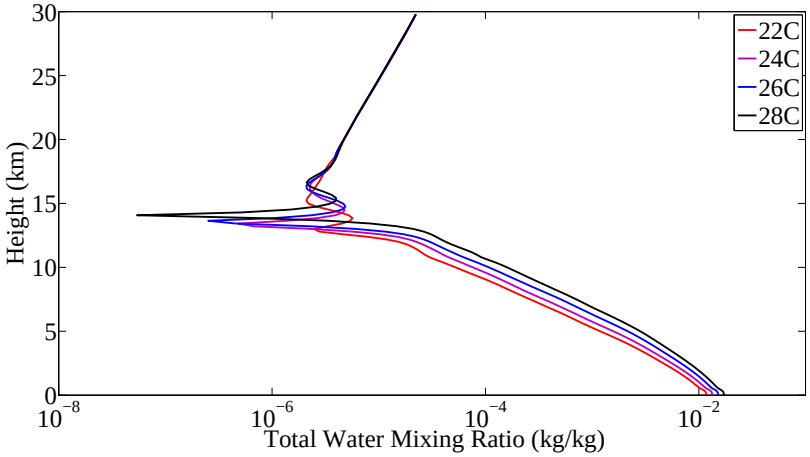

Figure 6.5: Water vapor mixing ratio at several prescribed SSTs. The water vapor mixing ratio is plotted on a semi-logarithmic plot. A higher surface temperature results in a more humid troposphere. The total water path is $28.84 kg/m^2$, $33.87 kg/m^2$, $40.06 kg/m^2$ and $47.09 kg/m^2$ respectively. The height of the oscillations increases with temperature and is located at approximately the same height as the temperature oscillations of figure 6.2.

A higher surface temperature results in a warmer atmosphere. According to the Clausius-Clapeyron relation the amount of water vapor the atmosphere can contain increases by 7% per degree. The atmosphere can therefore contain more water vapor. From these data the relative humidity of the air can be calculated. This has been plotted for the lower 15 kilometers in figure 6.6.

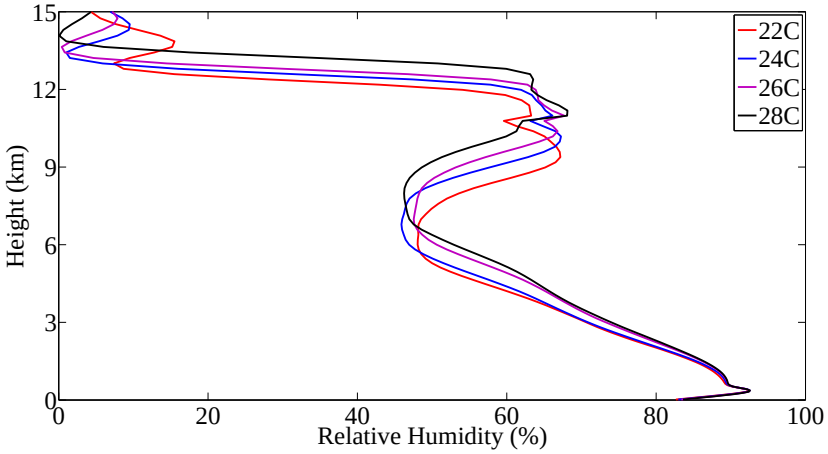

Figure 6.6: Relative humidity profiles at several SSTs. The relative humidity of the simulations has been plotted for the lower 15 kilometers. The relative humidity in the lowest 800 meters is approximately the same, above this layer however the relative humidity differs between the simulations.

The relative humidity in the layer near the surface is approximately equal for all four simulations. Above this layer however the relative humidity decreases in all four cases. The relative humidity above this layer is higher for the higher surface temperatures. After a certain height, the relative humidity increases again. This height depends on the surface temperature. As the surface temperature is higher, air can rise higher and transport moisture upward further.

In the radiative-convective equilibrium simulations of Sui et al. (1994) the relative humidity has also been plotted as a function of height. The behavior in the lowest 5 kilometers is approximately the same. In the results of this thesis however the relative humidity increases above a height of 5 kilometers, whereas the relative humidity in the work of Sui et al. (1994) continues declining. Sui et al. however mentioned that their results were not consistent with observations, which do in fact show the increase in relative humidity after a certain altitude. Research by Held et al. (1993) and Romps (2011) showed that in their radiative-convective equilibrium simulations the relative humidity started increasing after a certain height, consistent with the observations. Compared to their results however the drop in relative humidity at the top of the troposphere is located at a lower altitude in the simulations of this thesis. The results of Held et al. (1993) also show that increasing the surface temperature increases the altitude of the point where the relative humidity increases with height. The results of Held et al. (1993) and Sui et al. (1994) can be found in appendix A.2.

The increase in relative humidity above 5 kilometer in these simulations is associated with clouds. Clouds at these altitudes are often cirrus clouds and hence largely composed of ice. Even though the slab-averaged humidity is almost always below saturation large cloud fraction are observed as can be seen in figure 6.7.

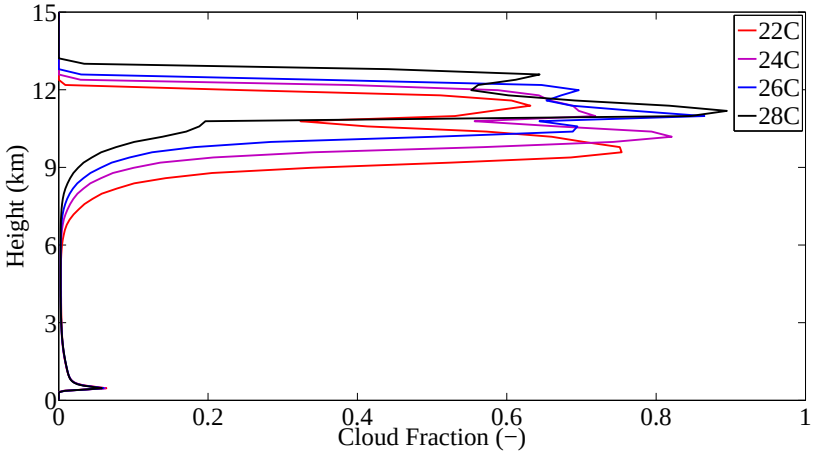

Figure 6.7: Cloud Fraction in radiative-convective equilibrium for several prescribed SSTs. These results are the average cloud fractions of the last 48 hours of the simulation. Only the lower 15 kilometers have been plotted as no clouds exist above this height. The average cloud fraction for the lower 6 kilometers is approximately the same for all four SSTs.

A large cloud fraction is observed at the top of the troposphere, in the underlying part of the domain the cloud fraction is much smaller. At approximately 500 meters a local maximum in the cloud fraction is observed, this is at the top of the subcloud mixed layer. Above this altitude very low cloud fractions are observed, the results of Islam et al. (1993) show low cloud fractions at these altitudes as well. The very high cloud fractions at the top of the troposhere are similar to the results of Islam et al. (1993).

Similar to the results of the relative humidity plots it is observed that the moisture and hence the clouds reach higher altitudes if the surface temperature is higher. The top of the clouds corresponds to the tropopause temperature inversion of figure 6.2. The cloud fraction in the lower 6 kilometers however is approximately the same for the four values of the surface temperature. This is in agreement with the results of the relative humidity, which is also approximately the same in the lower 6 kilometers for the four values of the surface temperature. Moreover, the CAPE integrals (figure 6.4) show that this region of the troposphere is approximately equally stable in these four situations.

At the top of the troposphere the distribution of the cloud fraction shows a dip above the maximum in cloud fraction. It is unknown if this is physical or numerical, but simulations of Robe and Emanuel (1996) also displayed this kind of behavior. The maximum cloud fraction appears to increase with surface temperature. The thickness of the cloud layer appears to decrease with surface temperature. Note that this refers to the cloud fractions, not the cloud densities.

The plots of the profiles in the atmosphere showed that the surface temperature has an effect on the humidity and temperature profiles of the atmosphere. The surface temperature affects the surface fluxes directly. Therefore the surface fluxes have been investigated.

Table 6.2: Surface Fluxes at Several Surface Temperatures

SST $^{\circ}C$	Sensible Heat W/m^2	Latent Heat W/m^2	Longwave Down W/m^2	Shortwave Down W/m^2	Precipitation mm/day
22	8.15	67.87	352.56	314.65	1.60
24	8.14	74.67	369.40	312.72	1.69
26	8.25	82.31	387.18	309.98	1.83
28	7.98	89.57	405.51	307.80	2.00

The sensible heat flux does not appear to change significantly with the surface temperature (SST). As the lowest layers of the atmosphere are well-mixed the temperature difference between the surface and the first level of the LES domain remains small, even if the SST increases. The liquid potential temperature difference is approximately constant ($1K$) for these four surface temperatures. The sensible heat flux depends on the temperature difference, as this temperature difference does not change with surface temperature, the sensible heat flux is roughly independent of the surface temperature as well.

The latent heat flux however increases substantially with surface temperature. The higher SST results in a warmer atmosphere, which increases the saturated water vapor content by about 7% per degree according to the Clausius-Clapeyron relation. In the lower 800 meters the relative humidity is approximately the same for the four investigated surface temperatures, as can be seen in figure 6.6. The water vapor content, or absolute humidity, increases because the increased saturated water vapor content. The latent heat flux in DALES is proportional to the difference of the saturated water vapor content at the surface and the water vapor content at the first atmospheric level at 10 meters. This difference increases with higher surface temperatures, because both the saturated vapor content at the surface and the water vapor content at 10 meters increase by 7 % per degree according to the Clausius-Clapeyron relation. Therefore the latent heat flux increases as well.

As more water enters the atmosphere by evaporation, more precipitation should fall to remove water from the atmosphere. In equilibrium these fluxes should be equal. To compare these fluxes the precipitation flux needs to be converted to W/m^2 using the latent heat. The fluxes in these experiments are not equal and a 21 to 31 W/m^2 difference is observed. This difference should result in an increase of the total water path (TWP) of 0.03 to 0.04 $kg/m^2/h$. In the last 2 days the TWP should have increased by more than 1 kg/m^2 which is not observed as the TWP is approximately constant. In the beginning of the simulation, when precipitation has not formed yet, the increase in TWP is equal to the latent heat flux.

The temperature of the atmosphere increases with increasing surface temperature resulting in a larger downward longwave flux from thermal radiation of the atmosphere. This is partially compensated by the fact that the amount of shortwave radiation is reduced in a warmer atmosphere. This could be an effect of the shortwave blocking effects of clouds. A similar reduction in shortwave radiation at the surface however was also observed in the water vapor experiments of section 5.3. In these experiments the amount of water vapor was increased, but clouds could not form, yet the amount of shortwave radiation at the surface was still reduced due to absorption of atmospheric gasses.

To quantify the effect of clouds more accurately the cloud radiative effect needs to be quantified. This can be calculated using the clear-sky radiative fluxes, which are also calculated by the radiative transfer code. The cloud radiative effects are calculated following Ramanathan et al. (1989) as described in he following equations, which can also be found in appendix C.4. In these equations TOA refers to the top of the atmosphere and *cloudy* and *clear* refer to the cloudy and clear-sky radiative fluxes,

$$LWCRE = \left(LW^{\uparrow}_{TOA}\right)_{clear} - \left(LW^{\uparrow}_{TOA}\right)_{cloudy}, \tag{6.4}$$

$$SWCRE = \left(SW^{\uparrow}_{TOA}\right)_{clear} - \left(SW^{\uparrow}_{TOA}\right)_{cloudy}. \tag{6.5}$$

The cloud-fractions of figure 6.7 show some dependency to the surface temperature, but to determine the total amount of the clouds the cloud water path is used. Table 6.3 displays the column amounts of total and liquid water and the magnitude of the cloud radiative effect.

Table 6.3: Cloud-Radiative Effect

SST $^{\circ}C$	Total Water Path kg/m^2	Cloud Water Path g/m^2	Shortwave CRE W/m^2	Longwave CRE W/m^2	CRE W/m^2
22	28.84	19.59	-20.39	21.37	0.98
24	33.87	19.17	-19.55	20.78	1.22
26	40.06	20.10	-19.23	19.73	0.50
28	47.09	20.07	-18.44	18.85	0.41

Although the total amount of water in the atmosphere increases by approximately 8% per degree increase in surface temperature, the amount of cloud water does not change substantially. The 8% increase is more than the 7% predicted by the Clausius-Clapeyron relation, therefore the atmosphere should experience an increasing relative humidity as is consistent with figure 6.6.

Clouds have been shown to affect the climate through the cloud radiative effect, commonly abbreviated as CRE (van der Dussen, 2015). Incoming shortwave radiation from the sun is reflected by clouds into space. As the albedo of clouds is larger than the albedo of the ocean surface, clouds generally result in more reflection of shortwave radiation hence cooling the atmosphere (Ramanathan et al., 1989). The shortwave CRE is therefore generally negative.

Longwave radiation from the surface is absorbed by the clouds, which heats up the clouds. These clouds emit part of the radiation upwards and part backwards. The clouds however are generally colder than the surface, hence less thermal radiation is emitted into space. The longwave CRE is therefore generally positive.

As the magnitude of the shortwave and longwave cloud radiative effects in these experiments are approximately equal, the total cloud radiative effect is approximately zero. Above oceans in the tropics it is commonly observed that the shortwave and longwave cloud radiative effects approximately cancel each other out (Ramanathan et al., 1989). The near cancellation of these cloud radiative effects does not imply that clouds do not affect the climate significantly. The shortwave CRE mainly causes extra heating at the top of the troposphere and cooling in the lower troposphere. The longwave cloud radiative effect reduces the longwave cooling in almost the entire troposphere thus heating up the troposphere. This is consistent with the findings of Ramanathan (1987, 1989). Although the shortwave and longwave CRE nearly cancel each other out, they act at different heights, hence these effects can significantly change the heating and cooling gradients, which can affect the dynamics as well (Ramanathan, 1987; Ramanathan et al., 1989).

6.3 Three-dimensional structure

In the previous section the focus was on the slab-averaged and time-averaged values of the simulation. In this section the focus will be on the three-dimensional fields instead of the slab-averaged values of these fields. From this three-dimensional data additional information can be retrieved to provide a better insight into the results. This data is data below an altitude of 14 kilometer, because data from high in the sponge layer is less reliable, because of gravity wave damping.

The cloud fractions of the simulations resulted in very high cloud fractions at the top of the tropopause and relatively low cloud fractions below this layer. To achieve a better understanding of the clouds in this simulations the liquid water content field of the 26°C has been plotted. Cloud fields from other simulations had similar structures and have not been compared to the results of other simulations.

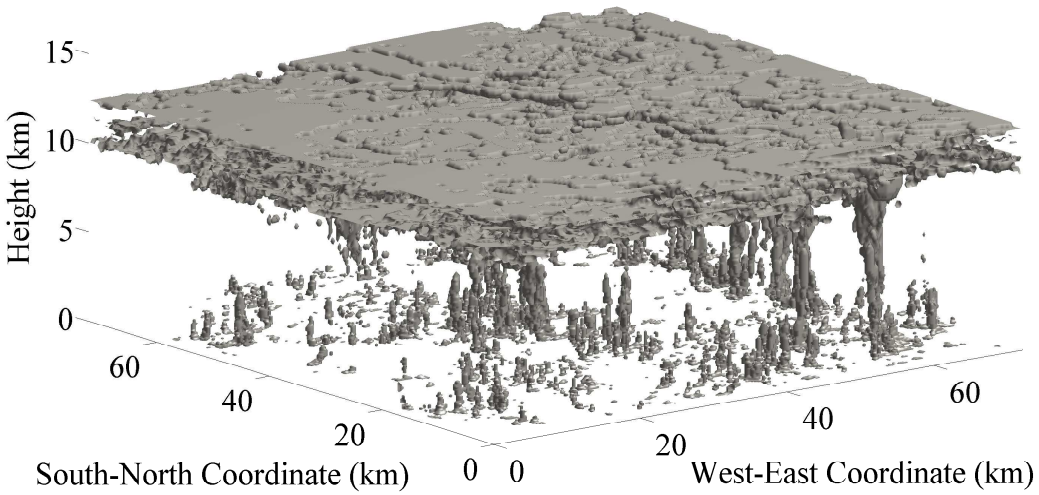

Figure 6.8: Three-dimensional Cloud Field. The cloud field in the 26°C simulation after 240 hours has been plotted. Note that a large cloudy layer exists between 9 and 12 kilometers high. The clouds in the underlying layers generally have small diameters compared to their vertical development.

In this figure it is clearly observed that a lot of clouds exist between 9 and 12 kilometers, the domain is almost entirely cloudy at this location. Clouds at this height are usually cirrus clouds composed largely of ice and hence have limited effect on the radiation. Similar results were attained by Islam et al. (1993) who found a large saturated cloud layer between 8 and 14 kilometers. In the lowest kilometer some small diameter cumulus-like clouds occur. It is interesting to observe that some of these clouds are vertically well developed, but have a relatively small diameter. At the right corner of this figure some clouds are observed that bridge the entire troposphere. Clouds with this kind of vertical development can exist in nature, such as cumulonimbus clouds or cumulus congestus clouds. Cumulonimbus clouds however often have diameters of several kilometers, much larger than the diameters in this simulation. The clouds in these simulations more closely resemble the cumulus congestus clouds, which are generally higher than they are wide. The simulations of Islam et al. (1993) also displayed vertically well-developed clouds. Vertically developed clouds were also observed in the simulations of Robe and Emanuel (1996), but the cloud fractions near the top of the troposphere were much smaller. Results of Robe and Emanuel (1996) and Islam et al. (1993) can be found in appendix A.3.

These vertical clouds generally have high upward velocities of for example 10 m/s in their core and lower subsiding velocities of 2 m/s at the shell surrounding the cloud core. In shallow cumulus clouds this behavior has been observed in the observations of Rodts et al. (2003) and also in LES simulations such as in the work of Heus and Jonker (2008). Their explanation for this downward moving shell is evaporative cooling; saturated air from the core is moved towards the edges where it reaches unsaturated air. Lateral mixing of the saturated air from the cloud with the unsaturated environment causes this liquid water to evaporate, cooling the air at the cloud shell in the process. The cool air is negatively buoyant and is hence accelerated downwards. LES uses gridbox-averaged values the gridbox is either saturated and cloudy or unsaturated. Small lateral movements of the entire cloud causes part of the cloud to enter an unsaturated gridbox and these parts are instantly evaporated. The evaporative cooling can therefore be stronger than in nature, which could limit the lateral growth of the cloud systems.

Simulations by Pauluis and Held (2002) found similar velocity structures in convective cells for radiative-convective equilibrium. The diameter of the convective cells in the research of this thesis however more closely resembles the dry cells rather than the moist cells of the research of Pauluis and Held (2002).

In the cloud plot large patches without any low level clouds are observed as well. It is illustrative to plot a contour plot of the total water path as well.

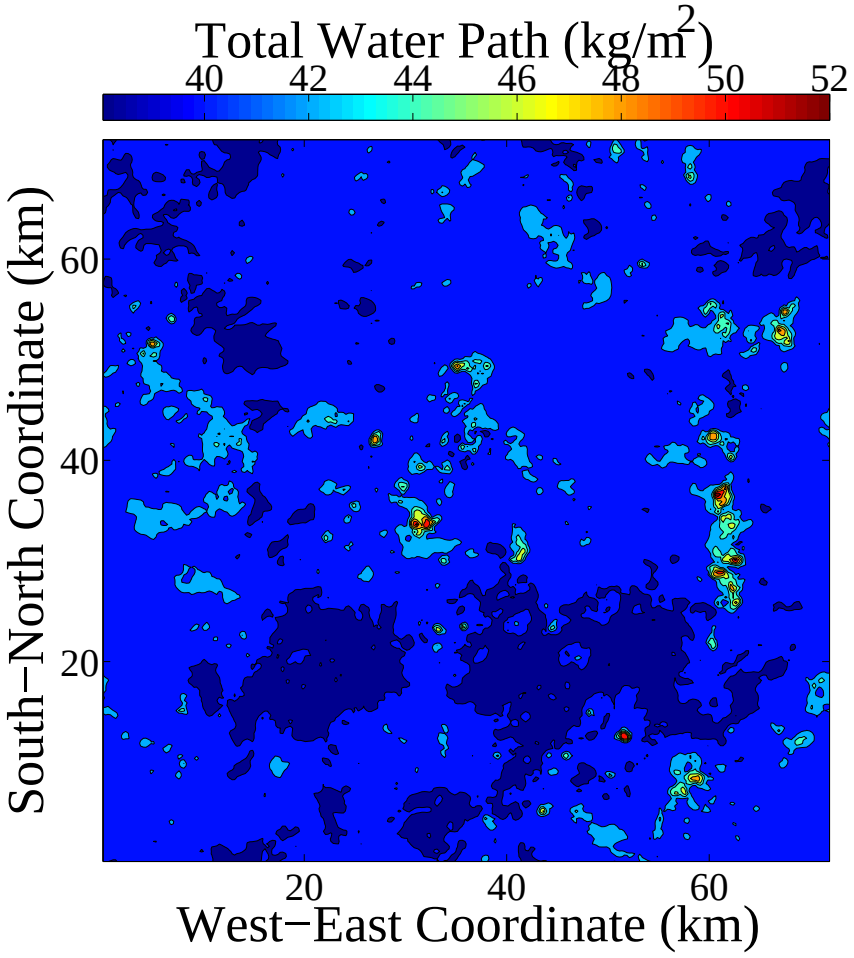

Figure 6.9: Total water path in kilograms per square meter of the 26°C simulation after 240 hours. Note that distribution of water content is not entirely random and some clustering appears to have taken place. Some areas have become somewhat dryer.

In the total water path contour plot dry patches can be observed (dark-blue) as well as some relatively humid areas (yellow, red). The TWP difference between these areas is $12 kg/m^2$. The relatively humid areas are locations of low clouds. The distribution of water vapor is not entirely random as some clustering is observed. In RCE experiments by Wing and Emanuel (2014) however very strong clustering of water was observed. In their experiments a large central humid area surrounded by dry patches was formed. Clustering of this magnitude is not observed in the results of this thesis. It should be noted that Wing and Emanuel used a lower resolution (3 km) model on a much larger domain of 768 by 768 kilometers for longer times of up to 100 days. It is unknown whether DALES exhibits the same kind of self-aggregation. Running longer simulations might result in more clustering. The domain size could also be a limitation to the dynamics that are responsible for the self-aggregation.

To evaluate whether the domain size limits the dynamics one can analyze the Fourier spectra of the LES fields as described by de Roode et al. (2004). In this method the ogive is calculated, which is the integral of the spectral density from a certain wavenumber k up to the Nyquist frequency. The critical wavenumber k_c is defined as the wavenumber k where the ogive is equal to two-third of the total variance (de Roode et al., 2004). This means that one-third of the variance resides in wavenumbers below k_c. The critical length scale Λ_c can be calculated by taking the reciprocal of the critical wavenumber. In principle the critical wavenumber can be calculated for several prognostic variables and combinations of prognostic variables.

For this research the characteristic length scales of the total water specific humidity q_t, the horizontal velocity u and the vertical velocity w have been calculated. The first of this prognostic variables is a measure for the cloud structures, the second one is a measure for the velocity structures and the third one serves as a production term for variations in the other fields. Using the ogive the characteristic length scales at all altitudes below 14 kilometers are calculated for the 26 °C simulation at 240 hours of simulated time.

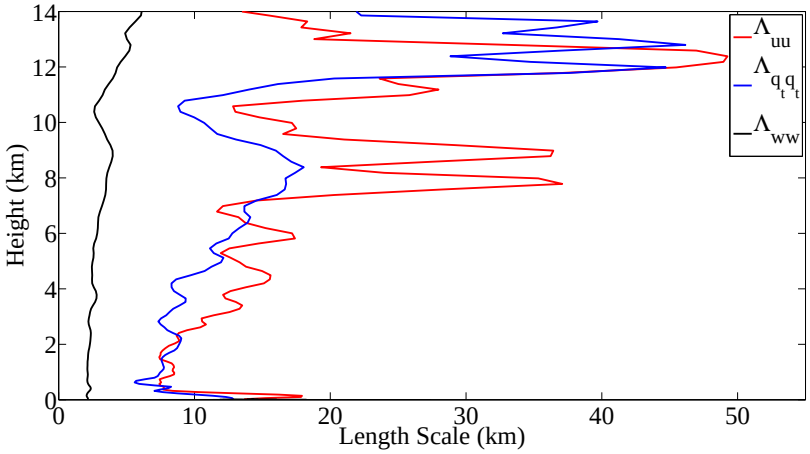

Figure 6.10: Length scales of several fields after 240h of simulation. Using the ogive the characteristic length scales for the vertical velocity Λ_{ww} (black), horizontal velocity Λ_{uu} (red) and total water specific humidity $\Lambda_{q_t q_t}$ (blue).

The values of Λ_{uu} and $\Lambda_{q_t q_t}$ are generally less than 15 kilometers in the layer below the cirrus cloud layer. The characteristic length scales increase with height reaching maximum values of 50 kilometers. Length scales have not been determined for the stratosphere as gravity wave damping damps out variations in this layer. This means that the structures of u and q_t below this layer have length scales of 15 kilometers. Compared to a domain size of 72 kilometers, this means that several of these structures can exist. Near the cirrus cloud layer however the length scales become much larger. This means that a large part of the variance is located at large length scales and the variance is not small. This could indicate that the domain is somewhat too small, as only a limited amount of these structures can exist, which would result in fluctuations.

Vertical velocity determines transport between layers, vertical velocity variance therefore serves as a production term for variance in other fields. The length scales of the vertical velocities are generally small compared to the other length scales, which is as expected as these length scales are limited by the tropospheric height. The length scales of the vertical velocities above 10 kilometers increase, which indicates that more vertical velocity variance is located at the larger wavelengths. This suggests that the variance in other fields will grow more at the larger scales.

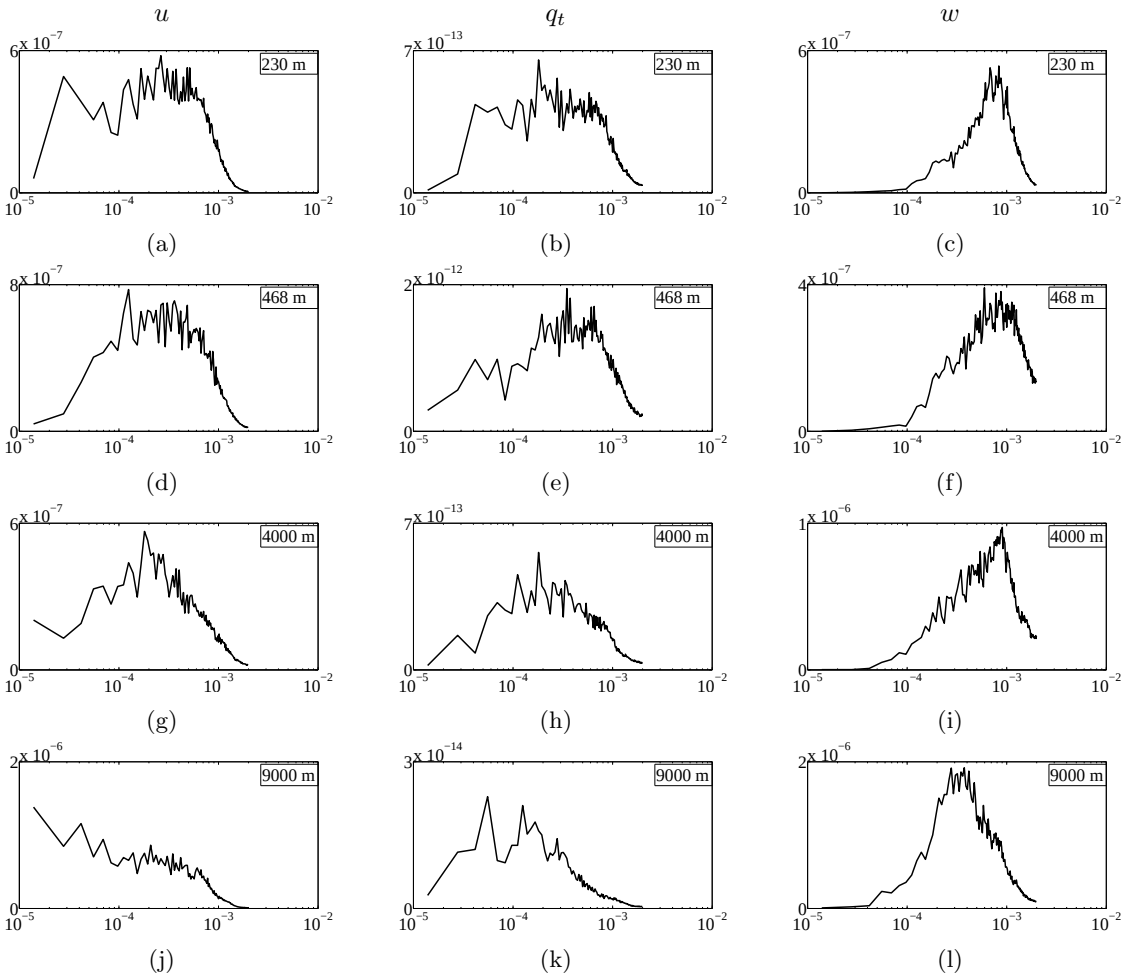

Figure 6.11: Variance spectrum plots after 240 hours of simulated time. The variance spectra multiplied by the wavenumber (kS) have been plotted on the y-axis as a function of the wavenumber (k) on the logarithmic x-axis. The wavenumber on the x-axis is expessed in m^{-1}. The units on the y-axes are m^2/s^2 in the left and right column and kg^2/kg^2 in the middle column. The left column contains u-velocity spectra, the middle column humidity spectra and the right column contains vertical velocity spectra. The first row is data from the boundary layer at 230m, the second row is positioned at the cloud base at 468m. The third row is located at 4 kilometers and the fourth row is located at 9 kilometers in the cloudy layer at the top of the troposphere.

Until the 1980's it was thought that the spectra of turbulent eddies were closely confined to length scales determined by the dissipation length scale (1mm) and the height of the planetary boundary layer (1km) (de Roode et al., 2004). A well-developed turbulent spectrum hence should consist of a single spread-out peak confined by these length scales. This peak may be skewed and often contains some noise. Variations larger than the height of the planetary boundary layer were not expected to occur. Scales larger than the planetary boundary layer are mesoscales.

Research however has shown that fields such as moisture and horizontal velocities exhibit variations located at these mesoscales and that only the vertical velocity spectra followed the shape of a classical turbulent spectrum (de Roode et al., 2004). If mesoscales develop spectral peaks may be located at much larger length scales than that of the turbulent eddies.

The vertical velocity spectra 6.11.c, 6.11.f, 6.11.i and 6.11.l are well-developed turbulent spectra without mesoscale variations. The vertical velocity spectra do not show any mesoscale variations at low wavenumbers, because the vertical velocity spectra are limited by the relatively shallow tropospheric height (de Roode et al., 2004).

Other spectra such as the u-velocity spectrum 6.11.a and humidity spectrum 6.11.b have a large peak in their spectrum positioned at low wavenumbers corresponding to mesoscale structures of 24 and 36 kilometers. These mesoscale structures have formed over the course of the 10 day simulation with a 26°C surface temperature. The size of these mesoscale structures could indicate that the domain is somewhat too small as only a few of these structures can exist in the domain of 72 kilometers.

More striking is the behavior of the u-velocity spectra 6.11.g and 6.11.j, which show that a substantial part of the variance is located at wavenumbers corresponding to the domain size. Spectrum 6.11.j is not shaped as a single peak function. In both of these cases the size of the variance is not small. The horizontal velocities at an altitude of 9 kilometers show strong temporal oscillating behavior as limited possibilities exist to remove this momentum. The direction of the horizontal velocity starts rotating due to Coriolis forces, but is not sufficiently damped. These spectra hence show that the horizontal velocity structures display existence of large mesoscale structures of sizes comparable to the domain size. To achieve good simulations of these velocity structures a larger domain would be necessary.

The humidity spectrum of figure 6.11.k contains two distinct peaks. The total size of the variance in this situation is relatively small compared to the other humidity spectra. It should be noted that the mean humidity at this altitude is about 70 times smaller than the humidity at 230 meters. The variance in the humidity field is hence relatively large and hence this spectrum clearly shows the existence of significant mesoscale structures. Similar to the other spectra 6.11.d, 6.11.e and 6.11.h, the variance spectrum of 6.11.k is located at somewhat small wavelengths. This indicates that the humidity contains some mesoscale structures, which could suggest that a larger domain size could have provided better results.

Some of these spectra such as 6.11.a, 6.11.e and 6.11.k have a dip in their spectrum at a wavenumber of approximately $10^{-4}m^{-1}$, which corresponds to a length of 24 kilometers. Fluctuations at smaller wavenumbers are present. Initially simulations were performed on a smaller domain of $24km \times 24km$ as to get developed input profiles for the simulations on the $72km \times 72km$ domain. The fact that quite a large part of the fluctuations occur at wavenumbers smaller than $10^{-4}m^{-1}$ suggests that increasing the domain to $72km \times 72km$ will likely have improved the quality of the simulations. In the small domain of 24 kilometers some mesoscale structures have formed, but not to the extent of the simulation on the 72 kilometer domain. The behavior of some of the spectra suggests that increasing the domain size further might improve the quality of the simulation by enabling development of more and larger mesoscale structures. In appendix F the spectra of the 26 °C simulation on the $24km \times 24km$ domain after 196 hours of simulated time can be observed.

Chapter 7

Conclusions and Outlook

7.1 Conclusions

One of the goals of this project was to use DALES for simulations of radiation-driven problems. This required adapting DALES and determining applicable settings, grid and input to simulate domains of 30 vertical kilometers. Several modifications were made; ice clouds were implemented and the WENO scheme was modified. Furthermore the recent implementation of the RRTMG radiative transfer code was investigated using simulations of radiative equilibrium, based on the work of Manabe and Strickler (1964).

The radiative equilibrium simulations showed that the temperature profiles in radiative equilibrium closely resembled the results of Manabe and Strickler. These radiative equilibrium profiles however are unstable and would not exist under normal circumstances. Additional simulations showed that addition of ozone was responsible for creation of a tropopause temperature inversion and the corresponding stratospheric temperature profile. Changing of the ozone concentrations however had a very limited impact on the temperature in the troposphere as the surface temperature was almost insensitive to changes in ozone concentration, as is consistent with the expectations. Substantial effects on the stratospheric temperature were observed when the ozone concentration was modified, which is consistent with the common notion that the stratosphere is heavily influenced by the interaction of ozone with solar radiation.

Changing the concentrations of carbon dioxide and water vapor however resulted in significant changes in temperature. In radiative equilibrium water is responsible for the steep lapse rates near the surface and the high surface temperatures. Increasing the amount of water vapor resulted in high surface temperatures and a much warmer troposphere. This can be explained by the greenhouse gas effect of water vapor.

Carbon dioxide is an important greenhouse gas which concentration tends to increase due to anthropogenic emission. Increasing the carbon dioxide concentrations resulted in increasing surface temperatures as well. The impact of changing the carbon dioxide concentrations however was much less substantial. The largest temperature differences in the carbon dioxide simulations were observed in the stratosphere and changes to the tropospheric temperatures were small.

The results of the radiative equilibrium simulations showed that the resulting temperature profiles were inherently unstable. Enabling convection, cloud formation and precipitation resulted in lower lapse rates in the troposphere compared to simulations with only radiative forcing. The troposphere is generally warmer in radiative-convective equilibrium and the top of the troposphere moves upward.

Radiative-convective equilibrium was investigated for surface temperatures of 22°, 24°, 26°and 28°C. Logically, a warmer surface temperature resulted in a warmer troposphere. The lower stratosphere is also warmer, but the effect of the surface temperature diminishes closer to the top of the LES domain. These results show that the temperature lapse rate becomes smaller as the surface temperature increases. The resulting lapse rate is close to the saturated lapse rate in the troposphere above 2 kilometers, but near the surface the lapse rate is approximately equal to the dry adiabatic lapse rate.

Closer inspection of the CAPE reveals that the atmosphere is more unstable at higher surface temperatures, but the CAPE contributions of the lower troposphere are approximately the same for the investigated surface temperatures. Therefore the lower troposphere does not become more unstable with increasing surface temperature. The increase of CAPE with surface temperature can mainly be attributed to higher altitude of the tropopause.

In accordance with expectations from the Clausius-Clapeyron equation, the amount of water vapor in the atmosphere increases with surface temperature. However, the relative humidity in these simulations increased with surface temperature as well. The resulting relative humidity plots were in agreement with other simulations and observations (Held et al., 1993; Sui et al., 1994). The maximum relative humidity is approximately 93% at 400 meters. Additionally the relative humidity plots show a local maximum near 10 kilometers, which coincides with a cloud layer.

The cloud fraction of the lower 6 kilometers is approximately equal in these four simulations. Apart from a peak in cloud fraction of 6% near 400 meters the cloud fraction in the lower 6 kilometers is very low, often less than 1%. Large cloud fractions of up to 90% are observed near the top of the troposphere, but this behavior has been observed in other simulations as well such as the work of Islam et al. (1993). The maximum cloud fraction increases with surface temperature, but the cloud layer becomes vertically less extended.

Looking at the surface fluxes it is observed that the sensible heat flux seems to be insensitive to the surface temperature. Latent heat flux however increases substantially with surface temperature. Air near the surface has the same relative humidity, but is warmer and can hence contain more water vapor. Closure to the hydrological cycle would require the latent heat flux and precipitation heat flux to be equal. Precipitation does increase with surface temperature. Although the total water path of the atmosphere converges, the latent heat flux and precipitation flux do not balance each other. Closer inspection suggests that the statistics of the precipitation does not function properly in these simulations.

Analysis of the surface fluxes indicates that the downward longwave flux increases with surface temperature, which is an effect of the warmer troposphere emitting more thermal radiation. The shortwave radiative flux on the other hand decreases with surface temperature. A likely explanation for this could be the clouds. The cloud fraction showed some dependency on the temperature, but the exact effect of surface temperature was difficult to asses. Calculation of the cloud water path showed that the amount of cloud water appears to be insensitive to surface temperature.

The effect of these clouds on the longwave and shortwave fluxes have been quantified in the cloud radiative effect. The longwave cloud radiative effect is positive and warms the atmosphere. Shortwave cloud radiative effect is negative, indicating a cooling effect of the clouds. The magnitude of these effects decreases with surface temperature. The net effect of the total cloud radiative effect is slightly positive but very small, indicating a very slight net warming effect of the clouds. The near cancellation of the cloud radiative effects is commonly observed above oceans. As the longwave and shortwave CRE act at different heights the effects on the atmospheric dynamics might still be substantial.

Some of the three-dimensional fields have been further investigated to acquire more insight in the structure of the cloud field. This revealed that the cloud field consisted of a large cloudy layer near the top of the troposphere and small clouds near 500 meters. In the intermediate layer vertically developed clouds with small diameters were observed, which is observed in other simulations as well (Islam et al., 1993; Robe and Emanuel, 1996). Some researchers such as Wing and Emanuel (2014) showed that radiative-convective equilibrium can exhibit strong clustering of clouds and water vapor, but this has not been observed in these simulations.

The three-dimensional fields show the existence of mesoscale structures in the domain. Analysis of the turbulent spectra using the ogive provided characteristic length scales. These length scales become larger near the top of the troposphere, which indicates that a large fraction of the variance resides at large length scales, indicating the existence of mesoscale structures. Closer inspection of the turbulent spectra revealed that the horizontal velocity and water field both have variance at large length scales at almost all heights. Although classically mesoscale structures were expected not to occur under uniform conditions, both simulations and observations have shown that these structures can exist (de Roode et al., 2004). Existence of mesoscale structures is not an inherent problem, but could cause problems with the statistics. Because of the large size of these mesoscale structures only a limited amount of these structures can exist in the domain simultaneously. The spectra however did show that extending the domain size from 24 kilometers to 72 kilometers was necessary to create these mesoscale structures. Additional extension of the domain might further improve the quality of the simulations.

7.2 Outlook

The results of this thesis have shown that DALES with the RRTMG radiation code can be used to simulate radiative-convective equilibrium, which required domains with heights of 30 kilometers. Showing that simulations of this scale are possible opens up new possibilities. Previous research showed that DALES is already well able to simulate stratocumulus, shallow cumulus and deep convection (Böing, 2014; van der Dussen, 2015). Therefore it could become possible to investigate large scale phenomena such as for example the Hadley circulation. These kinds of simulation do require a non-uniform surface temperature. The RRTMG code is already able to handle non-uniform surface temperatures and with some adjustments DALES can be adapted to incorporate this as well.

Performing full-fledged Hadley circulation simulations would require a very large domain, something which is currently not possible. In the Hadley circulation deep convection is responsible for transporting moisture to higher latitudes. To effectively simulate the Hadley circulation out-of-domain advection of moisture needs to be implemented. If this is not implemented large amounts of water can accumulate and large amounts of precipitation are necessary to close the hydrological cycle. To incorporate out-of-domain advection the periodic boundary conditions, as employed in nearly all LES models, might need to be modified. The periodic boundary conditions however are necessary for mass and momentum conservation. Alternatively large scale moisture and temperature tendencies could be used to account for the out-of-domain advection, which would require observational data, data from other large-scale simulations or parametrizations. Currently it might be more realistic and interesting to use a temperature gradient in the surface to investigate the effects of the temperature gradient on the resulting dynamics, cloud fields and energy balance. Note that because of the periodic boundary conditions the surface temperature field should be symmetric.

The RRTMG radiative transfer code, which calculates the upward and downward shortwave and longwave fluxes explicitly is likely an improvement over the radiative transfer codes of the previous DALES versions. The current implementation can be used for many kinds of simulations, but as the experiments of this thesis showed, some further modifications to the implementation might be necessary for the RRTMG code to become a part of the main DALES branch on GitHub. Ozone profiles inside the LES domain cannot currently be correctly specified by the user and ice clouds have not been implemented, but modifications to solve these problems have been made. The pressure in the LES domain, which acts as as substitute for density in the radiative transfer, is only initialized once and is not updated. Furthermore the initialization of the radiation does not occur at the start-up of the LES simulation, but after one timestep of the radiative transfer code. The first timestep of the radiative code the right radiative tendencies are not used. Considering the fact that the radiative transfer code is computationally quite expensive, radiative timesteps are often large. The initialization problems with the radiative tendencies could therefore result in substantial start-up problems. For this thesis project these issues have been resolved, but a more general solution is necessary.

The radiative-convective equilibrium simulations showed that the hybrid-WENO scheme, even when the threshold values were modified, was not able to entirely remove the oscillatory behavior in the prognostic variables near the top of the tropopause. Use of other advection schemes or grids might be a solution to solve this oscillatory behavior. Thorough investigation of this was out of scope for this thesis. Grid refinement might be an option as to reach this, but this would increase the required computation time. This could conflict with increasing the domain size which would require more computational resources as well. Increasing the domain size would enable development of more and larger mesoscale structures, as the spectra showed that in a relatively large amount of variance was located at large length scales. Longer simulations, instead of the 10 day simulations of thesis, could result in further development of the large scale phenomena. A balance needs to be found between grid, domain size and simulation time to use the computational resources efficiently.

The velocity variance spectra showed that a very large part of the variance was located at large length scales. Furthermore the horizontal velocities showed oscillatory behavior in time near the top of the troposphere and in the stratosphere. A likely explanation is the absence of damping forces at these altitudes. Gravity damping has been increased to reduce these oscillations in the stratosphere. Lowering the sponge layer further will distort the dynamics in the cloud layer. Although observations of stratospheric wind profiles show that high velocities can be reached in the stratosphere, problems can start in the LES simulations if the magnitude of the velocities reach too high values. One way to improve

the RCE simulations could be specifying geostrophic wind profiles. The current constant geostrophic wind profiles have been used for simplicity of the simulation.

Plots of the cloud field showed that clouds were vertically relatively well developed, a process also observed in other research such as Islam et al. (1993) and Robe and Emanuel (1996). The main force acting on these clouds in the buoyancy force. Resolved buoyancy is determined by the relative difference of the virtual potential temperature. In the formulation of the virtual potential temperature however ice has not been included. Latent heat of ice and water vapor in DALES differ by approximately 12%, which is quite substantial. This could be resolved by addition of an extra source or sink term associated with the phase change. Addition of ice to the virtual potential temperature formulation can therefore affect the buoyancy forces.

Additionally the liquid potential temperature θ_l in DALES is a simplification which does not incorporate ice. Research has shown that the use of this approximation without ice results in errors at low pressures (Bryan and Fritsch, 2004). For simulations with ice and high domains with low pressures it might be worthwhile to adapt the current approximation. The effects of ice for example could be included. Moreover the pressure dependencies in the liquid potential temperature formulations could be adapted as well.

Additionally the analysis of the surface fluxes showed that, even though the total water path was constant, the latent heat flux and precipitation flux were not equal, which would suggest an increasing total water path, which was not observed. Further inspection of the precipitation statistics could be done to try to solve this problem. A possible explanation might be the implementation of the anelastic approximation, which result in a density varying with height. Possibly the precipitation statistics are not adapted to work with this variable density.

Acknowledgments

Although completing this master thesis project is in the end an individual achievement, it would not have been possible without the help of others.

First of all I would like to thank my supervisor Stephan (de Roode) for his comments during the setup of the simulations, help with analysis of the results and his comments on the text of this thesis. Even though my experience with atmospheric physics and turbulence was very limited he was able to explain it to me concisely and his enthusiasm inspired me to further explore the world of atmospheric physics.

Many thanks to Erwin (de Beus) as well for all his computer-related help. The speed at which he can solve computer problems is amazing. When computer problems occurred Erwin usually solved the problem before I could actually finish my description of the problem.

Furthermore I would like to thank Steef Böing and Peter Blossey for their (online) help with questions regarding code and the schemes in DALES.

The students in Room 1.33.1 and the PhD students at the GRS department; Victor, Sander, René, Floris, Pim, Chiel, Sid, Vincent and Jerome were great discussion partners in both useful and less useful discussions about DALES, thesis work, coffee (quality), leisure time, cycling and the other important things in life. I really enjoyed our discussions and I owe the great time largely to them and the staff of the Atmospheric Physics group.

Additionally I would like to thank the staff of the Atmospheric Physics group for arranging computation time on the supercomputer facilities of SURFsara.

Furthermore I would like to thank my girlfriend, friends, family and colleagues for their interest in my project, their time and their support. Especially I would like to thank Tom and Frans-Willem for the regular beers and dinners and Rahul and Roel for the numerous coffee breaks.

Laurens Wester
November 12, 2015

Appendices

Chapter A

Previous Research

A.1 Manabe and Strickler (1964)

Manabe and Strickler were among the first to investigate the radiative-convective equilibrium using a 1-dimensional column model. Essentially Manabe and Strickler calculated the situation in radiative equilibrium. To reach radiative-convective equilibrium they prescribed a fixed lapse rate in the convective layers of the troposphere. Part of the research of this thesis has been inspired by their work. Similar to their work this thesis also investigated radiative equilibrium. In figures A.1 and A.2 the results of their 1964 paper can be found. Figure A.1 shows the temperature profiles in equilibrium for radiative equilibrium and for radiative equilibrium with convective adjustments. These convective adjustments consisted of prescribing a fixed lapse rates in the convective zones. These images have also been printed in other parts of this thesis but are printed here as well for a better overview.

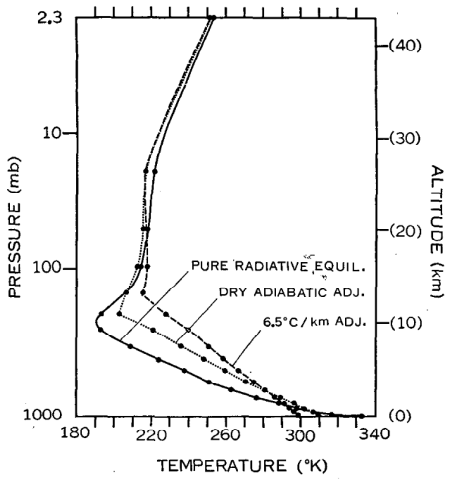

Figure A.1: Manabe and Strickler (1964): Radiative Equilibrium with a convective adjustment. Manabe and Strickler calculated radiative equilibrium of the atmosphere and compensated for convection by prescribing a fixed lapse rate in the convective layer. Image source: figure 4, Manabe and Strickler (1964).

Figure A.2 shows the atmosphere in radiative equilibrium. In these calculations gasses have been removed from the atmosphere. The resulting temperature profiles have been plotted.

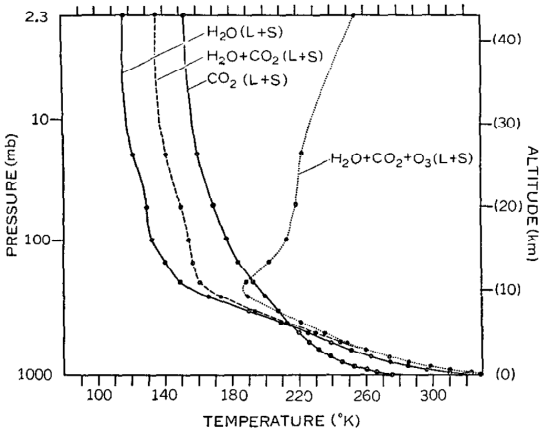

Figure A.2: Manabe and Strickler (1964): Effect of atmospheric composition. In these simulations the effects of adding and removing three gasses of the atmosphere in radiative equilibrium have been investigated. These three gasses (CO_2, O_3 and H_2O) are good absorbers of longwave or shortwave radiation. Image source: figure 6a, Manabe and Strickler (1964).

A.2 Held et al. (1993) and Sui et al. (1994)

Both of these papers investigated radiative convective equilibrium with a two-dimensional cloud-resolving model. Their simulations used a coarser resolution. The results from this thesis are compared to their results. Therefore some of their results are plotted in this section.

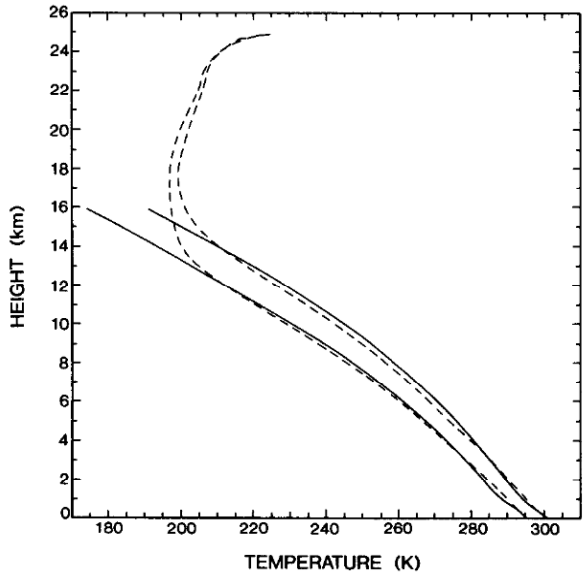

Figure A.3: Held et al. (1993); Temperature in Radiative Convective Equilibrium. These two simulations used a two-dimensional cloud-resolving model to determine the effect of the surface temperature on the atmospheric temperature. The dashed lines are simulations results of 25°C and 30°C. The solid lines are adiabats. Image source: figure 10, Held et al. (1993).

The temperature profiles from the results of Held et al. closely follow the moist adiabats. The inversion moves upwards as the surface temperature increases. Above this inversion the temperature remains relatively constant with height until 24 kilometers where it starts increasing with height.

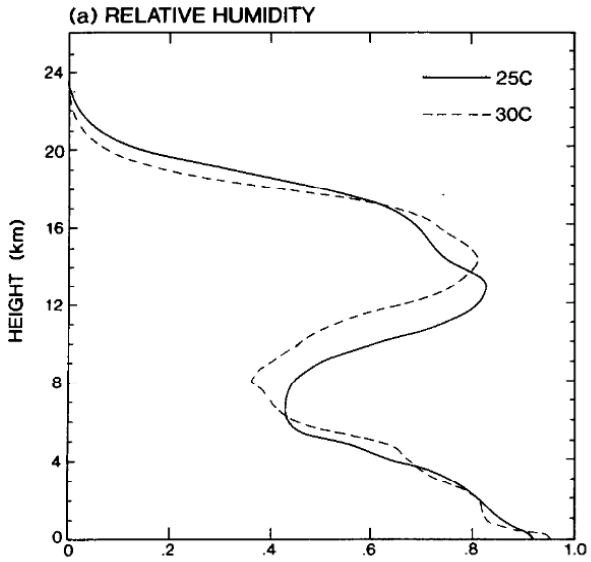

Figure A.4: Held et al. (1993): Relative Humidity. The relative humidity for the results of the 25°C (solid) and 30°C (dashed). The relative humidity decreases with height up to a point, after which the relative humidity increases with height. This point moves upward if the surface temperature is increased. Eventually the relative humidity reaches approximately 0% at 20 kilometers. Image source: figure 12a, Held et al. (1993).

The results from Held et al. (1993) match observational data in the troposphere quite well unlike the results of Sui et al. (1994). Observational data and the results of Sui et al. can be found in figure A.5.

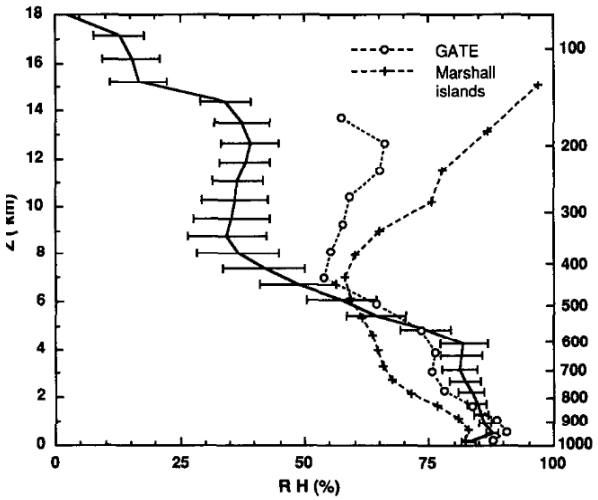

Figure A.5: Sui et al. (1994); Relative Humidity. The relative humidity of the simulations results (solid line) decreases with height and moves to 0% at 18 kilometers. These results are not consistent with measurements (dashed lines). The results of Held et al. (1993) more closely resemble the observational data. Image source: figure 9, Sui et al. (1994).

A.3 Islam et al. (1993) and Robe and Emanuel (1996)

The simulations of Islam et al. (1993) and Robe and Emanuel (1996) were both performed with three-dimensional cloud resolving models. Therefore it is interesting to compare the results of these papers to the results of this thesis. Robe and Emanuel did not calculate the radiation explicitly, but prescribed cooling rates to determine the effect on the atmosphere in equilibrium. R21 has a radiative cooling rate of $2.14 K day^{-1}$ and R54 $5.35 K day^{-1}$. The relative humidity and cloud fields excerpts are plotted in the next three figures.

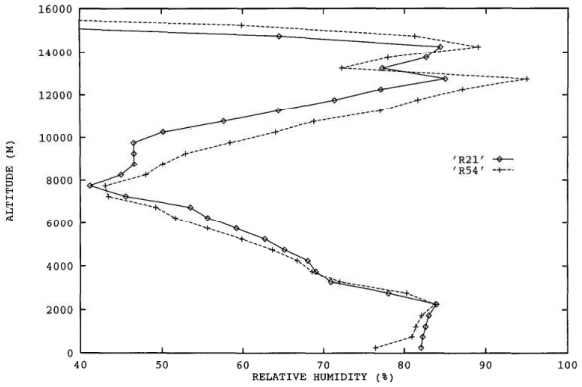

Figure A.6: Robe and Emanuel (1996): Relative Humidity. The relative humidity of two simulations with different cooling rates has been plotted. R21 has a radiative cooling rate of $2.14 K day^{-1}$ and R54 $5.35 K day^{-1}$. After an initial decrease in relative humidity after 2 kilometers the relative humidity decreases again up to 8 kilometers after which the relative humidity increases again. Image source: figure 5, Robe and Emanuel (1996).

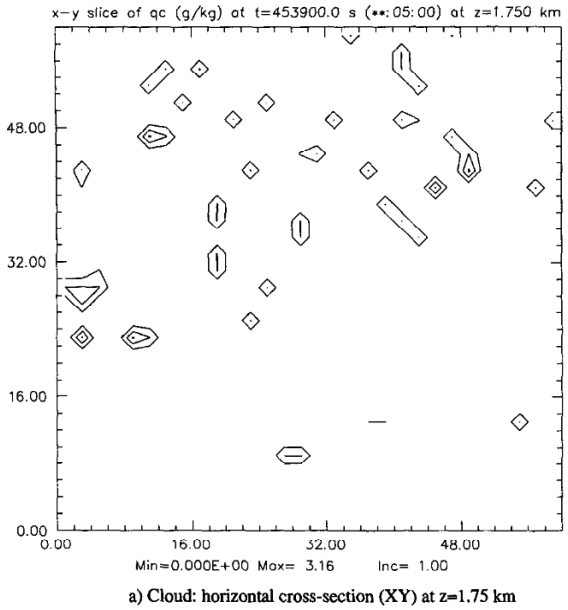

Figure A.7: Robe and Emanuel (1996): Cloud Fraction Horizontal. Clouds generally have a small diameter of less than 5 kilometers. Image source:figure 1a, Robe and Emanuel (1996).

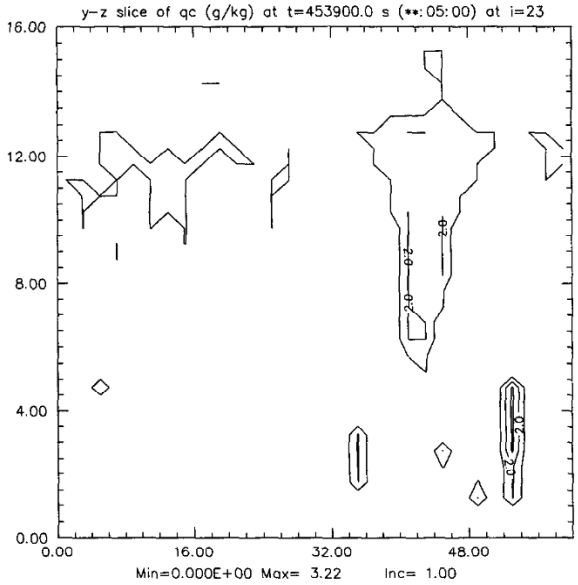

Figure A.8: Robe and Emanuel (1996): Cloud Fraction Vertical. Some clouds with relatively small diameters (2 kilometers) and extended vertical development (4 kilometers) are observed. The top of the troposphere has a higher cloud fraction, but is not entirely cloudy. Image source: figure 1b, Robe and Emanuel (1996).

Islam et al. (1993) used a three-dimensional model as well and computed the cloud fields for their simulations.

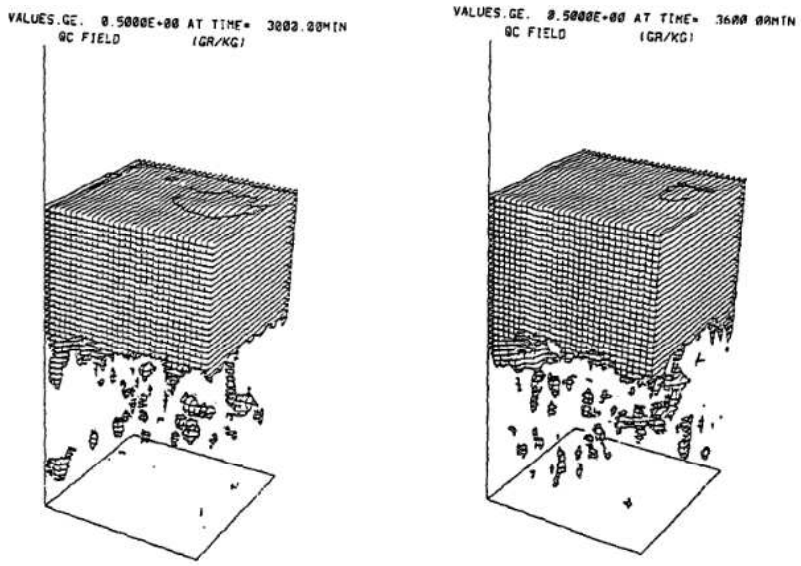

Figure A.9: Islam et al. (1993): Cloud Field. Cloud fields have been plotted for 50 hours (left) and 60 hours (right) of simulation. The top of the troposphere is located at 14 kilometers and below the top the domain is almost entirely cloudy. In the underlying area some smaller clouds are observed. Image source: figure 1e, Islam et al. (1993).

Chapter B

LES Modifications

B.1 Ice Clouds

As explained previously ice clouds were added to DALES for this project. This has been implemented using the following Fortran 90 code in the module "modradrrtmg.f90". In the subroutine *setupSlices-FromProfiles* lines 6 to 10 have been added to calculate the ice-liquid partitioning. This method is similar to the method used in the thermodynamics and microphysics. The "l_ice" is a switch that can be used to choose between simulations with and without ice clouds. The ice-liquid partitioning is applied in line 19 and 20.

```
1       do i=2,i1
2       do k=1,kmax
3           im = i-1
4           tabs_slice(im,k) = thl0(i,j,k) * exnf(k) &
5                            + (rlv / cp) * ql0(i,j,k)
6           if (l_ice) then
7           il_slice(im,k) = max(0.,min(1.,(tabs_slice(im,k)-tdn)/(tup-tdn)))
8           else
9           il_slice(im,k) = 1.
10          end if
11      enddo
12      enddo
13
14      do i=2,i1
15      im=i-1
16      do k=1,kmax
17
18         qv_slice  (im,k) = qt0(i,j,k) - ql0(i,j,k)
19         qcl_slice (im,k) = ql0(i,j,k)*il_slice(im,k)
20         qci_slice (im,k) = ql0(i,j,k)*(1.-il_slice(im,k))
21         o3_slice  (im,k) = o3snd(npatch_start)
22         tg_slice  (im)   = sst
23
24         h2ovmr    (im,k) = mwdry/mwh2o * qv_slice(im, k)
25 !
26         layerT    (im,k) = tabs_slice(im,k)
27         layerP    (im,k) = presf_input(k)
28      enddo
29      enddo
```

In the same subroutine the effective radius of the liquid particles is calculated. This is in line 1 to 17 in the snippet of code below. In this same loop one has to insert the ice cloud code (line 19 to 30)[1]. Line 25 to 30 are used to round down the effective radius of particles bigger than $60\mu m$ to $60\mu m$ and the round up the effective radius of particles smaller than $30\mu m$ to $30\mu m$. This way all effective radii are between 30 and 60 μm.

```
1       do i=1,imax
2         do k=1,kradmax
3           cloudFrac(i,k) = 0.
4           liquidRe (i,k) = 0.
5           iceRe    (i,k) = 0.
6           if (LWP_slice(i,k).gt.0.) then
7             cloudFrac(i,k) = 1.
8             liquidRe(i, k) = 1.e6*( 3.*( 1.e-3*LWP_slice(i,k)/layerMass(i,k) ) &
9                                /(4.*pi*Nc_0*rho_liq) )**(1./3.) * exp(log(sig_g)**2 )
10
11        if ( (LWP_slice(i,k).gt.0.) .AND. (liquidRe(i,k).lt.2.5)) then
12          liquidRe(i,k) = 2.5
13        endif
14        if ( (LWP_slice(i,k).gt.0.) .AND. (liquidRe(i,k).gt.60.)) then
15          liquidRe(i,k) = 60.
16        endif
17          endif
18
19      if (IWP_slice(i,k).gt.0.) then
20      cloudFrac(i,k) = 1.
21            iceRe(i, k) = 326.3 + 12.42*(layerT(i,k)-273.15)+0.197*((layerT(i,k)-273.15))**2 &
22            +0.0012*((layerT(i,k)-273.15))**3
23
24            !limit the radii between 30um and 60um
25        if ( (IWP_slice(i,k).gt.0.) .AND. (iceRe(i,k).lt.30.)) then
26          iceRe(i,k) = 30.
27        endif
28        if ( (IWP_slice(i,k).gt.0.) .AND. (iceRe(i,k).gt.60.)) then
29          iceRe(i,k) = 60.
30        endif
31
32          endif
33
34        enddo
35      enddo
```

The relevant variables need to be loaded from their respective modules.

[1] In the near future this modification can be found on GitHub. See: https://github.com/dalesteam/dales.git

B.2 WENO scheme

The WENO scheme has been slightly modify to reduce oscillatory behavior at higher altitudes. To do this the calculation of the smoothness parameter λ has been altered in the module "advec_hybrid.f90". In the subroutines *interp_x*, *interp_y* and *interp_z* line 13 has to be replaced by the code from line 14 and *tmpeps* needs to replace the original *lambda* in the subsequent line.

```
1   do k=1,k1
2     do j=2,j2
3       do i=2,i2
4       ip2=i+2;ip1=i+1;im1=i-1;im2=i-2;im3=i-3
5         ! Calculate the smoothness for each stencil in an upwind configuration
6         if (u0(i,j,k)>=0.) then
7           gam(:) = (pin(im1:ip1,j,k)-pin(im2:i,j,k))**2 + &
8                    (pin(im2:i,j,k)-pin(im3:im1,j,k))**2
9         else
10          gam(:) = (pin(i:ip2,j,k)-pin(im1:ip1,j,k))**2 + &
11                   (pin(im1:ip1,j,k)-pin(im2:i,j,k))**2
12        end if
13        ! lambda = maxval(gam)/(minval(gam)+eps_hybrid) !replaced by Blosseys suggestion
14           tmpeps = tiny(1.) + 1.e-14*(gam(1)+gam(2)+gam(3))
15           lambda = maxval(gam)/(minval(gam)+tmpeps)
16        ! Select which interpolation schemes should be used based on smoothness metric lambda
17        if (lambda > lambda_crit) then
18 !         if (abs(eps_hybrid-1.e-14)<1e-18) smoothx(k) = smoothx(k) + rdt
19          pout(i,j,k) = ip_weno(pin(im3:ip2,j,k),u0(i,j,k)>=0.)
20        else
21          pout(i,j,k) = ip_5th (pin(im3:ip2,j,k),sign(1.,u0(i,j,k)))
22        end if
23      end do
24    end do
25  end do
```

B.3 Ozone Interpolation

In the original DALES code it was not possible to specify a user-specified ozone content inside the LES domain. The ozone content inside the LES domain was set to the value of the lowest level of the backrad domain. Therefore the ozone volume mixing ratio was equal to the first level above the LES domain. If the top of the LES domain is in the stratosphere, the amount of ozone in the atmosphere is overestimated if this procedure is used.

In the "modradrrtmg.f90" the subroutine *setupSlicesFromProfiles* requires a small modification. The RRTMG radiative code uses pressure-based coordinates whereas the LES domain uses height-based coordinates. Pressure in the LES domain is calculated, hence the pressure at every height is known. To specify the ozone content inside the LES domain the ozone needs to be interpolated as a function of this pressure.

The logarithm of the pressure is approximately a linear function of height and hence the logarithm is used for linear interpolation (Taylor, 2005). Using linear interpolation of the pressure might result in biased estimated of the ozone content if the amount of pressure levels is limited. Note that the sounding level pressures are in reverse order. Should the LES domain contain pressure higher than the pressures in the sounding file, the ozone content is set equal to the ozone content of the highest pressures in the sounding file.

```
1       do i=2,i1
2       im=i-1
3       do ks = 2, (npatch_start+1)
4         if ((presf_input(k) .le. psnd(ks-1)) .AND. (presf_input(k) .ge. psnd(ks))) then
5         o3_slice  (im,k) = o3snd(ks-1)+((o3snd(ks)-o3snd(ks-1)) &
6         /(log(psnd(ks))-log(psnd(ks-1))))*(log(presf_input(k))-log(psnd(ks-1)))
7
8           elseif (presf_input(k) .ge. psnd(1)) then
```

```
9           o3_slice(im,k) = o3snd(1)
10          end if
11        enddo
12
13        enddo
```

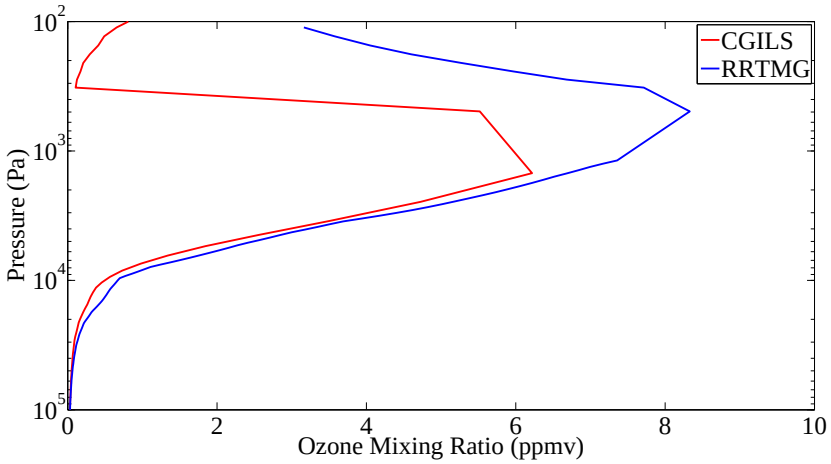

Figure B.1: CGILS and RRTMG ozone profiles. At the pressures occurring in the LES domain the difference in ozone concentration is small. The top of the LES domain at 30 kilometers is located at a pressure level of approximately $10^3 Pa$.

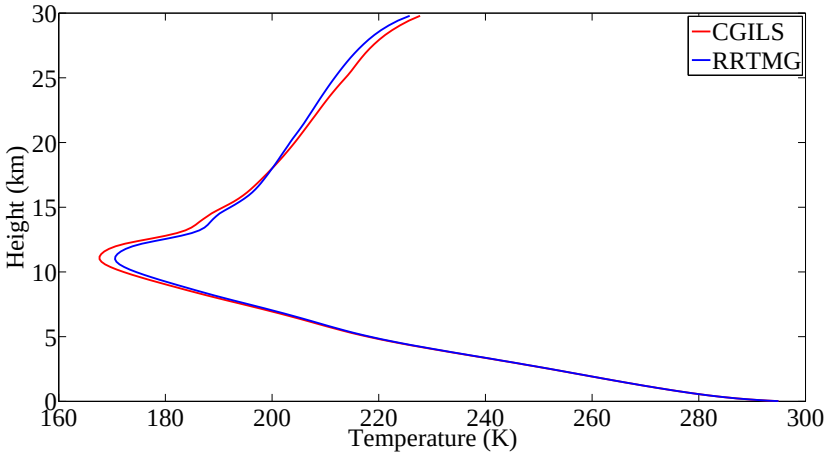

Figure B.2: The effect on the temperature of a radiation-driven simulation with a fixed surface potential temperature of 295K. The CGILS S6 profile (red) and the default profiles from the RRTMG code (blue) have been used (see image B.1). This results in small differences in temperature in the stratosphere and upper troposphere.

Chapter C

Derivations

C.1 Lapse Rate

It is assumed that air parcels rise adiabatically, therefore the amount of heat exchange (Q) with the environment is zero. The first law of thermodynamics hence stipulates that the change in internal energy (ΔU) should equal the work W done,

$$\Delta U = Q - W. \tag{C.1}$$

As the air parcel rises it expands performing expansion work. The internal energy for dry air is a function of temperature,

$$W = -pdV, \tag{C.2}$$

$$\Delta U = mc_v dT, \tag{C.3}$$

$$mc_v dT + pdV = 0. \tag{C.4}$$

Dividing by the mass gives the following equation,

$$mc_v dT + pdV = c_v dT + \frac{1}{m} pdV = 0. \tag{C.5}$$

For adiabatic processes the following steps can be used,

$$pV^\gamma = constant, \tag{C.6}$$

$$pdV = -V\frac{dp}{\gamma}, \tag{C.7}$$

$$c_v dT - \frac{V}{m}\frac{dp}{\gamma} = 0. \tag{C.8}$$

The state in the atmosphere is usually quite close to hydrostatic equilibrium. In hydrostatic equilibrium the pressure gradient force balances the gravity force,

$$dp = -\rho g dz, \tag{C.9}$$

$$c_v dT + \frac{V}{m}\frac{\rho g dz}{\gamma} = 0. \tag{C.10}$$

Using the information that $\gamma = c_p/c_v$ and $\rho = m/V$ and rewriting gives,

$$\frac{dT}{dz} = -\frac{V}{m}\frac{\rho g}{c_v \gamma} = -\frac{g}{c_p}. \tag{C.11}$$

The gravitational constant is $9.81 m/s^2$ and the heat capacity of air is $1004 Jkg^{-1}K$. This results in the dry adiabatic lapse rate,

$$\frac{dT}{dz} = -\frac{g}{c_p} \approx 9.8 K/km. \tag{C.12}$$

It is often convenient to use potential temperatures instead of absolute temperatures because potential temperatures are conserved quantities under certain circumstances,

$$T = \theta \left(\frac{p}{p_0}\right)^{\frac{R_d}{c_p}}. \tag{C.13}$$

Substituting this in the equation for the dry lapse rate gives,

$$\frac{dT}{dz} = -\Gamma_d = \frac{d\theta}{dz}\left(\frac{p}{p_0}\right)^{\frac{R_d}{c_p}} + \frac{\theta R_d}{p c_p}\left(\frac{p}{p_0}\right)^{\frac{R_d}{c_p}} \frac{dp}{dz} = -\frac{g}{c_p}. \tag{C.14}$$

Hydrostatic equilibrium is used to get rid of the pressure derivative, the temperature T is substituted back,

$$\frac{d\theta}{dz}\left(\frac{p}{p_0}\right)^{\frac{R_d}{c_p}} - \frac{\rho g R_d}{p c_p} T = -\frac{g}{c_p}. \tag{C.15}$$

The ideal gas law can be applied to this situation,

$$pV = m R_d T, \tag{C.16}$$

$$\frac{d\theta}{dz}\left(\frac{p}{p_0}\right)^{\frac{R_d}{c_p}} - \frac{\rho g V}{m c_p} = -\frac{g}{c_p}. \tag{C.17}$$

The fraction V/m is the density, so this equation simplifies to,

$$\frac{d\theta}{dz}\left(\frac{p}{p_0}\right)^{\frac{R_d}{c_p}} - \frac{g}{c_p} = -\frac{g}{c_p}, \tag{C.18}$$

$$\frac{d\theta}{dz} = 0. \tag{C.19}$$

This means that the potential temperature θ is constant with height if the temperature is following the dry adiabatic lapse rate. An alternative derivation can be made by assuming that liquid potential temperature θ_l (no energy exchange) and total water mixing ratio q_t (no moisture exchange) are constant,

$$\theta = \theta_l + \frac{L}{c_p \Pi} q_l. \tag{C.20}$$

For dry air q_t is zero and hence q_l is zero as well. Equation C.19 follows from this as well. Inclusion of moisture makes it somewhat more complicated even under unsaturated conditions. Moist air is lighter than dry air at the same pressure and temperature. To add this process to the calculations often the virtual temperature and the virtual potential temperature are used. Many formulas for dry situations can be used for unsaturated situations as well if the virtual equivalents are used,

$$T_v = T\left(1 + \left(\frac{R_v}{R_d} - 1\right) q_t - \frac{R_v}{R_d} q_l\right), \tag{C.21}$$

$$\theta_v = \theta\left(1 + \left(\frac{R_v}{R_d} - 1\right) q_t - \frac{R_v}{R_d} q_l\right). \tag{C.22}$$

Under unsaturated conditions q_l is always zero in formula C.22. As θ_l and q_t are constant for adiabatic parcels. Parcels that are unsaturated therefore follow the unsaturated lapse rate as well and hence equation C.23 applies to unsaturated cases with moisture as well. If θ_v increases with height the situation is stable whereas the situation is unstable if θ_v decreases with height,

$$\frac{d\theta_v}{dz} = 0. \tag{C.23}$$

If an unsaturated parcel rises the pressure will decrease with height and the parcel will expand which requires expansion work, reducing the temperature of the parcel. This reduces the maximum possible amount of water the parcel can contain (q_{sat}). As the total water content q_t remains constant part of the water can condensate if the total water content becomes larger than the saturated vapor content. This will result in release of latent heat, the parcel will from this point on follow the saturated adiabatic lapse rate. Calculation of the saturated adiabatic lapse rate is somewhat less straightforward. For a certain pressure profile the following procedure can be used. An adiabatic parcel has constant θ_l and constant q_t. Therefore one has to start with creating an air parcel at the ground surface, with $q_t = q_{sat}$. As the parcel is not saturated q_l is zero and the virtual potential temperature follows from equation C.24,

$$\theta_v = \left(\theta_l + \frac{L}{c_p \Pi} q_l\right)\left(1 + \left(\frac{R_v}{R_d} - 1\right) q_t - \frac{R_v}{R_d} q_l\right). \tag{C.24}$$

This parcel is lifted upwards, reducing the pressure, which reduces the saturated vapor content (q_{sat}). This increases the amount of liquid water q_l changing the temperature (see equation C.25). The saturated vapor content however depends on the temperature as well as can be seen from equation C.27, in this formula e_{sat} is the saturated vapor pressure. The saturated vapor pressure is calculated using Tetens's formula C.26 in which e_{sat0} is $610.78Pa$, A is 17.27, B is $35.86K$ and T_{melt} is $273.16K$,

$$T = \theta_l \left(\frac{p}{p_0}\right)^{\frac{R_d}{c_p}} + \frac{L}{c_p} q_l, \tag{C.25}$$

$$e_{sat} = e_{sat0} \exp\left(\frac{A\,(T - T_{melt})}{T - B}\right), \tag{C.26}$$

$$q_{sat} = \frac{R_d e_{sat}}{R_v \left(p - \left(1 - \frac{R_d}{R_v} e_{sat}\right)\right)}. \tag{C.27}$$

Because the saturated vapor content and temperature depends on each other through the liquid water content this problem has to be solved iteratively. The Newton-Raphson method can be used to calculate the temperature and the saturated vapor content. The saturated vapor content can be used to calculate the liquid water content q_l. As θ_l and q_t are constant the virtual potential temperature of the saturated adiabatic curve (θ_v^S) follows directly from equation C.24. This process has to be done for all height levels with their associated pressures. This enables calculation of the saturated adiabatic lapse rate. The virtual potential temperature along the saturated adiabatic curve increases with height, hence the saturated adiabatic lapse rate is positive. Under conditionally unstable conditions the virtual potential temperature increases with height but at a smaller rate than the saturated adiabatic virtual potential temperature.

$\frac{d\theta_v^S}{dz} < \frac{d\theta_v}{dz}$	Absolutely Stable
$0 < \frac{d\theta_v}{dz} < \frac{d\theta_v^S}{dz}$	Conditionally Unstable
$\frac{d\theta_v}{dz} < 0$	Absolutely Unstable

C.2 Momentum Equation

Since the density is not constant in this case the incompressible Navier-Stokes equations cannot be used. Instead the anelastic approximation has been implemented in the momentum equations by Böing (2014). The density is a function of height x_3 only which enables writing the advection term in equation 2.7 as follows,

$$u_j \frac{\partial u_i}{\partial x_j} = \frac{1}{\rho_0} \frac{\partial \rho_0 u_i u_j}{\partial x_j} - \frac{u_i}{\rho_0} \frac{\partial \rho_0 u_j}{\partial x_j}. \tag{C.28}$$

The density ρ_0 is independent of time and hence the first term in the anelastic continuity equation C.29 is zero,

$$\frac{\partial \rho_0}{\partial t} + \frac{\partial \rho_0 u_j}{\partial x_j} = 0. \tag{C.29}$$

This means that the second term on the right hand side in equation C.28 is zero because this is equal to the anelastic continuity equation with time-independent density. This can be used to simplify equation C.28,

$$u_j \frac{\partial u_i}{\partial x_j} = \frac{1}{\rho_0} \frac{\partial \rho_0 u_i u_j}{\partial x_j}. \tag{C.30}$$

As density in the anelastic approximation varies only in the vertical direction this equation could in principle be simplified further to equation C.31,

$$u_j \frac{\partial u_i}{\partial x_j} = \frac{1}{\rho_0} \frac{\partial u_i u_j}{\partial x_j} + \frac{u_i u_3}{\rho_0} \frac{\partial \rho_0}{\partial x_3}. \tag{C.31}$$

Substituting this into the momentum equation produces the following result,

$$\frac{\partial u_i}{\partial t} = -\frac{1}{\rho_0} \frac{\partial \rho_0 u_i u_j}{\partial x_j} - \frac{1}{\rho} \frac{\partial p}{\partial x_i} - 2\epsilon_{ijk}\Omega_j u_k - g\delta_{i3} + F_{ijk}. \tag{C.32}$$

The ideal gas law, an equation of state, generally holds for dry air, for moist air it is somewhat more complicated as the gas constant changes with moisture content. Therefore the virtual temperature T_v has to be used instead of the absolute temperature T. In this formula R_d the the gas constant for dry air. In this equation α is the specific volume,

$$p = \rho R_d T_v = \frac{R_d T_v}{\alpha}. \tag{C.33}$$

As described by Böing (2014) the environmental state is required to be in hydrostatic equilibrium. The environmental state in DALES is the slab-averaged state,

$$\alpha_e \frac{\partial p_e}{\partial x_i} = -g\delta_{i3}. \tag{C.34}$$

The pressure p gradient and specific volume α of the local state are expanded in terms of perturbations relative to the environmental state. Note that the local state does not needs be in hydrostatic equilibrium. Products of perturbations the total pressure gradient are neglected and several approximations are made as can be found in the appendix of Böing (2014), which leads to the following equation,

$$\alpha \frac{\partial p}{\partial x_i} \approx -g\delta_{i3} - g\delta_{i3} \frac{\alpha\left(p_e, T_v\right) - \alpha_e}{\alpha_e} + \frac{\partial}{\partial x_i}\left(\alpha_e \delta p\right). \tag{C.35}$$

Changing some of the specific volumes back to densities to remain consistency with the original equation 2.7 produces the following equation,

$$\frac{1}{\rho} \frac{\partial p}{\partial x_i} \approx -g\delta_{i3} - g\delta_{i3} \frac{\alpha\left(p_e, T_v\right) - \alpha_e}{\alpha_e} + \frac{\partial}{\partial x_i}\left(\frac{\delta p}{\rho_e}\right). \tag{C.36}$$

Substituting this into equation C.32 produces equation C.37,

$$\frac{\partial u_i}{\partial t} = -\frac{1}{\rho_0}\frac{\partial \rho_0 u_i u_j}{\partial x_j} + g\delta_{i3} + g\delta_{i3}\frac{\alpha\left(p_e, T_v\right) - \alpha_e}{\alpha_e} - \frac{\partial}{\partial x_i}\left(\frac{\delta p}{\rho_e}\right) - 2\epsilon_{ijk}\Omega_j u_k - g\delta_{i3} + F_{ijk}. \tag{C.37}$$

Simplifying the equation provides the following result,

$$\frac{\partial u_i}{\partial t} = -\frac{1}{\rho_0}\frac{\partial \rho_0 u_i u_j}{\partial x_j} - \frac{\partial}{\partial x_i}\left(\frac{\delta p}{\rho_e}\right) + g\delta_{i3}\frac{\alpha\left(p_e, T_v\right) - \alpha_e}{\alpha_e} - 2\epsilon_{ijk}\Omega_j u_k + F_{ijk}. \tag{C.38}$$

The third term on the right hand side is the buoyancy force. The buoyancy can be conveniently rewritten using the equation of state C.39, derived from equation C.33,

$$\alpha = \frac{R_d T_v}{p}, \tag{C.39}$$

$$g\delta_{i3}\frac{\alpha\left(p_e, T_v\right) - \alpha_e}{\alpha_e} = g\delta_{i3}\frac{\frac{R_d T_v}{p_e} - \frac{R_d T_{v,e}}{p_e}}{\frac{R_d T_{v,e}}{p_e}} = g\delta_{i3}\frac{T_v - T_{v,e}}{T_{v,e}}. \tag{C.40}$$

The virtual temperature T_v is not calculated in DALES but the virtual potential temperature θ_v is. Therefore the virtual temperature is converted to the virtual potential temperature using the Exner function,

$$\theta_v = T_v\left(\frac{p}{p_0}\right)^{R_d/c_p}. \tag{C.41}$$

As the both T_v and $T_{v,e}$ are at pressure p_e the Exner functions cancel out,

$$g\delta_{i3}\frac{T_v - T_{v,e}}{T_{v,e}} = g\delta_{i3}\frac{\theta_v - \theta_{v,e}}{\theta_{v,e}}. \tag{C.42}$$

Substituting this results in the momentum equation and including the drag from precipitation provides equation C.43 in which viscous forces have been neglected, as is often assumed in atmospheric physics,

$$\frac{\partial u_i}{\partial t} = -\frac{1}{\rho_0}\frac{\partial \rho_0 u_i u_j}{\partial x_j} - \frac{\partial}{\partial x_i}\left(\frac{\delta p}{\rho_e}\right) + g\delta_{i3}\left(\frac{\theta_v - \theta_{v,e}}{\theta_{v,e}} - q_r\right) - 2\epsilon_{ijk}\Omega_j u_k. \tag{C.43}$$

C.3 Zenith Angle

The amount of instantaneous incoming radiation is described by formula C.44 in which S_0 is the solar constant, R_0 is the earth-sun distance, R_E is the average earth-sun distance in a year and θ_s is the solar zenith angle,

$$Q = S_0 \frac{{R_0}^2}{{R_E}^2} \cos(\theta_s). \tag{C.44}$$

The zenith angle depends on latitude ϕ, declination δ and hour angle h,

$$\cos(\theta_s) = \sin(\phi)\sin(\delta) + \cos(\phi)\cos(\delta)\cos(h). \tag{C.45}$$

Throughout the day the declination angle δ is assumed to be constant, the ϵ_{earth} angle is approximately -23.45° and N is the day of the year,

$$\delta = \arcsin(\sin(\epsilon_{earth})\sin(4.88 + 0.172N)). \tag{C.46}$$

To get the total amount of incoming radiation formula C.44 has to be integrated over the entire day; from an hour angle of $-\pi$ to an hour angle of π. After sunset and before sunrise however the amount of solar radiation is 0, so formula C.45 is only valid between sunrise and sunset. Sunrise and sunset occur at hour angles of $-h_0$ and h_0 respectively which can be calculated using equation C.47,

$$\cos(h_0) = -\tan(\phi)\tan(\delta). \tag{C.47}$$

The average amount of incoming radiation on a day can be calculated using equation C.48,

$$Q_{av} = \frac{1}{2\pi} \int_{-\pi}^{\pi} S_0 \frac{{R_0}^2}{{R_E}^2} \cos(\theta_s) dh. \tag{C.48}$$

By substituting equation C.45 in C.48 the integral can be calculated,

$$Q_{av} = \frac{1}{2\pi} S_0 \frac{{R_0}^2}{{R_E}^2} \int_{-h_0}^{h_0} \left(\sin(\phi)\sin(\delta) + \cos(\phi)\cos(\delta)\cos(h)\right) dh, \tag{C.49}$$

$$Q_{av} = \frac{1}{2\pi} S_0 \frac{{R_0}^2}{{R_E}^2} \left(h\sin(\phi)\sin(\delta) + \cos(\phi)\cos(\delta)\sin(h)\right) |_{-h_0}^{h_0}, \tag{C.50}$$

$$Q_{av} = \frac{1}{\pi} S_0 \frac{{R_0}^2}{{R_E}^2} \left(h_0\sin(\phi)\sin(\delta) + \cos(\phi)\cos(\delta)\sin(h_0)\right). \tag{C.51}$$

Aside from this the insolation-averaged cosine of the zenith angle should be calculated. This is done by multiplying the insolation Q by the cosine of the zenith angle and integrating the product. This should be divided by the total amount of insolation,

$$\overline{\mu_0} = \overline{\cos(\theta_s)} = \frac{\int_{-\pi}^{\pi} Q(\theta_s)\cos(\theta_s) dh}{\int_{-\pi}^{\pi} Q(\theta_s) dh}. \tag{C.52}$$

Solar insolation only reaches the earth between sunrise and sunset, so the integrals have to be executed from $-h_0$ to h_0. Constants can be taken outside the integral,

$$\overline{\mu_0} = \frac{\int_{-h_0}^{h_0} S_0 \frac{{R_0}^2}{{R_E}^2} \cos(\theta_s)\cos(\theta_s) dh}{\int_{-h_0}^{h_0} S_0 \frac{{R_0}^2}{{R_E}^2} \cos(\theta_s) dh}, \tag{C.53}$$

$$\overline{\mu_0} = \frac{\int_{-h_0}^{h_0} S_0 \frac{{R_0}^2}{{R_E}^2} \left(\sin(\phi)\sin(\delta) + \cos(\phi)\cos(\delta)\cos(h)\right)^2 dh}{\int_{-h_0}^{h_0} S_0 \frac{{R_0}^2}{{R_E}^2} \left(\sin(\phi)\sin(\delta) + \cos(\phi)\cos(\delta)\cos(h)\right) dh}, \tag{C.54}$$

$$\overline{\mu_0} = \frac{\int_{-h_0}^{h_0} \left((\sin(\phi)\sin(\delta))^2 + (\cos(\phi)\cos(\delta)\cos(h))^2 + 2\sin(\phi)\sin(\delta)\cos(\phi)\cos(\delta)\cos(h) \right) dh}{2\left(h_0 \sin(\phi)\sin(\delta) + \cos(\phi)\cos(\delta)\cos(h_0)\right)}, \quad \text{(C.55)}$$

$$\overline{\mu_0} = \frac{2h_0 \left(\sin(\phi)\sin(\delta)\right)^2 + 4\left(\sin(\phi)\sin(\delta)\cos(\phi)\cos(\delta)\sin(h_0)\right) + \left(\cos(\phi)\cos(\delta)\right)^2 \int_{-h_0}^{h_0} \left(\cos(h)\right)^2 dh}{2\left(h_0 \sin(\phi)\sin(\delta) + \cos(\phi)\cos(\delta)\cos(h_0)\right)}, \quad \text{(C.56)}$$

$$\overline{\mu_0} = \frac{2h_0 \left(\sin(\phi)\sin(\delta)\right)^2 + 4\left(\sin(\phi)\sin(\delta)\cos(\phi)\cos(\delta)\sin(h_0)\right) + \left(\cos(\phi)\cos(\delta)\right)^2 \left(\frac{h}{2} + \frac{1}{4}\sin(2h)\right)\Big|_{-h_0}^{h_0}}{2\left(h_0 \sin(\phi)\sin(\delta) + \cos(\phi)\cos(\delta)\cos(h_0)\right)}, \quad \text{(C.57)}$$

$$\overline{\mu_0} = \frac{2h_0 \left(\sin(\phi)\sin(\delta)\right)^2 + 4\left(\sin(\phi)\sin(\delta)\cos(\phi)\cos(\delta)\sin(h_0)\right) + \left(h_0 + \frac{1}{2}\sin(2h_0)\right)\left(\cos(\phi)\cos(\delta)\right)^2}{2\left(h_0 \sin(\phi)\sin(\delta) + \cos(\phi)\cos(\delta)\cos(h_0)\right)}. \quad \text{(C.58)}$$

All variables in formula C.58 are known and hence this formula can be used to get a value for the insolation-averaged cosine of the zenith angle. Multiplied by the effective solar constant S_0^* this should provide the same daily averaged intensity. The associated effective solar constant can hence be calculated using formula C.60,

$$S_0^* \overline{\mu_0} = Q_{av}, \quad \text{(C.59)}$$

$$S_0^* = S_0 \frac{{R_0}^2}{{R_E}^2} \frac{1}{\overline{\mu_0}\pi} \left(h_0 \sin(\phi)\sin(\delta) + \cos(\phi)\cos(\delta)\sin(h_0)\right). \quad \text{(C.60)}$$

C.4 Cloud-Radiative Effects

One useful way to quantify the amount of water in the atmosphere is the total water path (TWP). To calculate this the amount of water is integrated from the surface to the top of the atmosphere (TOA). The amount of water can be calculated using the density and the total water mixing ratio. The equation for the TWP is displayed in equation C.61,

$$TWP = \int_0^{TOA} \rho_{air} q_t dz. \tag{C.61}$$

Although the TWP is a useful quantity to define the amount of water in the atmosphere, it is often useful to determine the amount of clouds in the atmosphere. To calculate this the cloud water path (CWP) can be calculated. The equation for the CWP is displayed in equation C.62,

$$CWP = \int_0^{TOA} \rho_{air} q_l dz. \tag{C.62}$$

These clouds affect the amount of shortwave and longwave radiation. To quantify the effect from the clouds on the radiation the cloud radiative effect is calculated following Ramanathan et al. (1989). The longwave cloud radiative effect is the difference in longwave radiation emitted into space as can be calculated using the following equation. This effect is usually positive, as a cloudy sky blocks a percentage of the upward longwave radiation,

$$LWCRE = \left(LW^{\uparrow}_{TOA}\right)_{clear} - \left(LW^{\uparrow}_{TOA}\right)_{cloudy}. \tag{C.63}$$

The shortwave cloud radiative effect is the difference in absorbed shortwave radiation. For the calculation the amount of reflected shortwave radiation needs to be deducted from the incoming shortwave radiation (equation C.64). As the amount of incoming radiation is the same for cloudy and clear skies it can be further simplified (equation C.65). This effect is usually negative, as a clouds generally reflect more shortwave radiation than the surface. Exceptions can occur if the surface is snowy (Ramanathan et al., 1989),

$$SWCRE = \left(SW^{\downarrow}_{TOA} - SW^{\uparrow}_{TOA}\right)_{cloudy} - \left(SW^{\downarrow}_{TOA} - SW^{\uparrow}_{TOA}\right)_{clear}, \tag{C.64}$$

$$SWCRE = \left(SW^{\uparrow}_{TOA}\right)_{clear} - \left(SW^{\uparrow}_{TOA}\right)_{cloudy}. \tag{C.65}$$

Chapter D

Input

D.1 Vertical Grid Spacing

The grid used in all simulations is a non-equidistant grid of 158 points. At the bottom the vertical spacing is at 40 meters similar to the well-known BOMEX case[1]. This spacing should suffice to create turbulence near the surface. A vertical grid spacing of 40 meters on a domain of 30 kilometers would require 750 grid levels, which is computationally very expensive. The grid is hence stretched by 2.5% until the grid has a vertical spacing of 200 meters. A vertical spacing of 200 meters should suffice to simulate appropriate cloud dynamics. Therefore the vertical spacing remains 200 meters until a height of 12 kilometers is reached, after which no clouds are formed. The grid stretches by 1% until a height of approximately 30 kilometers.

During the testing phase of this thesis higher stretch factors have been used, but use of these factors resulted in non-zero fluxes at the top of the domain.

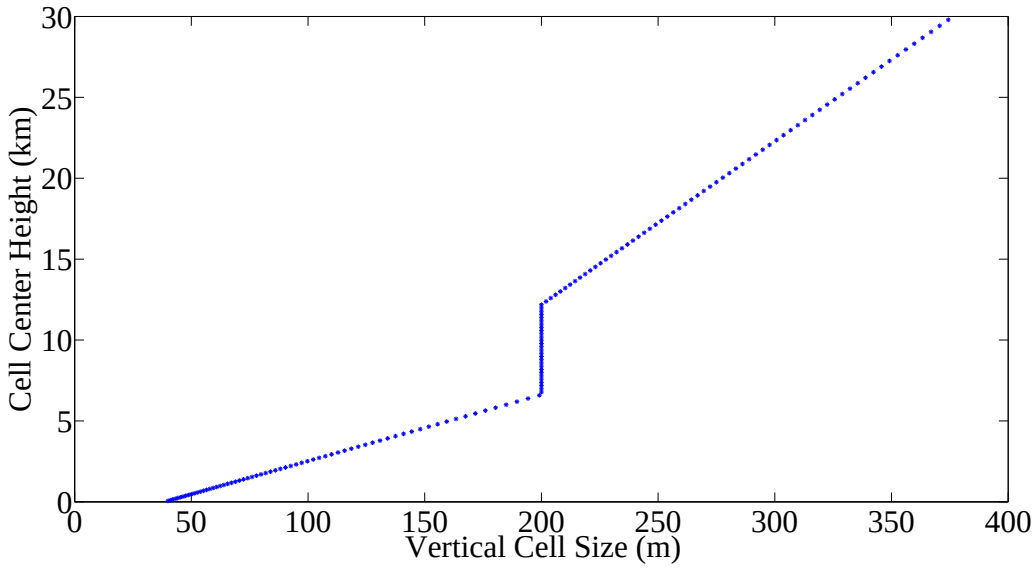

Figure D.1: The vertical grid spacing of the non-equidistant grid used in all simulations is plotted as a function of height. In the lower atmosphere a stretch factor of 2.5% is used, in the upper atmosphere a stretch factor of 1% is used.

[1]For a complete description of the BOMEX case, see: http://www.knmi.nl/ siebesma/gcss/bomex.html

D.2 Ozone Input

Ozone is important in determining the temperature profiles in the stratosphere and absorbs shortwave radiation. It is therefore important to specify the ozone content. As explained in appendix chapter B.3 it was not possible to user-specify the ozone content inside the LES domain in the original DALES version.

This can be resolved by introducing several lines of code to interpolate the ozone content as a function of pressure in the LES domain, however this modification was written after the main part of the experiments have been carried out. Therefore the all experiments use the standard ozone profile of RRTMG, as depicted in figure D.2. This is an ozone profile for a mid-latitude location in summer (Mlawer et al., 1997).

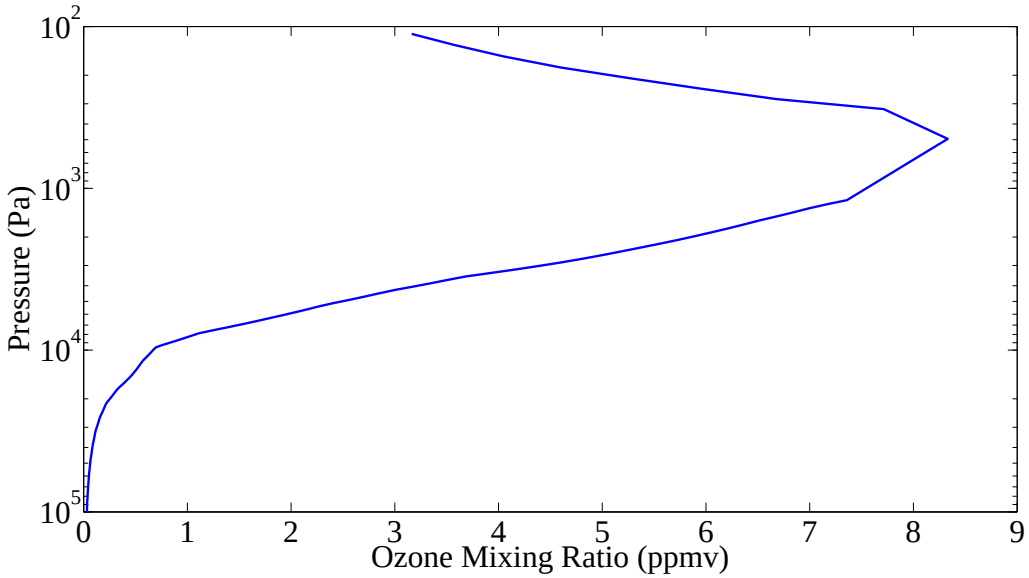

Figure D.2: The built-in ozone content from the RRTMG code as used for the simulations. The ozone mixing ratio in RRTMG is specified as a function of the pressure. The top of the LES domain is located at approximately $10^3 Pa$.

D.3 Namoptions

The following namoptions file has been used to provide input and settings of the simulations. The surface potential temperature (*thls* or θ_{ls}) have been varied across simulations. Moreover several different settings for advection and microphysics scheme have been used.

```
&RUN
iexpnr     =  050
lwarmstart = .false.
startfile  = 'initd576h00m000.048'
runtime    = 4320000.
trestart   =  86400.
ladaptive  = .true.
iTimeInt   =  1
irandom    =  43
krand      =  20
randthl    =  0.1
randqt     =  1e-10
nsv        =  2
courant    =  1.4
peclet     =  0.14
/

&DOMAIN
imax       =  64
jtot       =  64
kmax       =  158

xsize      =  16000.
ysize      =  16000.

xlat       =  17
xlon       =  149
xday       =  196
xtime      =  0
/

&PHYSICS
igrw_damp  =  2
isurf      =  2

timerad    =  600
iradiation =  4
lCnstZenith = .true.
lCnstAlbedo = .true.
useMcICA   = .false.
cnstZenith =  38.6890
sw0        =  571.8055
ps         =  101500
thls       =  299.1

rad_ls     = .false.
rad_longw  = .true.
rad_shortw = .true.
rad_smoke  = .false.
usero3     = .false.
lcoriol    = .true.
ltimedep   = .false.

/
&NAMSURFACE
z0         =  2e-4
z0mav      =  2e-4
z0hav      =  2e-4
albedoav   =  0.05
/
&DYNAMICS
cu         =  0.01
cv         =  5
ibas_prf   =  3
iadv_mom   =  5
iadv_tke   =  55
iadv_thl   =  55
iadv_qt    =  55
iadv_sv    =  55 55
lambda_crit = 20.
/
&NAMMICROPHYSICS
imicro     = 5
ibulk      = 3
l_sedc     = .true.
l_rain     = .true.
l_mur_cst  = .false.
l_warm     = .false.
mur_cst    = 0
Nc_0       = 100e6
sig_g      = 1.2
/
&NAMNUDGE
lnudge   = .false.
/
&NAMCHECKSIM
tcheck     =  3600.
/
&NAMBULKMICROSTAT
lmicrostat = .false.
timeav     = 3600.
dtav       = 600.
/
&NAMSAMPLING
lsamptend  = .true.
lsampcl    = .true.
lsampcldup = .true.
lsampco    = .true.
lsampup    = .true.
lsampbuup  = .true.
dtav       = 600.
timeav     = 3600.
/
&NAMTIMESTAT
ltimestat  = .true.
dtav       = 600.
iblh_meth  = 2
iblh_var   = -2
blh_nsamp  = 1
/
&NAMCROSSSECTION
lcross     = .false.
dtav       = 600.
/
&NAMGENSTAT
lstat      = .true.
dtav       = 600.
timeav     = 3600.
/
&NAMSTATTEND
dtav       = 600.
ltend      = .false.
/
&NAMRADSTAT
```

```
125 lstat = .true.
126 lradclearair = .true.
127 dtav = 600.
128 timeav = 3600.
129 /
130 &NAMBUDGET
131 lbudget = .true.
132 dtav    = 600.
133 timeav  = 3600.
134 /
135 &NAMNETCDFSTATS
136 lnetcdf     = .true.
137 /
```

Chapter E

List of Experiments

For an overview of the experiments of this thesis the following lists has been added to this appendix. The experiments have been split into radiative equilibrium experiments (chapter 5), radiative-convective equilibrium experiments (chapter 6) and other experiments to test modifications.

Radiative Equilibrium Experiments

- Experiments chapter 5.1:
  - RadEQ: V1-V16 (job.001-job.016): SST increases in increments of 5K from 275K to 350K
  - RadEq: RE (job.777): Radiative Equilibrium simulation
- Experiments chapter 5.2:
  - EffectGases: CO2 (job.001): Atmosphere with CO_2 only
  - EffectGases: H2OCO2 (job.002): Atmosphere with H_2O and CO_2 only
  - EffectGases: O3H2OCO2 (job.003): Atmosphere with O_3, H_2O and CO_2
- Experiments chapter 5.3:
  - CO2: V1-V12 (job.001-job.012): Atmosphere with percentage of CO_2, from 0% to 220% in steps of 20%
  - H2O: V1-V12 (job.001-job.012): Atmosphere with percentage of H_2O, from 0% to 220% in steps of 20%
  - O3: V1-V12 (job.001-job.012): Atmosphere with percentage of O_3, from 0% to 220% in steps of 20%

Radiative-Convective Equilibrium Experiments

- Initial Simulations:
  - Initial Simulations: 050 (job.050): RCE simulation with a SST of 28°C
  - Initial Simulations: 052 (job.052): RCE simulation with a SST of 26°C
  - Initial Simulations: 054 (job.054): RCE Warmstart of 052
  - Initial Simulations: 056 (job.056): Lower resolution grid version of 052, TOA fluxes don't go to zero

- Small Domain:
  - Small Domain: 104 (job.104): RCE simulation with a SST of 22°C
  - Small Domain: 105 (job.105): RCE simulation with a SST of 28°C
  - Small Domain: 106 (job.106): RCE simulation with a SST of 24°C
  - Small Domain: 107 (job.107): RCE simulation with a SST of 26°C
  - Small Domain: 204 (job.204): Warmstart of 104 with 24 extra hours of computation
  - Small Domain: 205 (job.205): Warmstart of 105 with 24 extra hours of computation
  - Small Domain: 206 (job.206): Warmstart of 106 with 24 extra hours of computation
  - Small Domain: 207 (job.207): Warmstart of 107 with 24 extra hours of computation
  - Small Domain: 304 (job.304): Warmstart of 204 with 16 extra hours of computation
- Large Domain:
  - Large Domain: 010 (job.010): RCE simulation with a SST of 26°C
  - Large Domain: 011 (job.011): RCE simulation with a SST of 28°C
  - Large Domain: 012 (job.012): RCE simulation with a SST of 24°C
  - Large Domain: 013 (job.013): RCE simulation with a SST of 22°C

Other Simulations:

- IceTest
  - Ice: V1-V30 (job.001-job.030): Radiation-only simulation with a fixed cloud, 100% ice cloud. Water varied in steps of $0.005g/kg$ from $q_{sat} + 0$ to $q_{sat} + 0.145$
  - Water: V1-V30 (job.001-job.030): Radiation-only simulation with a fixed cloud, 100% water cloud. Water varied in steps of $0.005g/kg$ from $q_{sat} + 0$ to $q_{sat} + 0.145$
  - 5050: V1-V30 (job.001-job.030): Radiation-only simulation with a fixed cloud, 50-50% ice-water cloud. Water varied in steps of $0.005g/kg$ from $q_{sat} + 0$ to $q_{sat} + 0.145$
- RCEcompare
  - FixT (job.001): For comparison with RCE at 26°C. Same settings, radiation only, fixed surface temperature of 26°C. Used for figure 6.1
  - RadT (job.002): For comparison with RCE at 26°C. Same settings, radiation only, radiative equilibrium surface temperature. Used for figure 6.1

Chapter F

Turbulent Spectra Small domain

The final radiative-convective equilibrium simulations were simulated on a $72km \times 72km$ domain. Initially however simulations on a 9 times smaller $24km \times 24km$ domain were performed as to extract input profiles for the large domain radiative-convective simulations. On the $24km \times 24km$ domain the highest possible wavenumber is $4.167 \times 10^{-5} m^{-1}$ corresponding to the 24 km size of the domain. Some mesoscale fluctuations can hence occur. On the $72km \times 72km$ domain however, more mesoscale fluctuations were observed as can be seen in figure 6.11. In figure F.1 the spectra of the $24km \times 24km$ domain can be observed. Note that many of these spectra have a minimum located at the wavenumbers between $10^{-5} m^{-1}$ and $10^{-4} m^{-1}$, whereas some of the simulations on the $72km \times 72km$ domain have a maximum located at these wavelengths.

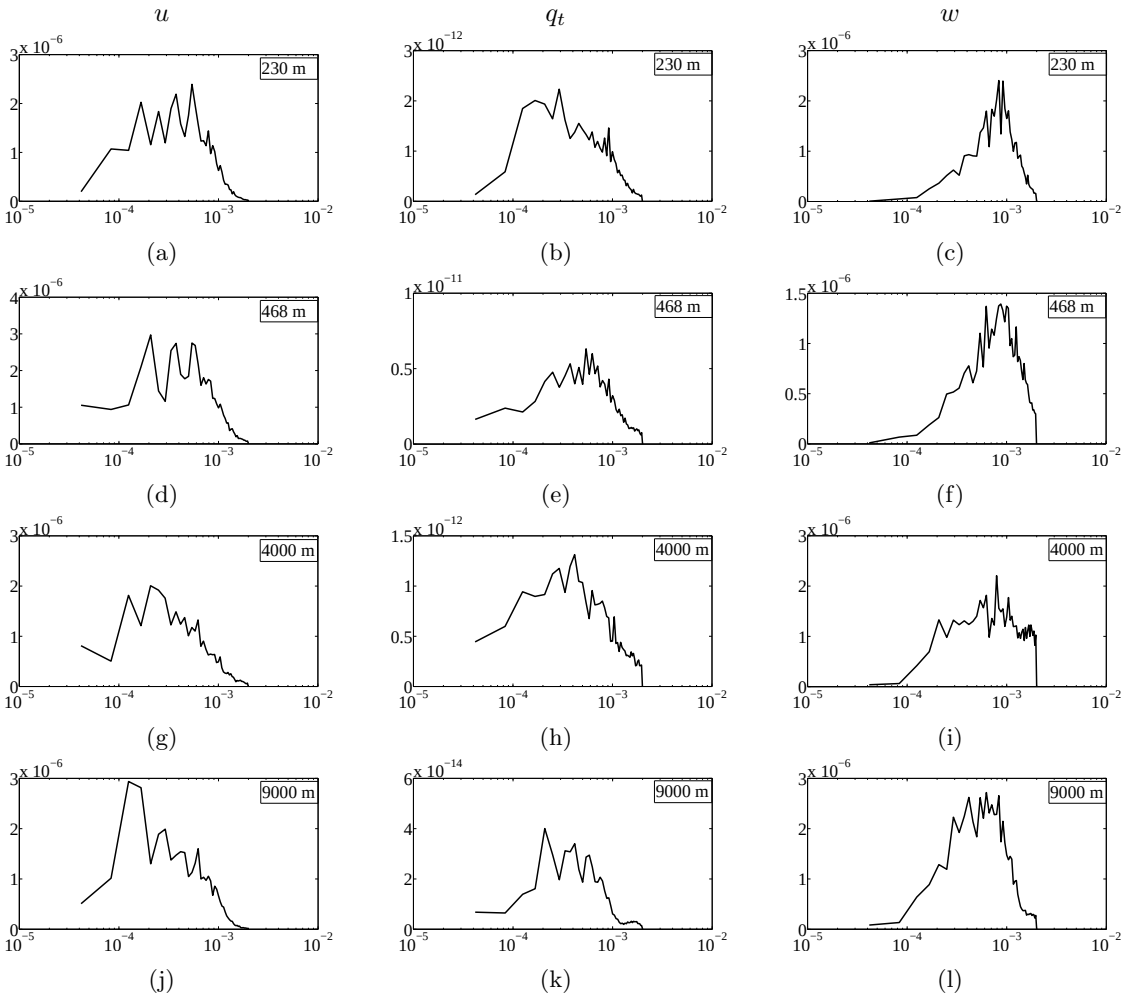

Figure F.1: Variance spectrum plots on the $24km \times 24km$ domain after 196 hours of simulated time. The surface temperature is 26 °C. The variance spectra multiplied by the wavenumber (kS) have been plotted on the y-axis as a function of the wavenumber (k) on the logarithmic x-axis. The wavenumber on the x-axis is expessed in m^{-1}. The units on the y-axes are m^2/s^2 in the left and right column and kg^2/kg^2 in the middle column. The first row is data from the boundary layer at 230m, the second row is positioned at the cloud base at 468m. The third row is located at 4 kilometers and the fourth row is located at 9 kilometers in the cloudy layer at the top of the troposphere.

Bibliography

AMETSOC. Glossary of Metereology: Moist-Adiabatic Lapse Rate, 2015. URL `http://web.archive.org/web/20150705025414/http://www.ospo.noaa.gov/data/sst/contour/global_small.fc.gif`. [Online; accessed 23-September-2015].

P.N. Blossey and D.R. Durran. Selective monotonicity preservation in scalar advection. *Journal of Computational Physics*, 227(10):5160 – 5183, 2008.

P.N. Blossey, C.S. Bretherton, M. Zhang, A. Cheng, S. Endo, T. Heus, Y. Liu, A.P. Lock, S.R. Roode, and K.M. Xu. Marine low cloud sensitivity to an idealized climate change: The CGILS LES intercomparison. *Journal of Advances in Modeling Earth Systems*, 5(2):234–258, 2013.

S.J. Böing. *The interaction between deep convective clouds and their environment*. PhD thesis, Delft University of Technology, 2014.

S.J. Böing, H.J.J. Jonker, A.P. Siebesma, and W.W. Grabowski. Influence of the subcloud layer on the development of a deep convective ensemble. *Journal of the Atmospheric Sciences*, 69(9):2682–2698, 2012.

C.S. Bretherton, P.N. Blossey, and M. Khairoutdinov. An energy-balance analysis of deep convective self-aggregation above uniform SST. *Journal of the atmospheric sciences*, 62(12):4273–4292, 2005.

G.H. Bryan and J.M. Fritsch. A reevaluation of ice-liquid water potential temperature. *Monthly weather review*, 132(10):2421–2431, 2004.

T.W. Cronin. On the choice of average solar zenith angle. *Journal of the Atmospheric Sciences*, 71(8): 2994–3003, 2014.

S.R. de Roode, P.G. Duynkerke, and H.J.J. Jonker. Large-eddy simulation: How large is large enough? *Journal of the atmospheric sciences*, 61(4):403–421, 2004.

J.W. Deardorff. A numerical study of three-dimensional turbulent channel flow at large Reynolds numbers. *Journal of Fluid Mechanics*, 41(2):453–480, 1970.

J.W. Deardorff. Theoretical expression for the countergradient vertical heat flux. *Journal of Geophysical Research*, 77(30):5900–5904, 1972.

E.E. Ebert and J.A. Curry. A parameterization of ice cloud optical properties for climate models. *Journal of Geophysical Research: Atmospheres*, 97(D4):3831–3836, 1992.

ECMWF. *IFS Documentation Cy40r1, Operational Implementation 22 November 2013, Part II Data Assimilation*, November 2013.

Q. Fu and K.N. Liou. On the correlated k-distribution method for radiative transfer in nonhomogeneous atmospheres. *Journal of the Atmospheric Sciences*, 49(22):2139–2156, 1992.

I.M. Held, R.S. Hemler, and V. Ramaswamy. Radiative-convective equilibrium with explicit two-dimensional moist convection. *Journal of the atmospheric sciences*, 50(23):3909–3927, 1993.

T. Heus and H.J.J. Jonker. Subsiding shells around shallow cumulus clouds. *Journal of the Atmospheric Sciences*, 65(3):1003–1018, 2008.

T. Heus, C.C. van Heerwaarden, H.J.J. Jonker, A.P. Siebesma, S. Axelsen, K. van den Dries, O. Geoffroy, A.F. Moene, D. Pino, S.R. de Roode, and J. Vilà-Guerau de Arellano. Formulation of the Dutch Atmospheric Large-Eddy Simulation (DALES) and overview of its applications. *Geoscientific Model Development*, 3(2):415–444, 2010a.

T. Heus, C.C. van Heerwaarden, J. van der Dussen, and H. Ouwersloot. *Overview of all namoptions in DALES*, December 2010b.

A.J. Heymsfield and C.M.R. Platt. A parameterization of the particle size spectrum of ice clouds in terms of the ambient temperature and the ice water content. *Journal of the atmospheric sciences*, 41 (5):846–855, 1984.

D.J. Hill and D.I. Pullin. Hybrid tuned center-difference-WENO method for large eddy simulations in the presence of strong shocks. *Journal of Computational Physics*, 194(2):435–450, 2004.

S. Islam, R.L. Bras, and K.A. Emanuel. Predictability of mesoscale rainfall in the tropics. *Journal of Applied Meteorology*, 32(2):297–310, 1993.

ISO. *International Standard ISO 2533*. International Organization for Standardization, 1978.

D.K. Lilly. The representation of small scale turbulence in numerical simulation experiments. *IBM Scientific Computing Symposium on environmental sciences*, pages 195–210, 1967.

S. Manabe and R.F. Strickler. Thermal equilibrium of the atmosphere with a convective adjustment. *Journal of the Atmospheric Sciences*, 21(4):361–385, 1964.

S. Manabe and R.T. Wetherald. Thermal equilibrium of the atmosphere with a given distribution of relative humidity. *Journal of the Atmospheric Sciences*, 24(3):241–259, 1967.

E.J. Mlawer, S.J. Taubman, P.D. Brown, M.J. Iacono, and S.A. Clough. Radiative transfer for inhomogeneous atmospheres: RRTM, a validated correlated-k model for the longwave. *Journal of Geophysical Research: Atmospheres*, 102(D14):16663–16682, 1997.

M.F. Modest. The Treatment of Nongray Properties in Radiative Heat Transfer: From Past to Present. *Journal of Heat Transfer*, 135(6), 2013a.

M.F. Modest. *Radiative Heat Transfer*. Academic Press, 2013b.

NASA. *Landsat 7 Science Data Users Handbook*, March 2011.

NOAA. NOAA/NESDIS geo-polar blended 5km SST analysis for the full globe - 03 July 2015, 2015. URL `http://web.archive.org/web/20150705025414/http://www.ospo.noaa.gov/data/sst/contour/global_small.fc.gif`. [Online; accessed 11-August-2015].

NOAA, NASA, and USAF. *U.S. Standard Atmosphere*. National Oceanic and Atmospheric Administration, 1976.

S.C. Ou and K.N. Liou. Ice microphysics and climatic temperature feedback. *Atmospheric Research*, 35 (24):127 – 138, 1995.

R.K. Pachauri, M.R. Allen, V.R. Barros, J. Broome, W. Cramer, R. Christ, J.A. Church, L. Clarke, Q. Dahe, P. Dasgupta, et al. *Climate Change 2014: Synthesis Report. Contribution of Working Groups I, II and III to the Fifth Assessment Report of the Intergovernmental Panel on Climate Change*. IPCC, 2014.

O. Pauluis and I.M. Held. Entropy budget of an atmosphere in radiative-convective equilibrium. Part I: Maximum work and frictional dissipation. *Journal of the Atmospheric sciences*, 59(2):125–139, 2002.

P. Räisänen. Two-stream approximations revisited: A new improvement and tests with GCM data. *Quarterly Journal of the Royal Meteorological Society*, 128(585):2397–2416, 2002.

V. Ramanathan. The role of earth radiation budget studies in climate and general circulation research. *Journal of Geophysical Research*, 92(D4):4075–4095, 1987.

V. Ramanathan, R.D. Cess, E.F. Harrison, P. Minnis, B.R. Barkstrom, E. Ahmad, and D. Hartmann. Cloud-radiative forcing and climate: Results from the Earth Radiation Budget Experiment. *Science*, 243(4887):57–63, 1989.

F.R. Robe and K.A. Emanuel. Moist convective scaling: Some inferences from three-dimensional cloud ensemble simulations. *Journal of the atmospheric sciences*, 53(22):3265–3275, 1996.

S.M.A. Rodts, P.G. Duynkerke, and H.J.J. Jonker. Size distributions and dynamical properties of shallow cumulus clouds from aircraft observations and satellite data. *Journal of the atmospheric sciences*, 60 (16):1895–1912, 2003.

R.R. Rogers and M.K. Yau. *A short course in cloud physics, International series in natural philosophy.* Butterworth Heinemann, 3 edition, 1989.

D.M. Romps. Response of tropical precipitation to global warming. *Journal of the Atmospheric Sciences*, 68(1):123–138, 2011.

M.L. Salby. *Fundamentals of Atmospheric Physics.* Academic Press, 1996.

J. Smagorinsky. General circulation experiments with the primitive equations: I. the basic experiment*. *Monthly weather review*, 91(3):99–164, 1963.

C.H. Sui, K.M. Lau, W.K. Tao, and J. Simpson. The tropical water and energy cycles in a cumulus ensemble model. part i: Equilibrium climate. *Journal of the atmospheric sciences*, 51(5):711–728, 1994.

F.W. Taylor. *Elementary Climate Physics.* Oxford University Press, 2005.

A.M. Tompkins and G.C. Craig. Radiativeconvective equilibrium in a three-dimensional cloud-ensemble model. *Quarterly Journal of the Royal Meteorological Society*, 124(550):2073–2097, 1998.

J.J. van der Dussen. *Stratocumulus transitions in present-day and future climate.* PhD thesis, Delft University of Technology, 2015.

J.J. van der Dussen, S.R. Roode, A.S. Ackerman, P.N. Blossey, C.S. Bretherton, M.J. Kurowski, A.P. Lock, R.A.J. Neggers, I. Sandu, and A.P. Siebesma. The GASS/EUCLIPSE model intercomparison of the stratocumulus transition as observed during ASTEX: LES results. *Journal of Advances in Modeling Earth Systems*, 5(3):483–499, 2013.

G.J. van Zadelhoff, E. Van Meijgaard, D.P. Donovan, W.H. Knap, and R. Boers. Sensitivity of the shortwave radiative budget to the parameterization of ice crystal effective radius. *Journal of Geophysical Research: Atmospheres*, 112(D8), 2007.

A.A. Wing and K.A. Emanuel. Physical mechanisms controlling self-aggregation of convection in idealized numerical modeling simulations. *Journal of Advances in Modeling Earth Systems*, 6(1):59–74, 2014.

H.M. Worden, K.W. Bowman, J.R. Worden, A. Eldering, and R. Beer. Satellite measurements of the clear-sky greenhouse effect from tropospheric ozone. *Nature Geoscience*, 1(5):305–308, 2008.

W.G. Zdunkowski, R.M. Welch, and G. Korb. An investigation of the structure of typical two-stream-methods for the calculation of solar fluxes and heating rates in clouds. *Beiträge zur Physik der Atmosphäre*, 53(2):147–166, 1980.